Wake Re-Energization of a Scaled Wind Farm via the Use of Lifting Devices: An Experimental Study

M.J. Fijen

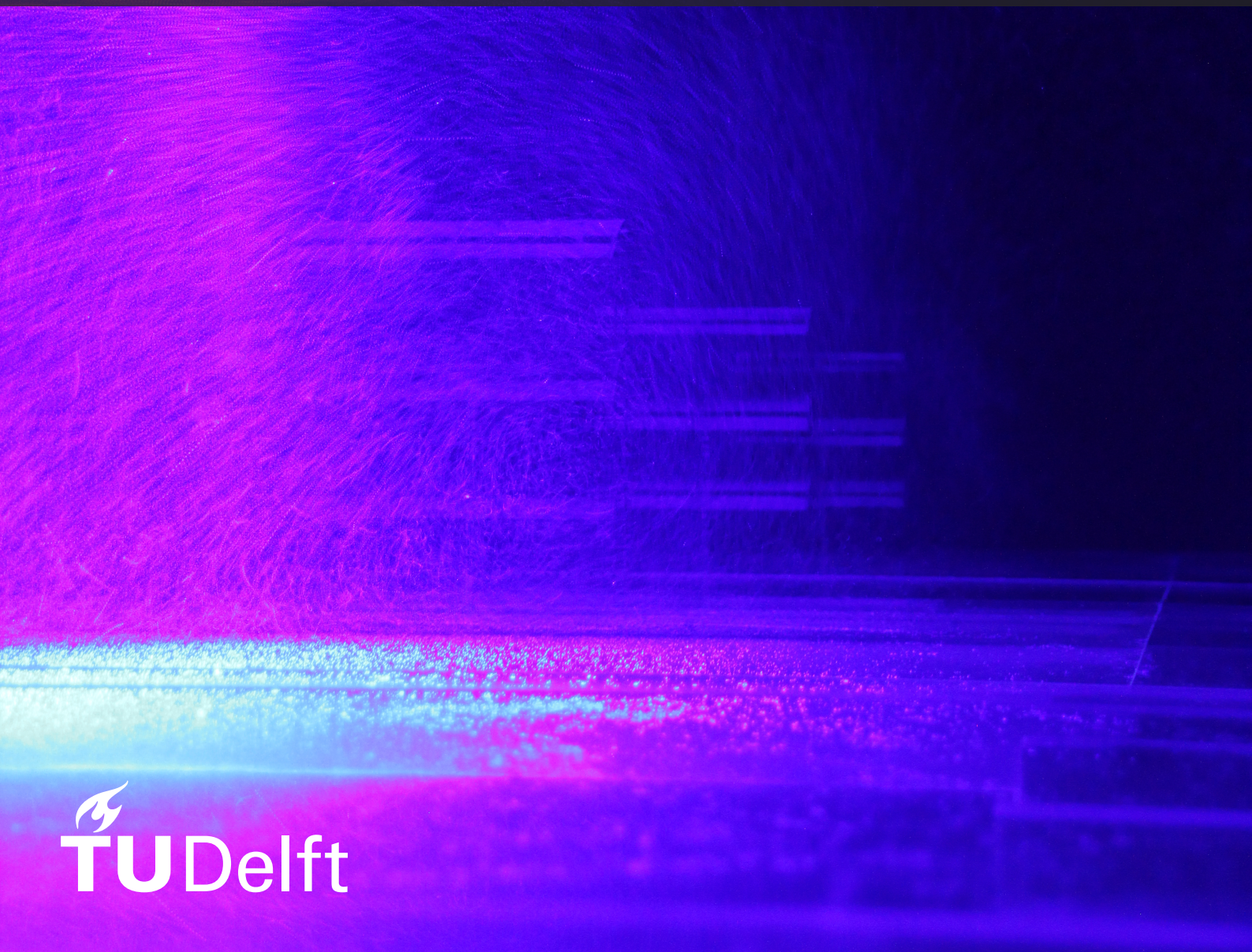

TU Delft

Wake Re-Energization of a Scaled Wind Farm via the Use of Lifting Devices: An Experimental Study

by

M.J. Fijen

to obtain the degree of Master of Science
at the Delft University of Technology,
to be defended publicly on Monday March 7, 2025 at 09:30 AM.

Student number:	5643724	
Project duration:	March, 2024 – March, 2025	
Thesis committee:	A. Sciacchitano,	TU Delft, Supervisor
	Y. Li,	TU Delft, Supervisor
	W. Yu,	TU Delft, Chair
	A.H. van Zuijlen	TU Delft, Examiner
Additional supervisor:	C.J. Simão Ferreira	TU Delft

An electronic version of this thesis is available at `http://repository.tudelft.nl/`.

TU Delft

Preface

This thesis represents the culmination of a year of learning, research, and collaboration. I am grateful to everyone who supported me throughout this journey.

First and foremost, I would like to express my heartfelt gratitude to Clem for his invaluable guidance and mentorship over the past year. Your insights and encouragement have been of great importance in the completion of this work. You were always there to help when I needed it, and I truly appreciate your support. Although we were both relatively inexperienced with conducting experiments, I am glad we took on the challenge together. Brian, your assistance during both experimental campaigns was exceptional. Your kindness and willingness to explain things made the long days in the wind tunnels enjoyable and productive.

I am also thankful to Carlos, whose passion for wind farm design inspired me to pursue this fascinating area of study. Your guidance and mindset were invaluable during the preparation for the wind farm experiments. My sincere thanks go to Andrea for sharing his boundless expertise in aerodynamics and wind tunnel testing. Your problem-solving mentality and practical advice were crucial to the success of this project. Finally, I would like to extend my gratitude to Ed for his dedication to producing all the essential parts for my wind tunnel experiments. Your efforts ensured the smooth progress of my research.

To all who contributed to this work, thank you for your support, inspiration, and belief in my efforts. It was a pleasure working with you all, and I truly enjoyed this journey.

M.J. Fijen
Delft, February 2025

Abstract

The development of offshore wind farms has demonstrated significant value in harnessing renewable energy sources. However, the offshore wind energy sector faces increasing challenges, making the realization of new wind farms a greater financial risk. This has reached the point where several high-profile offshore wind projects have been halted. A key contributor to these struggles is the aerodynamic effect of wind farm wake losses. As wind turbine sizes increase, costs rise, but the wind farm concept limits energy yield. This is due to slow wake recovery behind turbines, causing downstream turbines to only be able to harvest energy from low-momentum flow. Based on the literature review conducted, the methods to improve wind farm efficiency by reducing wake losses, such as wind farm layout optimization and rotor yawing or tilting, only partially address the problem.

The concept of regenerative wind farming, proposed by Ferreira, seeks to provide a solution. This involves integrating lifting devices into wind energy harvesting systems that can redirect the wake vertically, enabling the flow from higher atmospheric layers to contribute more to the wake recovery process. Such interactions can dramatically enhance the energy that is replenished into the wind farm, offering a promising approach to overcoming these challenges.

This research aims to evaluate the potential of the novel wind farm concept, regenerative wind farm, through a scaled wind farm experiment. In the scaled wind farm, there are nine wind energy harvesting systems, which are aerodynamically modeled by using porous disks and wings. The study focuses on the far wake and the performance of downstream turbines. The experiment was conducted in the Open Jet Facility (OJF) at TU Delft. The flow field was measured using Particle Tracking Velocimetry (PTV) with Helium-Filled Soap Bubbles (HFSB), and load measurements were accompanied.

Load measurements revealed that thrust values for downstream turbines increased by more than three times when lifting devices were attached to the actuator surfaces. Also, flow field data showed significantly higher wake velocities, as potent vertical flows in the wake regions were induced by the tip-vortices of the wings, which enhanced vertical energy entrainment. This vertical motion actively entrains the flow above the wind farm, allowing high-momentum air to enter the wind farm layer, something that does not occur without the wings. Additionally, the lifting devices reduce turbulence intensity in the rotor projection area at the downstream end of the wind farm, helping to lower the fatigue loading of downstream systems. An investigation of a misaligned row confirmed that the concept remains effective even under such conditions.

This work demonstrates that the regenerative wind farm concept holds great potential to enhance wind farm power output while reducing the required wind farm area. With this concept, wind turbine wake losses are effectively mitigated by entraining high-momentum flow into the wind farm.

Contents

List of Figures

Nomenclature

Abbreviations

Abbreviation	Definition
ABL	Atmospheric Boundary Layer
AEP	Annual Energy Production
CFD	Computational Fluid Dynamics
EROI	Energy Return On Investment
HAWT	Horizontal Axis Wind Turbine
IBL	Internal Boundary Layer
LED	Light Emitting Diode
LES	Large Eddy Simulations
MRS	Multi Rotor System
MRSL	Multi Rotor System with Lifting devices
OJF	Open Jet Facility
PIV	Particle Image Velocimetry
PTV	Particle Tracking Velocimetry
RANS	Reynolds-averaged Navier Stokes
RGWF	Re-Generative Wind Farm
SOWFA	Simulator fOr Wind Farm Applications
STB	Shake-The-Box
TSR	Tip Speed Ratio
TI	Turbulence Intensity
VAWT	Vertical Axis Wind Turbine
WTABL	Wind Turbine Array Boundary Layer

Symbols

Symbol	Definition	Unit
A	Area	$[\mathrm{m}^2]$
C_L	Lift coefficient	[-]
d	Rotor diameter	[m]
D	Rotor diameter	[m]
$\widehat{D}^W$	Normalized time-averaged rotors' drag	[-]
f_i	External force in the i-direction	[N]
L	Characteristic length	[m]
L_f	Lift force	[N]
$\widehat{L}^W$	Normalized time-averaged wings' lift	[-]
M	Mean wind speed	$[\mathrm{m/s}]$
n	Rotational speed	$[\mathrm{s}^{-1}]$
$\overline{p}$	Mean pressure	[Pa]
P_{Row}	Harvested power from each row in a wind farm	[W]
$P_{Row,1}$	Harvested power from the first row in a wind farm	[W]
P_w	Power from wind	[W]
R	Blade radius	[m]
Re	Reynolds number	[-]
$\widehat{T}^R$	Normalized time-averaged MRSL thrust	[-]
u	Wind speed	[m/s]
$\mathbf{u}$	Velocity vector	[m/s]
$\overline{u}$	Average velocity in x-direction	[m/s]
$\overline{u_i}$	Mean velocity in the i-direction	[m/s]
u_i'	Fluctuating velocity component in the i-direction	[m/s]
u'	Fluctuating velocity component in the i-direction	[m/s]
u_∞	Freestream velocity	[m/s]
$\overline{v}$	Average velocity in y-direction	[m/s]
v'	Fluctuating velocity component in the y-direction	[m/s]
$\overline{w}$	Average velocity in z-direction	[m/s]
w'	Fluctuating velocity component in the z-direction	[m/s]
α	Angle of attack	[-]
θ	Mean potential temperature	[K]
θ_P	Wing pitch angle	[-]
θ_{wind}	Wind direction	[-]
μ	Dynamic viscosity	[Pa·s]
ρ	Fluid Density	$[\mathrm{kg/m}^3]$
ω	Vorticity	$[\mathrm{s}^{-1}]$

1

Introduction

The realization of offshore wind farms has proven its added value in exploiting renewable energy sources [1]. The increase in wind turbine size has made energy production vastly efficient while the realization costs could be kept low when positioning the turbines in clusters, which are known as wind farms [2]. Looking into the future of offshore wind energy for the Netherlands, multiple wind farms are awaiting its realization. Moreover, new locations are being investigated for even more farms [3].

However, several high-profile offshore wind projects in the U.S. and Europe have been halted, primarily due to escalating costs. Additionally, turbine manufacturers have incurred losses amounting to billions. These challenges stem from rising costs driven by strained supply chains, increasing interest rates, and additional uncertainties related to inflation [4]. These factors increase the financial risk for the realization of wind farms.

Moreover, wake effects ensure the energy yield of wind farms is dropping rapidly with the size of the wind farm [5]. Therefore, not only should the wind turbines become more efficient but the entire wind farm is expected to increase its performance as they are suffering from severe energy loss due to wake effects. Additionally, as modern wind turbines are scaled up to multi-megawatt capacities, the energy gains from larger rotor sizes are increasingly outweighed by the rise in mass and cost. Consequently, the conventional single-rotor design becomes economically unfeasible at very large scales [6]. The fast increase in wind turbine size in past years ensures economies of scale are being reduced and the supply chain is relying on fewer manufacturers. As a result, the size of offshore wind turbines reached a state where the potential energy gains do not outweigh the added costs. This means that the expected energy yield per area for wind farms is not being achieved by simply increasing the size of turbines.

The current state of the wind energy market calls for innovative engineering solutions to enhance wind farm efficiency. These improvements are essential to restore the competitive edge of wind energy and accelerate the transition to green energy sources. Therefore, this work aims to explore and understand wind turbine wakes, wind farm aerodynamics, methods to enhance wind farm efficiency by reducing wake losses, and experimental elements through a comprehensive review of existing literature. In this review, already established research topics into the efficiency improvement of wind farms are discussed. Additionally, it proposes the novel idea from Ferreira to take this a step further, focusing on increased vertical entrainment enlarging the interaction with the atmospheric boundary layer by using lifting devices [7]. These subjects can be reviewed in chapter 2. Moreover, this work includes two wind tunnel experiments to assess Ferreira's concept. The first experiment focuses on developing a small Multi-Rotor System with Lifting devices (MRSL) created using a porous surface with attached wings. The second, and main, experiment is the Regenerative Wind Farm Experiment, in which a scaled wind farm containing nine MRSLs is tested. This experiment will provide insights into the far wake and overall wind farm behavior

of MRSLs, an area that remains unexplored. The methodology and results of the first experiment, along with the final MRSL design, are presented in chapter 3. The methodology for the Regenerative Wind Farm Experiment is described in chapter 4, while its results and discussion appear in chapter 5.

2

Theoretical Background

This chapter investigates the wake structure of a single turbine and researches the characteristics and aerodynamics of offshore wind farms. It also aims to identify strategies to improve wind farm efficiency by reducing wake losses and determines the experimental approach needed for the wind farm experiments such as the influence of scaling, the application of lifting devices, and the application of an appropriate flow quantification technique. Finally, the theoretical background will be used to construct the research goal and questions for this work.

2.1. Wind Turbine Wakes

This section reviews the aerodynamic effects of a turbine extracting energy from the wind. For these effects to be studied, the wake characteristics are explained in the first section, and the second section investigates the wake recovery. Moreover, it answers the questions: how does wake recover, where does the energy for wake recovery come from, and what affects its recovery rate?

2.1.1. Wake Characteristics

Wind turbines are devices used to extract kinetic energy from wind. This energy is extracted using a rotor that transfers kinetic energy into mechanical energy in a rotating shaft. Since energy is extracted, the freestream velocity of the wind slows down behind the rotor. Besides slowing down, the rotating rotor introduces a strong increase in turbulence level due to instabilities induced by tip and root vortices. The combination of the increased turbulence level and the wind speed deficit behind the rotor is called the wake of a wind turbine. A visualization of this wake for a single Horizontal Axis Wind Turbine (HAWT) can be seen in Figure 2.1.

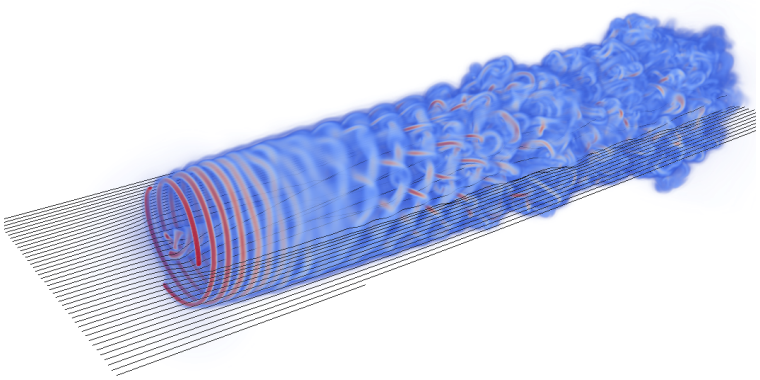

Figure 2.1: Visualization of the wake structure of a single HAWT [8].

The wake behind a turbine can be divided into the near and far wake [9]. Depending on the definition, the region of the near wake is defined where the geometric properties of a rotor can be identified by the wake structures. Examples of these wake structures are the tip and root vortices. Located close to the rotor plane, corresponding to approximately one rotor diameter, the near wake is primarily influenced by a continuous sheet of trailed vorticity shed from the blades. This rolls up into concentrated vortices near the blade roots and tips, generating a helical structure. The far wake is identified as the region after the near wake and is the starting point of wake recovery. The far wake emphasizes the influence of turbines on farms. In the far-wake region, individual vortices are broken down and diffused within the flow due to external atmospheric turbulence. This is where the wake starts to recover.

Figure 2.1 illustrates the instantaneous wake structure of a turbine in a three-dimensional image, while the upper part of Figure 2.2 presents the wake in a two-dimensional figure. The bottom part of this figure also shows the time-averaged velocity profiles $\overline{u}$ in the induction region and the wake. This removes the irregularities caused by turbulence. The average velocity field shows a deficit identified by $\Delta\overline{u}$. This velocity deficit is large in the near wake and reduces in the far wake. The deficit is reduced due to wake recovery, which will be discussed in the next section. It is seen that the average velocity $\overline{u}$ is affected by the energy extraction of the turbine. The region that transits from the lower wind speed to the undisturbed flow is called the shear layer. The induction region is identified ahead of the turbine, where the flow velocity is already affected by the turbine.

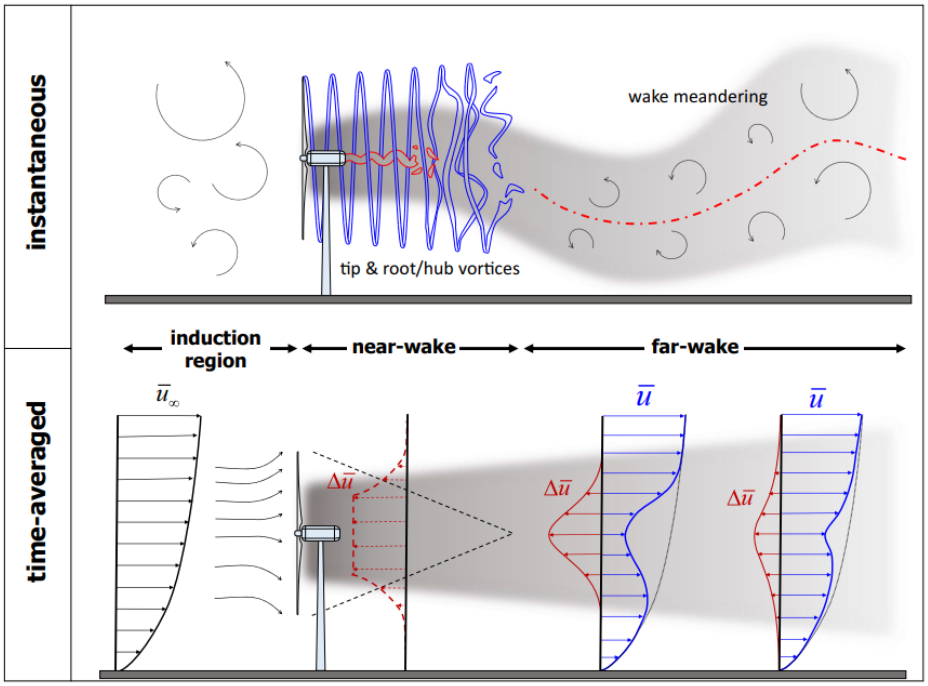

Figure 2.2: Instantaneous and time-averaged velocity field of the wake behind a turbine [10].

Another phenomenon that is indicated in the figure is wake meandering. On many occasions, the wake does not follow a straight line behind the rotor disk but carries lateral motion too. This can occur in the horizontal and vertical planes. Wake meandering originates from crosswinds in the wake and the flow in the wake which can impose lateral forces too. As a consequence, non-uniform inflow conditions for consecutive turbines can occur. This results in uneven blade loading. This wake meandering is however not relevant for wind tunnel experiments conducted as a follow-up of this literature research due to the fact that these phenomena do not occur naturally in a test environment such as wind tunnel experiments and are out of the scope of this research. More information about wake meandering can be found in the work of Larsen [11] and Churchfield [12].

2.1.2. Wake Recovery

In principle, the wake behind a turbine naturally recovers by entraining energy from the surrounding ambient flow. The transport of momentum from the high-speed region to the low-speed region in a shear layer increases with the strength of the wind speed gradient. This momentum transfer is primarily driven by turbulence. Therefore, this turbulent mixing reduces the wind speed deficit behind the turbine by entraining the undisturbed wind. This momentum transport in the shear layer reduces the wind speed gradient eventually covering the entire original stream. The region where the wind speed is regenerated is the far wake and can be identified by increased turbulence from the broken-down vortex structures originally induced by the blade tip and root. Figure 2.3 shows this process, the turbulent mixing reduces the wind speed deficit behind the turbine which is identified as the blue dotted line. At first, the gradient in the shear layer is very large while in the far wake this gradient becomes less and spreads towards the center of the wake.

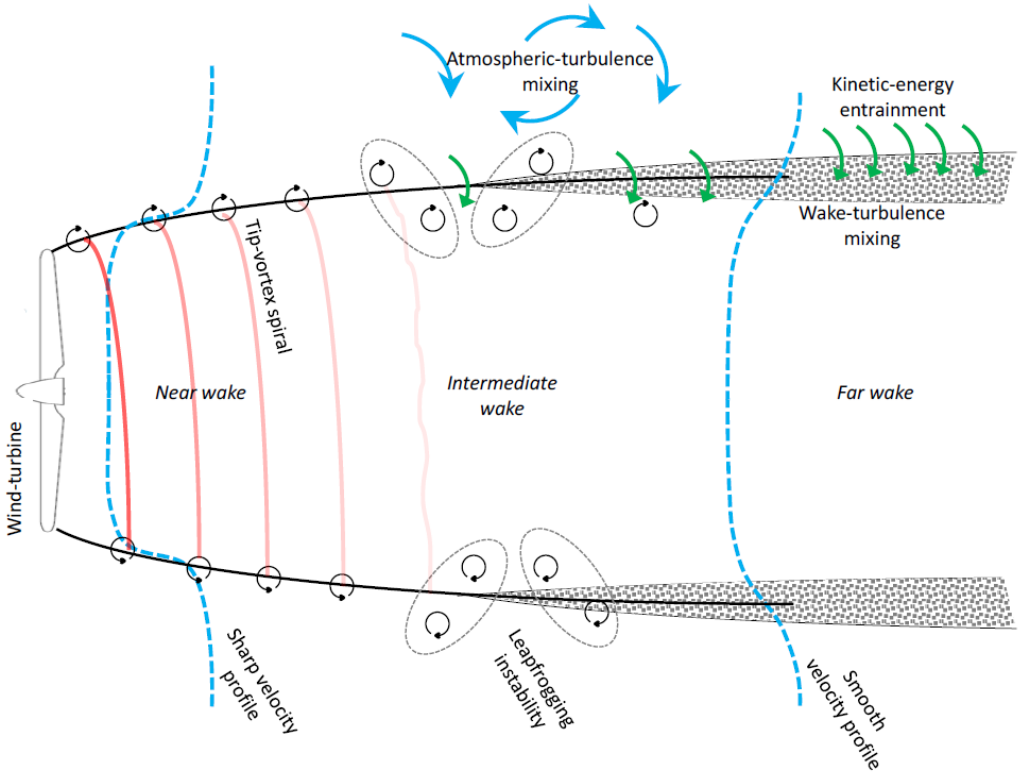

Figure 2.3: Wake recovery process behind a wind turbine, figure retrieved from [13].

The study of Wu and Porté-Agel [14] assesses the wake of a single HAWT by comparing Large-Eddy Simulation (LES) combined with a wind-turbine model to measurements collected with hot-wire anemometry (HWA). The LES results for the case are shown in Figure 2.4.

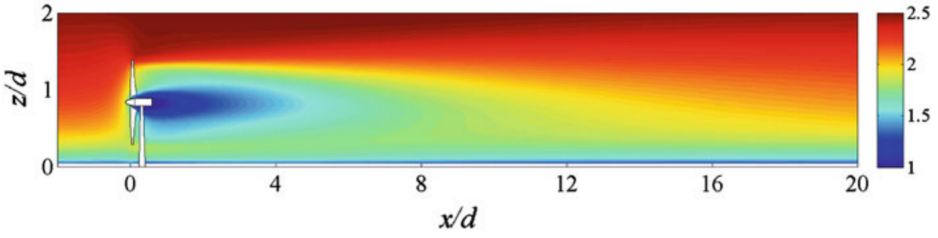

Figure 2.4: Contour of the time-averaged streamwise velocity [14].

As expected from subsection 2.1.1, the velocity deficit is largest near the turbine and decreases as the wake expands and entrains surrounding air. Nevertheless, the wake's influence remains noticeable even in the far wake, at distances as large as $x/d = 20$ which is 20 rotor diameters. Figure 2.5 illustrates this by showing the vertical profile of the time-averaged streamwise velocity. The comparison between measurements and models shows clear agreement in the far wake. Furthermore, even at a distance of 20 rotor diameters downstream, the undisturbed inflow profile has not yet been restored. This highlights the significant impact of wind turbine wakes and underscores the challenge for wind farms, where turbine spacing is much smaller. However, this issue will be addressed in detail in section 2.2.

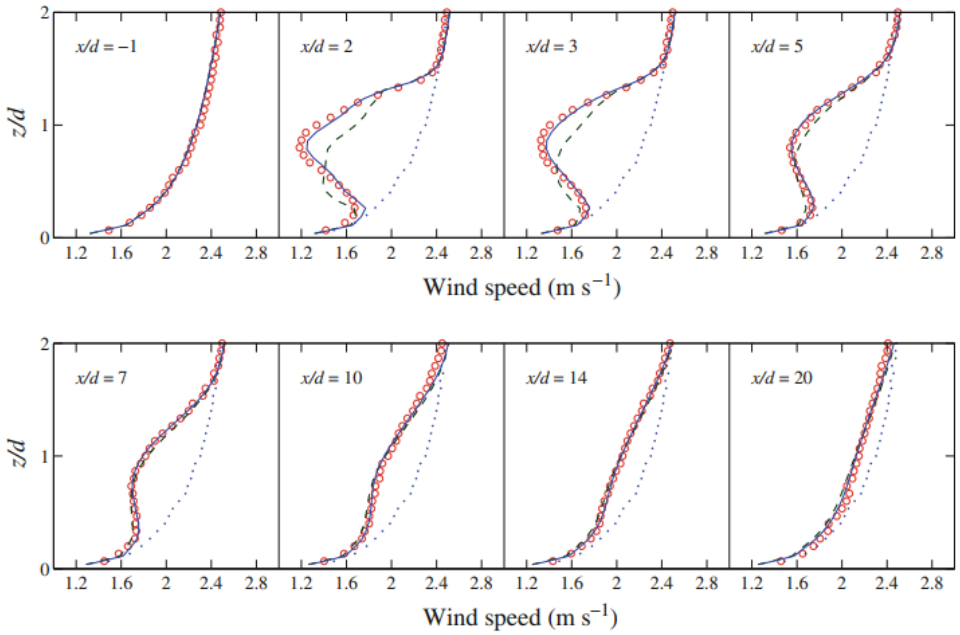

Figure 2.5: Comparison of vertical profiles of the time-averaged streamwise velocity, wind-tunnel measurements shown by the open circles, the two LES models are the solid and dashed line, the dotted line is the undisturbed inflow profile [14].

Figure 2.6 shows the Particle Image Velocimetry (PIV) results of the shedded tip and root vortices in the near wake of a turbine as a function of the downstream location. The root vortices are indicated in red while the tip vortices can be identified by the blue vortex cores. These vortices occur due to the pressure difference on the turbine blades [15]. As mentioned earlier, the vortex cores break down and merge further downstream. This is in line with Figure 2.1 where vortex cores form helical structures in the near wake and disappear in the far wake. When the generated tip vortices of adjacent blades start to interact, the phenomenon of leapfrogging can occur. Leapfrogging occurs when two neighboring tip vortices, initially positioned in a staggered manner, begin to rotate around each other due to their induced velocities. This process causes the vortices to "leapfrog" past one another as they move downstream, continuously exchanging positions. The phenomenon can contribute to the breakdown of the vortex structure and increased wake turbulence further downstream. This can influence the energy extraction of downstream turbines in a wind farm. The wake can have additional turbulence due to the leapfrogging phenomenon, potentially enhancing wake recovery but also inducing greater mechanical loads on downstream turbines. The research by Lignarolo [16] shows that leapfrogging has a strong impact on the momentum deficit recovery of the wake.

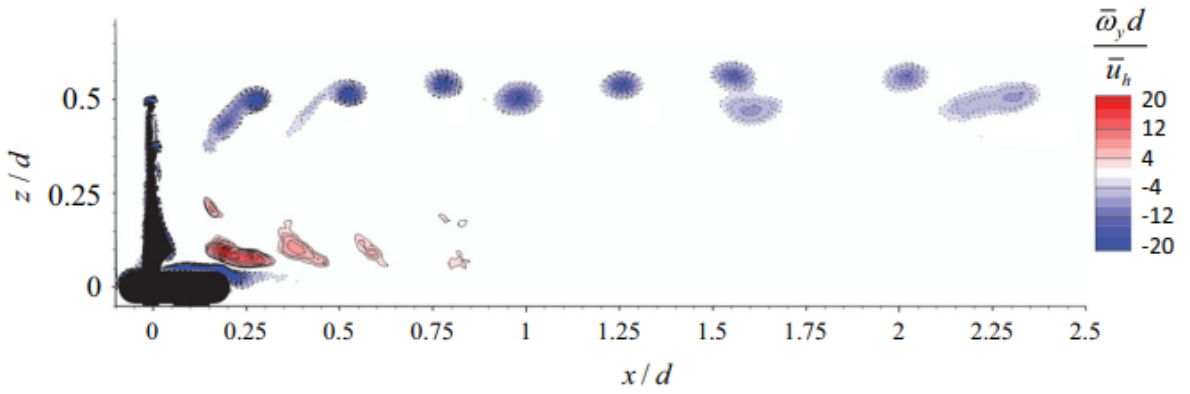

Figure 2.6: PIV measurements from the out-of-plane vorticity, figure retrieved from [10] originating from [17].

This section has examined the characteristics and wake recovery of a single turbine wake. It distinguishes between the near and far wake, reviews the velocity deficit behind the rotor, and discusses the wake recovery through turbulent mixing and leapfrogging. The typical length of a turbine wake is examined as well. These phenomena are crucial for understanding wind farm aerodynamics, which will be explored in the next section.

2.2. Wind Farm Aerodynamics

This section investigates the aerodynamics of wind farms as a whole. The first section of this chapter elaborates on the economic reasoning behind wind farm layout discussing important ratios such as capacity factor and capacity density. Wind farms can be categorized by different flow regions and this is discussed in the second section of this chapter. Finally, the predominant source of energy extraction for turbines further in the farm i.e., vertical entrainment, is considered.

2.2.1. Wind Farm Yield

While onshore wind turbines are easier to install and maintain, they pose significant challenges in densely populated countries like the Netherlands, particularly due to noise and visual impact. As a result, offshore wind farms have become a key source of sustainable energy. Additionally, the Netherlands plans to significantly expand offshore wind energy capacity by creating wind farms, outpacing the growth of onshore energy production [18]. The creation of these so-called farms allows for cheaper installation due to economies of scale. Additionally, there is more potential energy to be harnessed at sea because of the generally higher wind speeds [19]. Dupont et al. assess the Energy Return On Investment (EROI) for global wind energy potential [20]. The study indicates that the Netherlands has a high potential for harnessing energy in its offshore regions. Looking into this potential energy, the available maximum power from wind is determined by Equation 2.1.

$$P_w = \frac{1}{2}\rho A u_\infty^3 \tag{2.1}$$

This equation shows the extracted power relates to the wind speed cubed $P_w \sim u_\infty^3$. The relationship indicates that wind farm efficiency declines rapidly when turbines extract energy from the slow wind speed wake of upstream turbines. Figure 4 illustrates the time-averaged velocity profile for downstream turbines, highlighting the velocity deficit at hub height, resulting in power loss.

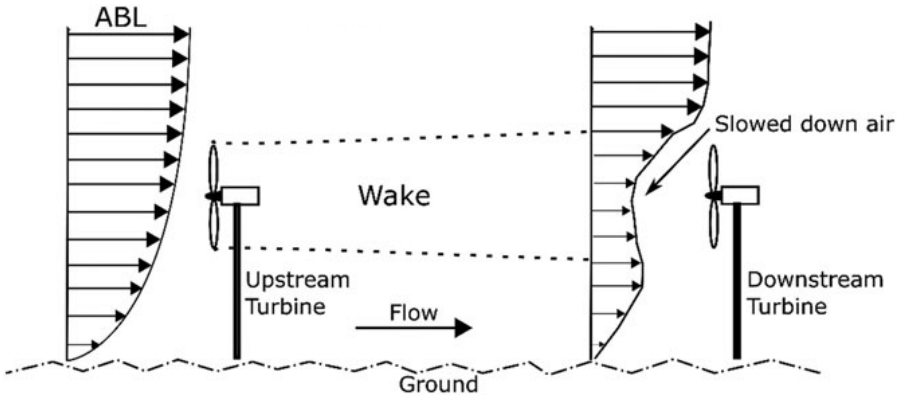

Figure 2.7: Wake effect on a downstream wind turbine, adapted from [21].

This power loss is shown in Figure 2.8. The graph displays the power generated by each turbine row, normalized to the output of the first row for the Horns Rev wind farm. In this case, the wind direction is aligned with the turbine array, allowing for the shortest possible inter-turbine spacing. For this specific wind farm, the inter-turbine spacing is seven times the rotor diameter which in short is stated as 7D. It is seen that from the second turbine row, the power production asymptotically drops to below 60% of the first turbine and does not improve for consecutive rows.

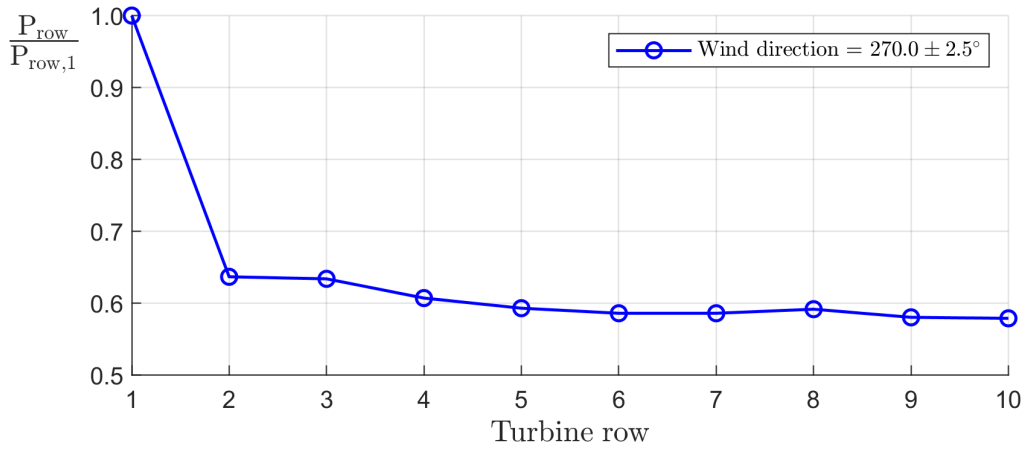

Figure 2.8: Power generated by each turbine row, normalized to the output of the first row when the wind direction is aligned with the turbine array. Inter-turbine spacing is 7D and the data is acquired from [5].

The capacity density of a wind farm is defined as the ratio of its rated capacity to the area of land it occupies. It is measured in megawatts per square kilometer ($\mathrm{MW/km^2}$).

$$\text{Capacity density} = \frac{\text{Rated turbine power x total number of turbines}}{\text{Total wind farm area}} \tag{2.2}$$

The rated turbine power is the maximum electrical output it can generate under optimal wind conditions, typically measured at a specific wind speed where the turbine operates at full capacity. A wind farm's capacity density alone is insufficient to conclude its energy production. To do this, the capacity factor of the wind farm must also be considered. The wind farm capacity factor is identified as the actual energy output in a year over the rated power production in a year.

$$\text{Capacity factor} = \frac{\text{Actual energy output in a year}}{\text{Rated energy output in a year}} \tag{2.3}$$

For a given wind site, a developer can select turbines that yield a capacity factor ranging anywhere from 1% to 99%, based on economic considerations. Weather is the primary influence on

capacity factors over short periods, such as minutes or months. However, these variations tend to average over a wind farm's 20 to 30-year lifespan. Thus, the long-term capacity factor is largely determined by the developer's trade-offs among the costs of turbine blades and structure, the mechanical and electronic components in the nacelle, the grid connection and installation expenses, and the wind farm layout.

Longer blades are more expensive but capture more wind, thereby increasing power generation. Conversely, lower maximum power ratings for the electrical and electronic components reduce costs, as well as the expense of grid connections. A developer might choose turbines with very long blades and low-rated electronics, which would achieve peak-rated power even in moderate wind conditions, but produce significantly less electricity most of the time. Alternatively, the developer could opt for shorter blades with electronics and grid connections rated for high power output. In this scenario, the turbine might never reach its peak power, leading to an average power generation of only 1% of the rated capacity, and a higher unit cost for the electricity produced. Thus, identical sites with identical wind conditions can yield capacity factors anywhere from 1% to 99%, depending on the design choices made.

Take the recently completed wind farm in the North Sea, located in the Hollandse Kust (noord) wind energy area as an example. The Kavel V wind farm, operational since 2023, consists of 69 turbines, each with a capacity of 11 MW, spread over an area of $126\ \mathrm{km}^2$. This results in a capacity density of $6.6\ \mathrm{MW/km}^2$. With an annual energy yield of $3.3\ \mathrm{TWh}$, the wind farm operates at a capacity factor of 50% [1].

The Dutch government is allocating new areas and setting capacity targets for future wind farms to meet their renewable energy goals. By 2030, they aim to have 21 GW of installed capacity across $2,600\ \mathrm{km}^2$ of sea[2]. This results in a capacity density of $8.1\ \mathrm{MW/km}^2$. The projected average energy yield by 2030 is 90 TWh per year, corresponding to an overall capacity factor of still 49%[3].

The last two paragraphs indicate that the capacity factor of future farms is assumed to remain equal to the recently commercialized wind farm Kavel V. However, the plans state that the capacity density will increase to at least $8.1\ \mathrm{MW/km}^2$, effectively decreasing the inter-turbine spacing. This estimate overlooks the significant impact of wake effects, which will lower the energy yield of the turbines and, in turn, reduce the capacity factor. As a result, this will decrease overall wind farm efficiency and decrease the revenue of offshore wind energy, eroding its competitive advantage.

To extend this further, even wind farm capacities of $10\ \mathrm{MW/km}^2$, are assumed to be possible by the the Dutch government[2]. However, research on cost analysis for the optimal wind farm capacity density using 10 and 15 MW turbines on Dutch offshore sites show that optimal wind farm capacity is in the range of 4.7 to $5.1\ \mathrm{MW/km}^2$ [22]. This requires wake losses to be minimized. Otherwise, the capacity factor of new wind farms will be significantly reduced. Resulting in high unit cost for produced electricity. Ultimately, if the wake loss effects are not addressed, high-capacity wind farms in the future won't be financially viable in the future.

2.2.2. Flow Regions Inside and Around a Wind Farm

To understand the aerodynamics of wind farms, the flow inside and around a wind farm can be identified by several regions [23]. These regions are identified as follows:

- **The wind-farm induction zone**
  The induction region, located immediately upwind of the wind farm, is where flow deceleration occurs due to the cumulative blockage effect of the wind turbines.
- **The entrance and flow development region**
  The entrance and flow development region starts at the first turbine of the farm. At this first turbine, the internal boundary layer (IBL) starts to develop. The IBL development originates

[1] https://www.crosswindhkn.nl/windfarm/
[2] https://windopzee.nl/onderwerpen/wind-zee/hoeveel-ruimte/
[3] https://windopzee.nl/onderwerpen/wind-zee/waar/

from the upward mass flow related to the wake expansion which follows from the deceleration of the flow. For large enough wind farms, the development of the IBL can influence the height of the Atmospheric Boundary Layer (ABL).

- **The fully-developed region**
  This region is characterized by the negligible change in flow properties in the streamwise direction. The height of the IBL and ABL remains constant. This region grows with the increasing size of wind farms and is discussed extensively in subsection 2.2.4.
- **The exit region**
  The exit region is located upstream of the final turbine of the farm. The IBL starts to reduce in height due to a downward mass flow related to the contraction of the wake. In the exit region, the flow velocity starts increasing again.
- **The wind-farm wake region**
  This region starts at the final turbine of the wind farm. The ABL reduces to its original height as the wake starts to recover and return to the inflow conditions.

Figure 2.9 shows the regions concerning a large finite-size wind farm.

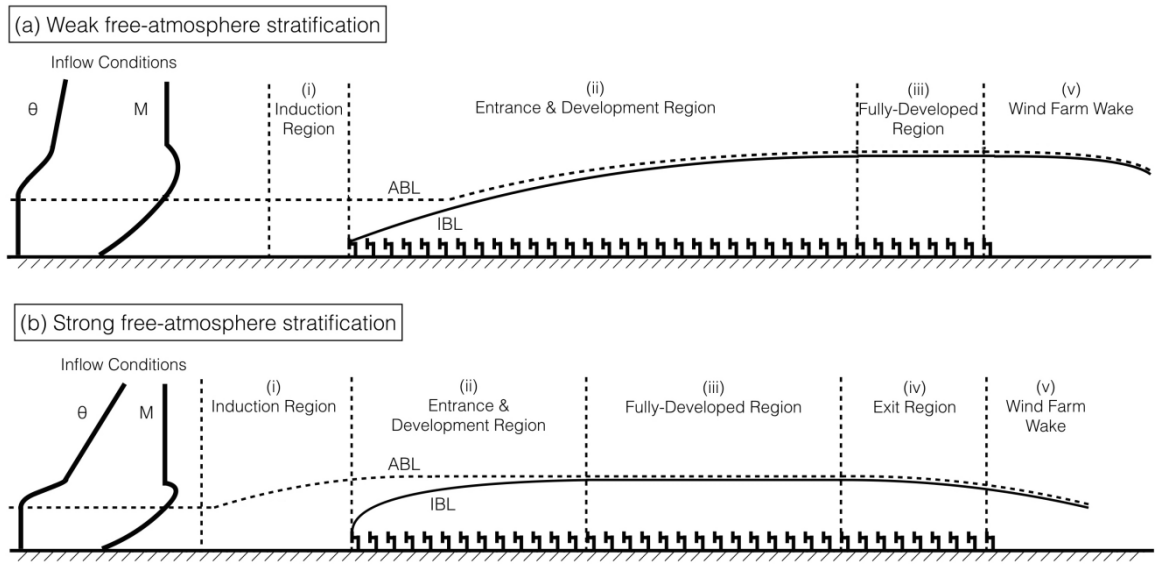

Figure 2.9: Flow regions in large finite-size wind farms where θ is the mean potential temperature and M is the mean wind speed. Figure retrieved from [23].

It is important to note that the free-atmospheric stratification influences the size of the flow regions. Weak and strong free-atmospheric stratification is influenced by the inflow conditions identified as mean potential temperature θ and mean wind speed M. For more information regarding free-atmospheric stratification see the book of Stull [24].

2.2.3. Deep Array Modeling

Deep array models are used to capture the extensive wake mixing deeper inside wind farms. This is done because single-wake models do not suffice anymore. These models only work when the wakes of single turbines can still be identified. Moreover, the wind surrounding the wakes can no longer be considered undisturbed. The deep array models consider wind turbines as added surface roughness. This approach leads to increased wind shear in the atmospheric boundary layer and lower wind speeds near the surface. Additionally, surface roughness generates turbulence. By modeling turbines as surface roughness elements, their large-scale impact on wind flow can be captured without needing to analyze the details of individual wakes. The effect of different surface roughness categories on the wind shear profile, as described by the logarithmic law, applies only to fully developed boundary layers like region (iii) in Figure 2.9. However, the

depth of interest within a wind farm can be too short for this full development. To address this, many deep array models use the concept of an inner boundary layer, which forms when surface roughness changes. This inner boundary layer grows over time, with wind shear determined by the new surface roughness. Meanwhile, the original boundary layer maintains its existing wind shear. At the top of the inner boundary layer, wind speed remains continuous, linking the inner and outer layers. This corresponds to the region (ii) in Figure 2.9.

Research on fully developed wind farms dates back to 1992 when Frandsen introduced a deep array model for estimating wind speed reduction by modeling wind turbines as effective roughness elements [25]. The research of Calaf [26] studies the Wind Turbine Array Boundary Layer (WTABL) systematically using a suit of LES. Comparing their case with the Frandsen study, they propose a slightly different approach to analytically model the infinite wind farm as roughness elements. Since the effects of thermal stratification were not taken into account by both of these models, Abkar and Porté-Agel modified the Frandsen model to account for the effect of free-atmosphere stability [27].

In deep array modeling, turbines act as effective roughness elements, meaning that higher-density wind farms with more turbines create greater roughness. This leads to reduced wind shear profiles, which in turn lowers capacity factors. The concept of deep array modeling therefore highlights the anticipated challenges associated with high-density wind farms.

2.2.4. Vertical Entrainment in Fully Developed Wind Farm Regions

Currently, the scale of offshore wind farms is increasing in size to an extent where the length of the wind farm exceeds the height of the ABL. This reduces the efficiency of wind farms as the wake effects cause significant reductions in energy capture. The generally dominant horizontal wind flows become disturbed and the turbines further in the wind farm rely for the largest part on vertical entrainment from the ABL for the exchange of momentum and energy [26]. Reaching the asymptotic limit of energy and momentum entrainment is called the "infinite" or "fully developed" wind farm. With the future capacity densities of offshore wind farms, this state is being reached sooner. Figure 2.10 shows the emergence of the fully developed WTABL where the turbulent entrainment of mean kinetic energy by the red arrows, indicates its vertical character.

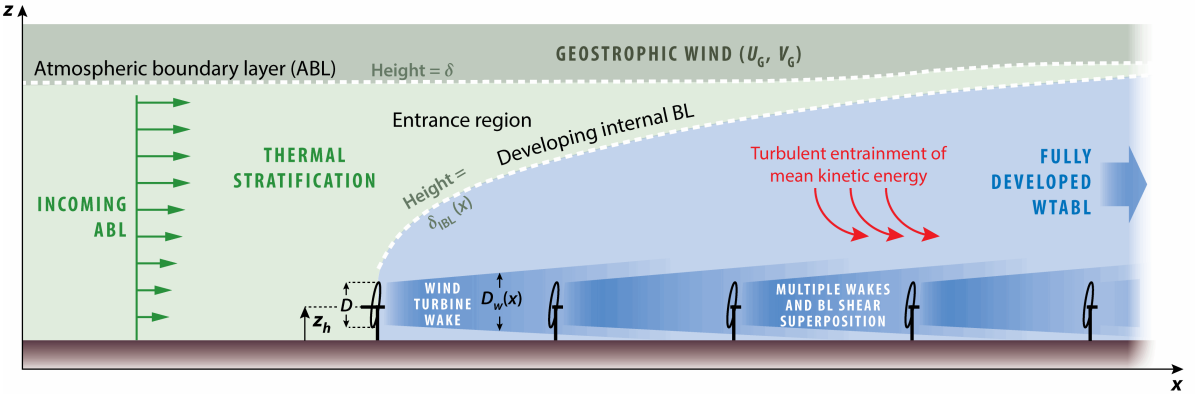

Figure 2.10: Illustration of interaction between the atmospheric boundary layer and large wind farms [28].

Meyers' research delves into the concept of momentum and energy transport tubes to analyze the three-dimensional mean fluxes of these properties in turbulent flows. These transport tubes are constructed using transport vector fields, incorporating the effects of Reynolds stresses and mean-flow viscous stresses. When transport processes are primarily driven by turbulence and Reynolds stresses, rather than mean-flow convection, these tubes provide a valuable way to visualize where momentum and energy originate and how they are transported. The study specifically examines stream-wise axial momentum and energy transport tubes in fully developed wind-turbine array boundary layers. The findings reveal that energy takes different paths to

reach wind turbines, depending on the turbine arrangement. There are two main energy transport mechanisms: a sideways flux and a top-down flux. Sideways fluxes are sustained by top-down fluxes in regions outside the turbine wake. In wind farms with larger span-wise turbine spacing, sideways energy fluxes dominate, whereas in setups with smaller spacing, the top-down mechanism becomes more prominent [29].

The study by Abkar also demonstrates that in the fully developed wind turbine region, the power extracted by the turbines is primarily balanced by the transport of kinetic energy, which is drawn from the flow above the farm and delivered to the region below. Consequently, the more energy entrained from the free atmosphere, the more power the turbines can generate. This indicates that any factors enhancing kinetic energy entrainment from the surrounding environment will lead to increased power production in large wind farms [30].

To connect the discussed literature with physical and aerodynamic principles, the Navier-Stokes equations serve as a general starting point. These equations describe the relationships between velocity, pressure, temperature, and density in a moving fluid. A specific variant, the Reynolds-averaged Navier-Stokes (RANS) equations, is commonly used to model turbulent flows, a key characteristic of wind turbine wakes as discussed in subsection 2.1.1. Since wind turbine wakes typically have Mach numbers below 0.3, density changes are less than 5%, justifying the assumption of incompressible flow [31]. For incompressible flow ($\nabla \cdot \mathbf{u} = 0$), the RANS equation in the component form combined with the identification of each term is shown in Equation 2.4.

$$\underbrace{\rho\left(\overline{u}_i \frac{\partial \overline{u}_i}{\partial x_j}\right)}_{\text{Advection}} = \underbrace{-\frac{\partial \overline{p}}{\partial x_i}}_{\text{Pressure}} + \underbrace{\mu \frac{\partial}{\partial x_j}\left(\frac{\partial \overline{u}_i}{\partial x_j}\right)}_{\text{Diffusion}} - \underbrace{\rho \frac{\partial \overline{u_i' u_j'}}{\partial x_j}}_{\text{Reynolds stress}} + \underbrace{f_i}_{\text{Body forces}} \tag{2.4}$$

In this equation:

- $\overline{u_i}$: Mean velocity in the i-direction (e.g., $\overline{u}$, $\overline{v}$, $\overline{w}$).
- $\overline{p}$: Mean pressure.
- ρ: Fluid density.
- μ: Dynamic viscosity.
- u_i': Fluctuating velocity component in the i-direction.
- $\overline{u_i' u_j'}$: Reynolds stress term for fluctuating velocities.
- f_i: External force in the i-direction.

Now, focusing only on the x-direction, as this is the main direction in which wind turbines exert their forces. The x-component (u-direction) of the RANS equations is written in Equation 2.5

$$\rho\left(\overline{u}\frac{\partial \overline{u}}{\partial x} + \overline{v}\frac{\partial \overline{u}}{\partial y} + \overline{w}\frac{\partial \overline{u}}{\partial z}\right) = -\frac{\partial \overline{p}}{\partial x} + \mu\left(\frac{\partial^2 \overline{u}}{\partial x^2} + \frac{\partial^2 \overline{u}}{\partial y^2} + \frac{\partial^2 \overline{u}}{\partial z^2}\right) - \rho\left(\frac{\partial \overline{u'u'}}{\partial x} + \frac{\partial \overline{u'v'}}{\partial y} + \frac{\partial \overline{u'w'}}{\partial z}\right) + f_x \tag{2.5}$$

When considering the case of an infinite wind farm, certain components have a negligible contribution to the equation. First, the contributions of viscosity (μ) are dropped as the Reynolds number is high ($Re > 10^7$). This is indicated by the blue zero. Next, the terms of x and y derivatives are dropped due to the infinite wind farm scenario, as the statistics are assumed to be stationary in both x and y directions. The red zeros indicate this. After removing these terms, we arrive in Equation 2.6.

$$\rho\left(\overline{u}\frac{\partial \overline{u}}{\partial x}+\overline{v}\frac{\partial \overline{u}}{\partial y}+\overline{w}\frac{\partial \overline{u}}{\partial z}\right) = -\frac{\partial \overline{p}}{\partial x}+\mu\left(\frac{\partial^2\overline{u}}{\partial x^2}+\frac{\partial^2\overline{u}}{\partial y^2}+\frac{\partial^2\overline{u}}{\partial z^2}\right)-\rho\left(\frac{\partial \overline{u'u'}}{\partial x}+\frac{\partial \overline{u'v'}}{\partial y}+\frac{\partial \overline{u'w'}}{\partial z}\right)+f_x \quad (2.6)$$

Then, based on the scale analysis for the flow in the wind farm, one can know that the scale of different terms can be listed in descending order as following [26], $\overline{u} > \sqrt{\overline{u'w'}} \gg \overline{v} \simeq \overline{w}$. Thus, the term $\overline{w}\partial\overline{u}/\partial z$ is inferior since its scale is smaller than $\partial\overline{u'w'}/\partial z$. Finally, Equation 2.7 has arrived, and this shows that the forces extracted by the wind turbines in a very large-scale wind farm are composed of the deficient vertical advection term and turbulence term. Both of these terms are contributing to vertical entrainment.

$$\underbrace{\rho\overline{w}\frac{\partial\overline{u}}{\partial z}}_{\text{Vertical advection}} + \underbrace{\rho\frac{\partial\overline{u'w'}}{\partial z}}_{\text{Turbulence}} = \underbrace{f_x}_{\text{Turbine forces}} \quad (2.7)$$

The key takeaway from this derivation is that the wake recovery resulting from the turbine forces mainly arises from turbulence, with a minor contribution from vertical advection. However, the importance of the vertical advection term will increase when the active enhancement of vertical flow into wind farms is examined in subsection 2.3.3. After discussing the aerodynamics of wind farms, the key takeaway from this chapter is that more vertical energy entrainment from the free atmosphere results in more power for the turbines to generate. This suggests that any factors enhancing the vertical advection will lead to increased power production in large wind farms.

2.3. Methods to Enhance Wind Farm Efficiency by Reducing Wake Losses

Where subsection 2.2.4 discusses the main problem for the efficiency loss in large wind farms, this section discusses solutions to increase wind farm efficiency by focusing on the acceleration of wake recovery. Solutions for improving wind farm efficiency can be categorized into two approaches: axial induction-based methods and wake redirection-based methods. Axial induction-based methods for wind farm efficiency focus on adjusting the turbine's operational settings to control the amount of wind energy extracted. This is done by altering the generator torque or blade pitch. By lowering the axial induction factor, turbines allow more wind to pass through, reducing the wake effects on downstream turbines and improving overall farm performance. This strategy balances energy capture with minimizing wake losses. More information regarding this method can be found in the research of Annoni [32], Knudsen [33] and Gebraad [34]. As this method does not actively redirect wakes within the wind farm, it is not a focus of this literature review, which concentrates on the latter approach. Wake redirection methods include rotor yaw, tilt, and vertical forcing. This chapter begins by highlighting the importance of optimizing wind farm layout to enhance power output, followed by a detailed discussion of yaw, tilt, and vertical forcing techniques. Among these, vertical forcing is a relatively new and less researched approach.

2.3.1. Wind Farm Layout Optimization

A common scenario where partial wake incidence and mixed wakes must be considered is when assessing a wind farm's power output as a function of wind direction. As the wind shifts from 0 to 360 degrees, the impact of wakes on total power generation varies. When the wind aligns with the rows of turbines, many turbines experience full wake effects due to overlapping wakes.

In contrast, other wind directions may result in fewer wake interactions, with wakes originating from turbines located further upstream.

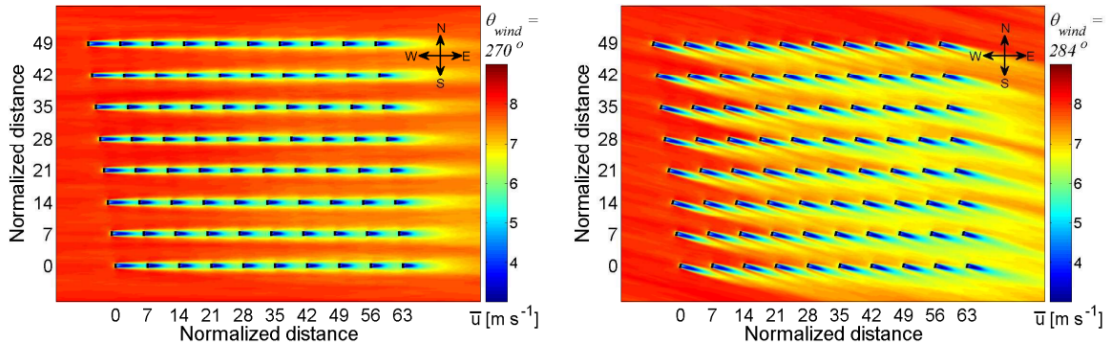

Figure 2.11: LES results of the mean flow velocity for two wind direction conditions [35].

To indicate the effect of changing wind direction on the power output of a wind farm. The research of Porté-Agel studies these effects on the Horns Rev wind farm near the Danish coast by performing LES [35]. Figure 2.11 shows the time-averaged streamwise velocity on a horizontal plane at hub height for incoming wind directions of 270° (left) and 284° (right).

The wind direction of 270° is aligned with the rows of turbines, resulting in an effective turbine spacing of 7D. As one would expect, the power generation of the farm would be low due to the wake losses. Figure 2.12 shows the normalized power for every turbine row in the Horns Rev wind farm. The results are based on observations [36]. When the wind direction changes to 285°, the wake from upstream turbines is perceived by turbines much further in the farm. This means that the effective spacing between turbines changes, and turbines 29D away are the first to encounter the wake from the upstream turbine. This indicates that the power generated by a wind farm for various wind directions is determined by the effective spacing between the turbines.

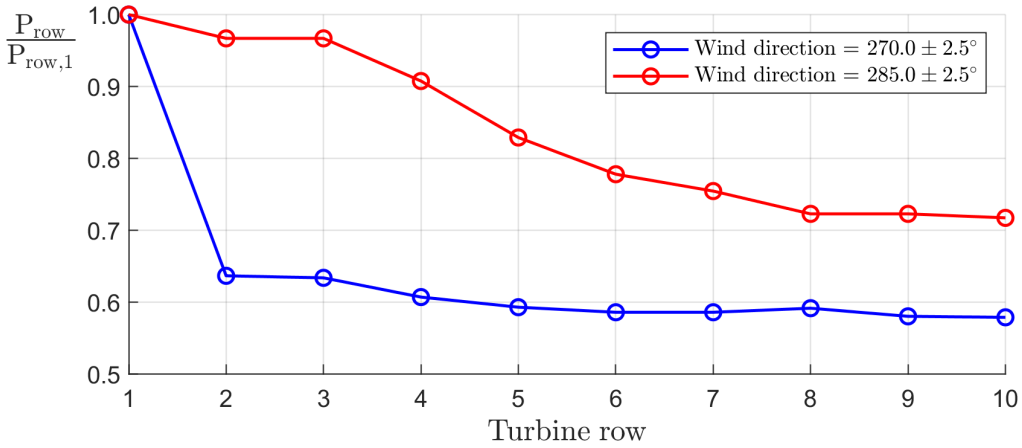

Figure 2.12: The power generated by each turbine row of the Horns Rev wind farm normalized to the power of the first turbine based on observations [36]. The effective turbine spacing is 7D for 270° and 29D for 285°.

A slight change in wind direction, from 270° to 285°, leads to a significant increase in the power output of all turbines across the wind farm. This 14° shift results in a 43% rise in normalized wind farm power output, increasing from 0.60 to 0.86 based on LES results [35]. This indicates the importance of wind farm layout optimization based on the wind rose of certain locations.

Archer's research shows that the staggered layout of the Lillgrund wind farm in Sweden improves overall power production. By staggering every second row of turbines, the wind farm's capacity factor increased from 0.30 to 0.34, based on large-eddy simulations coupled with an actuator line

model [37]. In general, staggered wind farms experience smaller wake effects, such as reduced power losses and lower fatigue loads on turbines. This is due to the greater effective distance between turbines in the wind direction, allowing wakes to develop with lower velocity deficits and reduced turbulence intensity before interacting with downwind turbines [10]. Additionally, wake-induced power losses decrease more gradually with downstream distance in staggered configurations compared to aligned setups. Although vertical kinetic energy entrainment is less concentrated in staggered farms, they benefit from more effective overall vertical energy entrainment. Hamilton's research shows that in staggered wind farms, the fourth row of turbines experiences a 7.5% higher vertical entrainment of high-momentum fluid compared to a standard cartesian grid. This increase is likely due to variations in the wake development between the different farm layouts [38].

The highlighted research articles demonstrate that wind farm layout influences vertical entrainment, the primary energy source for large wind farms. As a result, optimizing layout design is crucial for improving efficiency. Additionally, a wind farm's sensitivity to wind direction should be carefully considered when planning the layout to maximize performance. However, for the increasing size of wind farms, this application is mainly extending the infinite wind farm state instead of solving the issue of reduced power output in wind farms due to wake effects.

2.3.2. Rotor Yaw and Tilt Control

The rotor should be orthogonal to the flow for a single turbine to perform optimally. If this is not the case and a rotor has a yaw or tilt angle, the performance of the turbine drops, and greater structural loading occurs. Rotor yaw or tilt is therefore in principle a bad idea for an isolated rotor. However, it is a useful tool for increasing the total energy yield of multiple consecutive turbines. This is based on the principle that a single turbine performs less due to this setup, but multiple consecutive turbines perform better due to the increased wake recovery. In this section, yaw and tilt control will be addressed.

The distribution of far-wake flow and wake deflection under yawed conditions indicates that wake deflection increases as the wake moves further downstream. This is illustrated in Figure 2.13, which presents contours of the normalized streamwise velocity on a horizontal plane at hub height for a turbine yawed at 20°, based on wind-tunnel experiments. Wake deflection is influenced by several factors: higher yaw angles, increased thrust coefficients, reduced incoming turbulence intensity, and enhanced thermal stability. These findings indicate that employing yaw-angle control for wind turbines is particularly advantageous in offshore wind farms or in environments characterized by stable boundary layers [10].

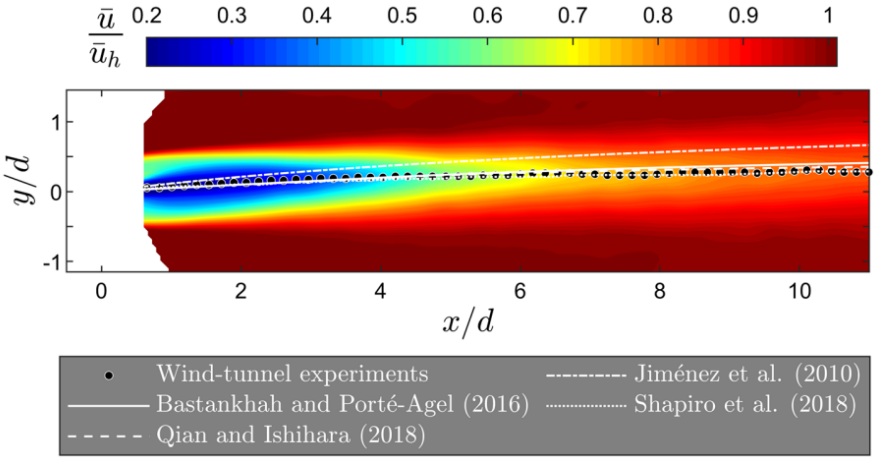

Figure 2.13: Contour plot showing normalized streamwise velocity from a rotor with a 20° yaw angle. Also, wake center trajectories are shown based on analytical models and wind tunnel experiments [10].

To study the behavior of rotor yawing applied to wind farms, the study of Archer [39] investigates a wind farm with 28 turbines using LES to quantify and optimize power gains while minimizing losses. By intentionally misaligning selected turbines in the front, middle, and back rows with positive (counter-clockwise) or negative (clockwise) yaw angles, the research finds that positive yaw angles lead to net power gains, while negative angles result in losses. The hypothesis suggests that this effect is linked to the Coriolis effect, indicating that only positive yaw misalignment should be used for wake steering in the northern hemisphere. The research highlights several key findings:

- The potential benefits of wake steering stem from both wake deflection and the narrowing of the wake.
- When the yaw misalignment angle is negative (clockwise), the power losses at the misaligned turbine outweigh any gains at downstream turbines.
- Positive yaw misalignment angles require at least two downstream turbines to achieve statistically significant net power gains.
- Misaligning the yaw angle of turbines in the front or deep rows effectively increases overall wind farm power production, whereas misaligning mid-row turbines is less effective.

More research on turbine yawing using an actuator surface is done by Howland [40]. This study investigates wake deflection behind a porous disk model of a wind turbine under yawed conditions using wind tunnel experiments and uniform inflow. Velocity distributions measured at different downstream positions confirm that the non-rotating porous disk model accurately replicates realistic wake deflections, consistent with other studies.

Controlling the tilt angle has emerged as another research topic for optimizing wake redirection and improving wind farm efficiency. A study on the Princess Amalia wind farm explored increasing Annual Energy Production (AEP) by tilting the rotors [41]. The findings showed that using fixed tilt angles led to a 2.77% increase in AEP, while implementing active tilt control achieved a more significant improvement, boosting AEP by 13.64%.

To investigate how the wake behind a yawing or tilting rotor behaves, the research of Flemming is studied [42]. The paper presents high-fidelity simulations of a two-turbine fully waked scenario to explore various wake mitigation strategies. These strategies include adjusting the yaw and tilt angles of the upstream turbine to induce wake skew and repositioning the downstream turbine. The simulation outcomes are evaluated against a baseline operation, focusing on changes in overall power capture and turbine loading for both upstream and downstream turbines. The repositioned and tilted case ensures higher power outputs relative to the yawed case. Figure 2.14 shows the simulated wake cases and the baseline case.

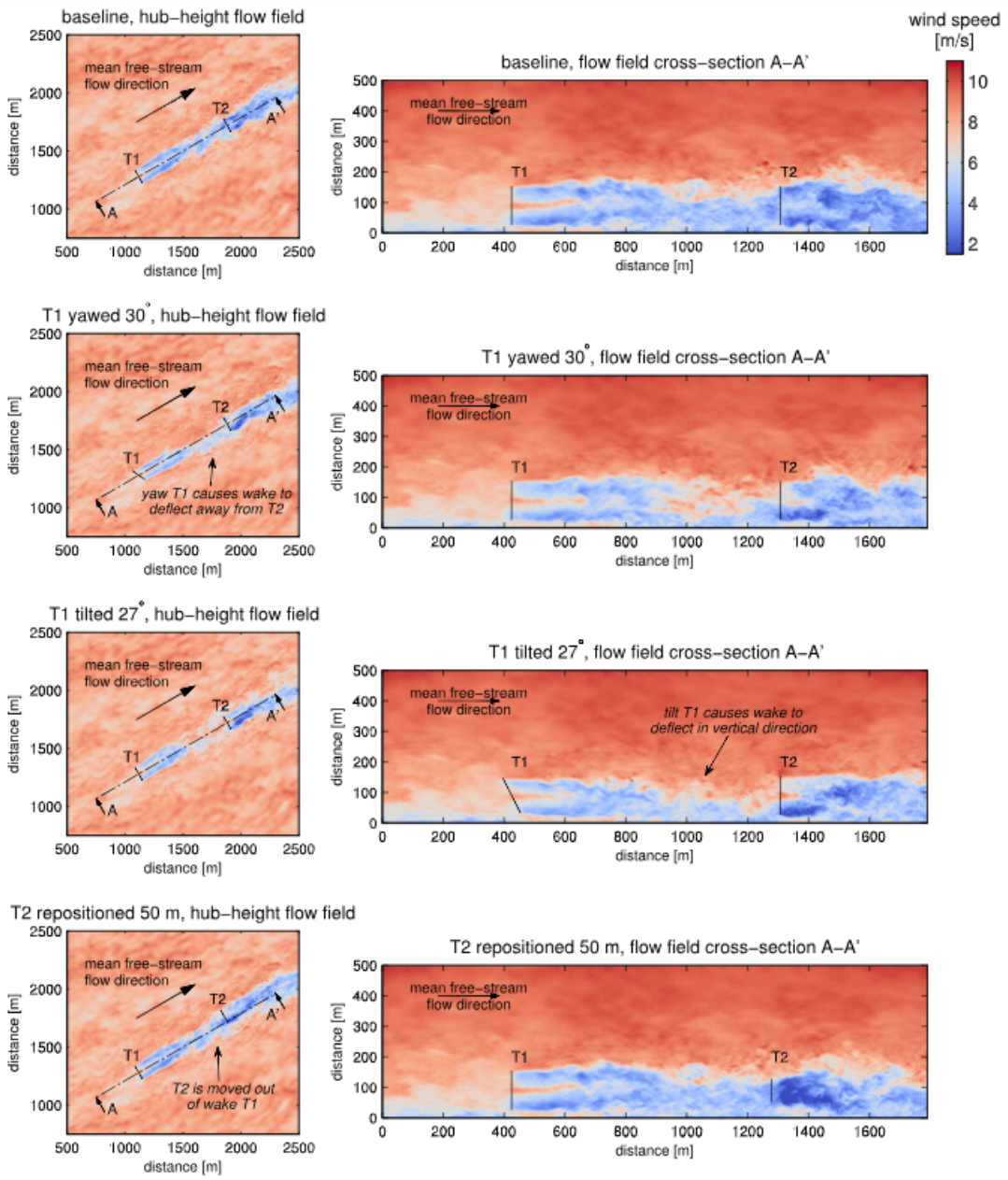

Figure 2.14: Velocity fields generated by SOWFA, T1 indicates the upstream turbine and T2 the downstream turbine [42].

2.3.3. Vertical Forcing

So far, we have discussed wake redirection methods using rotor yaw and tilt, both aimed at improving wind farm efficiency. As wind farms continue to grow in size, the fully developed region of the farm becomes more significant. In this region, the flow becomes well mixed, and the turbine wakes are able to recover less. As noted in section 2.2, this region receives its energy from vertical entrainment. This raises the question of whether enhancing vertical forcing could further boost wind farm efficiency. Additionally, increasing velocity fluxes in the vertical direction could be advantageous, something that rotor yawing does not achieve and rotor tilting only partially addresses.

With the knowledge gained, Bader investigates using airfoils positioned behind actuator disks to implement the concept of vertical forcing through simulations [21]. This article explores potential external modifications to improve wind turbine performance in a farm setting. The ap-

proach involves redirecting each turbine's wake downward and away from the turbines behind it. This is accomplished by placing stationary external airfoils near the rotor area. Various designs are tested using Reynolds-Averaged Navier-Stokes simulations for an aligned array of two wind turbines. In these simulations, the turbines are modeled as actuator disks with axial induction, positioned within a turbulent atmospheric boundary layer. Figure 2.15 shows one of the ten simulation cases in which airfoils are placed near the rotor area.

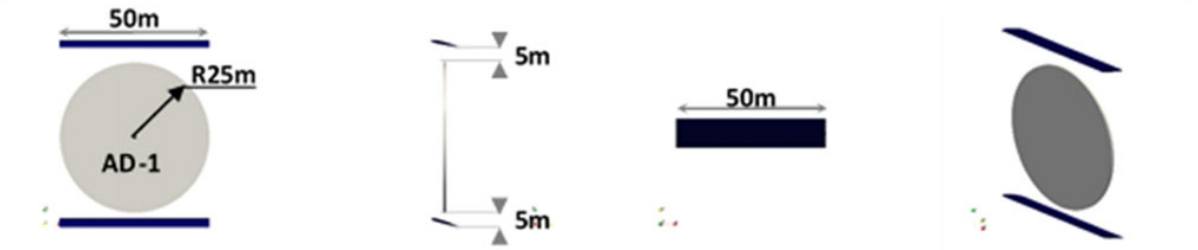

Figure 2.15: One of the ten device configurations [21].

The study shows that the use of fixed external airfoils can enable partial or even complete power recovery at turbine separations as close as 3 rotor diameters downstream. The velocity deficit parameter (VDP) is used to quantify the recovery rate. In the baseline case without wings, the velocity deficit was found to be 16.5%. With the airfoil device shown in Figure 2.15, the VDP improved to 11.6%, indicating better wake recovery. The best result, with a VDP of 4.1%, was achieved using a circular airfoil that forced the wake downward. Another effective case with simpler straight airfoils resulted in a VDP of 7.4%, involving three horizontal airfoils positioned behind the actuator disk at almost 1D distance. Another finding from the study shows that certain devices can also enhance the performance of the upstream turbine. This happens because of the shapes of some devices, mimicking diffuser shrouds and therefore creating negative pressure areas behind the rotor. This consequently admits more air through the rotor. The designs where this happens are the circular and vertical airfoil cases. In conclusion, the use of airfoils near the rotor area can improve the performance of downstream turbines by directing the wake downward. Additionally, certain airfoil designs can also have a positive impact on the upstream turbine.

Building on insights from the previous study and Ferreira's novel idea, enhancing vertical forcing using lift-generating devices presents an interesting research opportunity for improving wind farm efficiency. To illustrate how this concept might be applied in practice, Figure 2.16 shows a rendering of the proposed design. The concept involves a Multi-Rotor System (MRS) of horizontal-axis wind turbines. However, vertical-axis wind turbines can be used equally simply. The support structure of the MRS provides the opportunity to incorporate lift-generating wings in the design. By leveraging the primary advantage of the MRS, these wind harvesting devices can be scaled up to heights of 300 meters while maintaining the same blades and generators, benefiting from economies of scale. The lift-generating airfoils can even work as structural parts in the design.

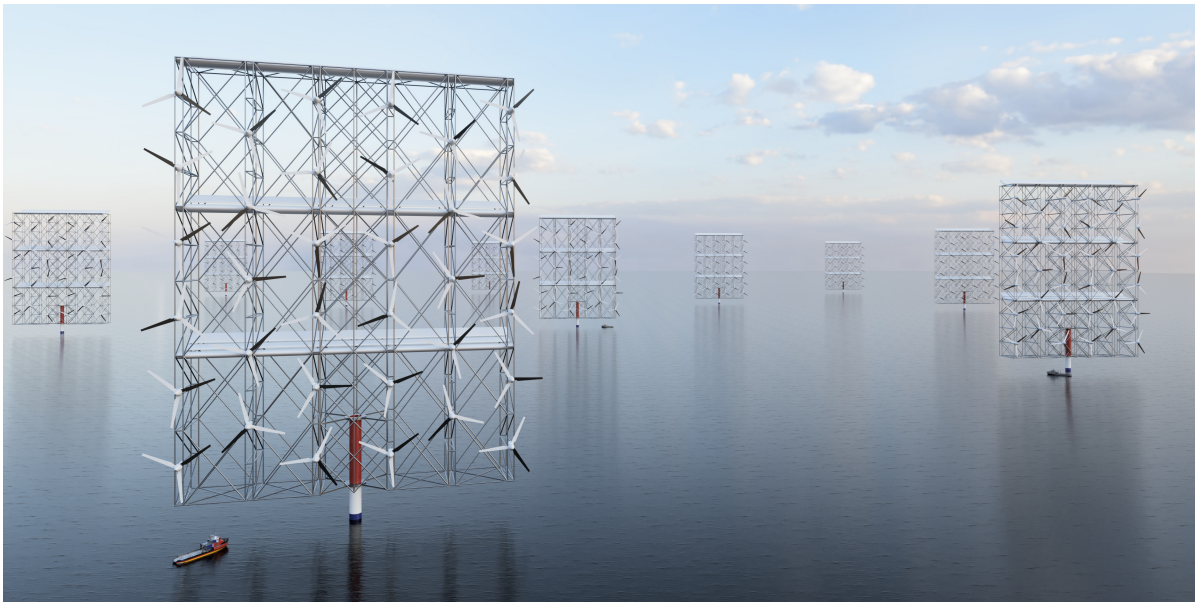

Figure 2.16: Future perspective of a Wind farm of multi-rotor systems with enhanced vertical forcing using lifting devices in the construction.

Based on this concept, the work of Broertjes investigates vertical forcing combined with an MRS of Vertical Axis Wind Turbines (VAWT) in an experimental setup [43]. The device used for the wind tunnel experiments makes use of two wings. One wing is situated at the top of the MRS while the other is placed in the middle. The setup can be seen in Figure 2.17.

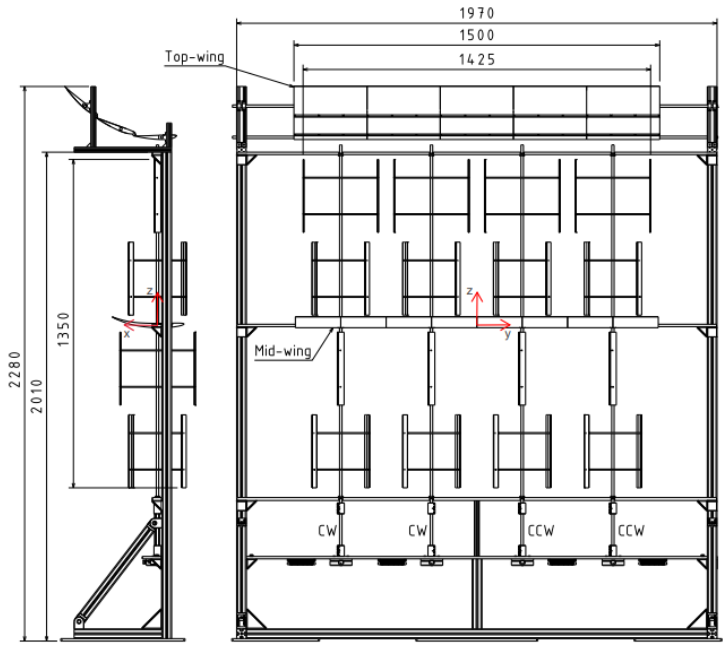

Figure 2.17: Experimental MRS with wings mounted in the middle and at the top, dimension in millimeters [43].

The study examines load measurements, streamwise velocity, vorticity, momentum, and power recovery. In terms of load measurements, a 2% to 3% increase in the thrust coefficient was observed when the wings were mounted. This is attributed to the suction sides of the airfoils, which

effectively accelerate the flow reaching the turbines. The results for the streamwise velocity are presented in Figure 2.18.

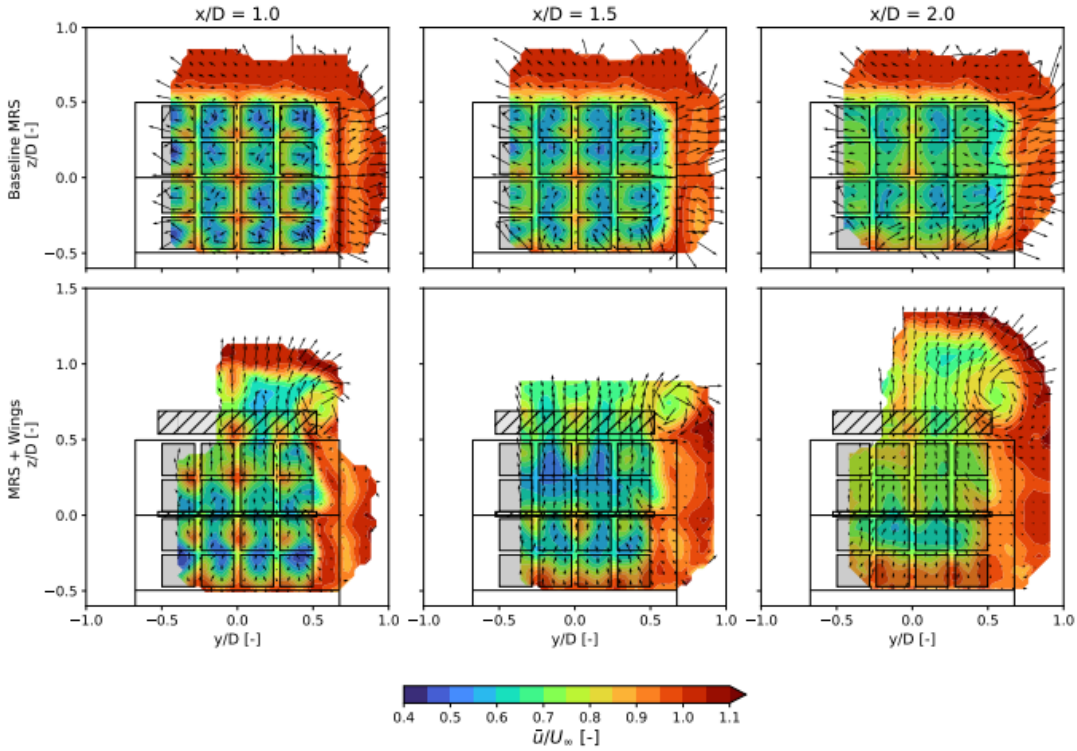

Figure 2.18: Contours of the normalized streamwise velocity for the MRS without wings (top row) and with external wings (bottom row) at x/D = 1.0, 1.5, and 2.0. The vectors indicate in-plane velocities [43].

In this figure, x/D represents the streamwise distance behind the MRS, where D is the width of the MRS. In the baseline case, the wake expands laterally as it progresses downstream but remains centered behind the actuator plane. However, once external wings are added to the MRS, the wake behavior changes significantly. The wings introduce both upwash into the flow and tip vortices at the wing tips. As a result, these effects energize the wake region through the sides of the MRS, enhancing the wake recovery. In the MRS configuration with wings, the vorticity field is primarily influenced by the strong tip vortices generated by the external wings, rather than the individual tip vortices from the rotors. The study highlights that wake evolution is influenced not only by advection but also by the interaction and entrainment effects of tip vortices from the lifting devices. However, when examining streamwise momentum recovery, it becomes clear that advection plays the dominant role. The analysis of power recovery further reveals that the wake behind the MRS equipped with wings recovers more quickly than in the baseline configuration at all three downstream locations.

Broertjes' research focuses on the near-wake region, extending up to twice the width of the actuator surface. In wind farms, however, the typical inter-turbine spacing ranges from 5 to 10 times the rotor diameter. Therefore, to properly assess the aerodynamics in wind farms, it is crucial to study the wake further downstream. Additionally, the cumulative aerodynamic effects of multiple wind turbines can only be analyzed by creating a wind farm in an experimental setup. Pre-published Computational Fluid Dynamics (CFD) work from Li investigates the infinite wind farm with and without lifting devices configured.

The research utilizes CFD simulations in OpenFOAM, employing the RANS approach. A wind farm model consisting of 3 columns and 5 rows was created, with an inter-turbine spacing of 6D in the streamwise direction and 5D laterally. The turbines were modeled as actuator disks, each

equipped with four lifting devices based on the S1223 airfoil profile. The study explores three configurations: without lifting, upward lifting, and downward lifting. The streamwise velocity results of this study can be seen in Figure 2.19.

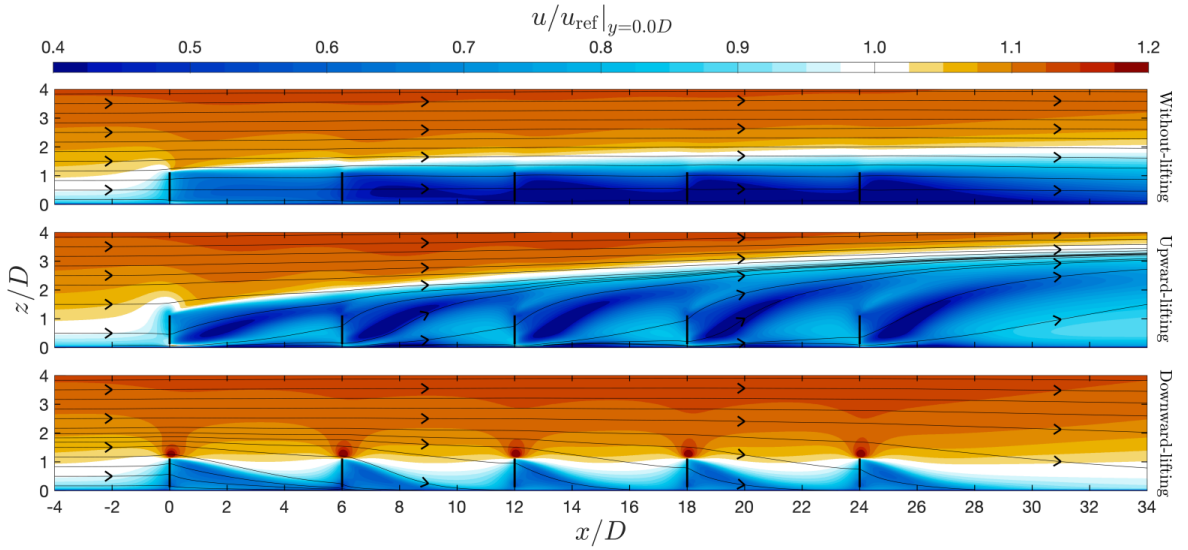

Figure 2.19: Contours of streamwise velocity u of the wind farms for the three cases, thick black lines represent the positions of the systems.

In this contour plot, the without-lifting case approximates the aerodynamics of wind farms of today. A large region with slow wind speeds develops in the farm while faster moving wind goes over the wind farm without much interaction between the layers. The upward and downward lifting cases show much more interaction by entraining larger amounts of momentum from the area above the wind farm. The normalized thrust forces on the actuator surfaces from the last row show 40% thrust relative to the first surface. For the upward and downward lifting cases, this thrust is increased to 80%. Moreover, the relative power densities for the upward and downward lifting cases almost double relative to the without lifting case. To conclude, the results and analysis from this study suggest that wind farms could potentially have much higher efficiencies than their conventional counterparts, revolutionizing the off-shore wind energy sector. The concept of vertical forcing in wind farms is known as "regenerative wind farming". Regenerative wind farming aims to increase the total energy output of a wind farms by actively interacting with the ABL while minimizing the utilized area. It represents an innovative approach to wind energy generation, seeking to make the most of the available wind resources by rethinking how turbines interact with the wind and each other.

This section on vertical forcing highlights its potential to enhance wind farm efficiency and introduces the concept of regenerative wind farming. While wind farm layout optimization, as well as rotor yaw and tilt adjustments, can introduce significant improvements for smaller wind farms, their impact diminishes as wind farm size increases. This is because these optimization methods extend, rather than solve, wind farm wake losses. Vertical forcing, on the other hand, presents a promising solution to wake loss issues in larger wind farms, as demonstrated by the research of Ferreira [7], Bader [21], Broertjes [43], and Li.

Additionally, Broertjes' experimental near-wake study and Li's CFD calculations for wind farms reveal a research gap: the need to assess vertical forcing in a wind farm setup using wind tunnel testing. Conducting experiments in such a setup would provide the opportunity to assess the concept with physical accuracy, capture complex turbulence interactions, and serve as validation for CFD models.

2.4. Experimental Elements

As identified in the previous section, an experimental approach is needed to address the research gap. This chapter explores the essential components required to conduct such an experiment. Given that small-scale wind turbines can be complex and costly, the use of actuator surfaces is examined. To implement vertical forcing, lift-generating devices will also be required. Due to scaling constraints, this necessitates high-lift wings, which will be reviewed in this chapter. Lastly, a suitable flow quantification technique applicable to wind farm experiments is assessed.

2.4.1. Actuator Surface

When scaling wind turbines, the Tip Speed Ratio (TSR) is a common scaling parameter that is defined in Equation 2.8.

$$TSR = \frac{nR}{u} \tag{2.8}$$

Since the blade radius R is significantly smaller in wind tunnel testing, the wind speed u needs to be reduced, while the rotor's rotational speed n must be increased. To maintain the same tip speed ratio (TSR) in these conditions, the rotors need to be powered, which requires small electronic components and intricate designs. This can become prohibitively expensive and complex for wind tunnel testing. As a result, actuator surfaces are often used instead. These porous shapes mimic the aerodynamic behavior of HAWTs. The aerodynamics of actuator surface wakes have been extensively studied [40, 44]. Lignarolo et al. [45] demonstrated that these devices can replicate key aerodynamic parameters, such as velocity, pressure, and enthalpy fields when the thrust coefficient is matched to that of wind turbines. Consequently, the use of actuator surfaces has become a widely adopted tool for simulating wind farm behavior [46]. These features make porous plates a suitable and significantly simpler surrogate for wind turbines. Additionally, Steiros and Hultmark [47] developed a model that relates the drag force on the actuator surface to its porosity. A part of Huang's study explores the use of actuator surfaces as replacements for VAWTs [48]. It is important to note that for both HAWTs and VAWTs, the near-wake vortex systems differ when using actuator surfaces. For instance, actuator surfaces do not generate the tip and root vortices induced by HAWTs or the vortices formed around the blade tips of VAWTs.

2.4.2. High Lift Wings

A full-scale offshore MRS in the future could have dimensions up to 300 meters in both width and height. Since full-scale wind tunnel testing is not feasible, downscaling is necessary to fit the wind tunnel while maintaining accurate inter-turbine spacing. This requires the wind tunnel model to have an actuator surface of approximately 0.3 x 0.3 meters. To ensure the aerodynamic characteristics remain realistic, scaling laws must be applied, with the Reynolds number, described in Equation 2.9, being one of the key scaling parameters. The Reynolds number represents the ratio of inertial forces to viscous forces within a fluid flow.

$$Re = \frac{\rho u L}{\mu} \tag{2.9}$$

In this equation, ρ represents the density, u is the wind speed, L is the characteristic length, and μ is the dynamic viscosity. Assuming the density, velocity, and dynamic viscosity can be kept similar between real-life conditions and wind tunnel testing, the width of the actuator surface is used as the characteristic length in the Reynolds number equation. Since this is scaled at a 1:1000 ratio, the Reynolds number will be reduced by a factor of 1000 in wind tunnel testing. Theoretically, increasing the velocity by a factor of 1000 could maintain the same Reynolds number, but this is impractical as it would lead to supersonic flow, which would alter the fundamental aerodynamic behavior. As a result, the wind tunnel tests will necessarily be conducted at a lower Reynolds number.

At low Reynolds numbers, the lift coefficient generated by a wing decreases due to reduced inertial forces in the flow. This happens because a lower Reynolds number often means that the boundary layer is more prone to earlier transition and separation. Several strategies can be employed to address this issue. A good starting point is to refer to the lift force equation in Equa-

tion 2.10.

$$L_f = \frac{1}{2}\rho C_L A V_\infty^2 \tag{2.10}$$

Assuming constant wind speed and air density, two variables can be adjusted to maintain a sufficient lift force: the area A and the lift coefficient C_L. Since the spanwise length of the wing is constrained by the width of the actuator surface, increasing the chord length and modifying the lift coefficient are viable options to achieve higher lift. This explains the need for high-lift wings in this experimental approach. Where adjusting the chord length is a simple method, this only involves enlarging the airfoil shape, altering the lift coefficient requires a deeper understanding of airfoil theory. Smith's work offers valuable insights into high-lift aerodynamics and the use of multi-element airfoils to achieve high lift coefficients [49].

2.4.3. Particle Image Velocimetry

Particle Image Velocimetry (PIV) is a non-intrusive flow quantification technique. It involves injecting tracer particles into the flow, ranging from tiny particles produced by smoke machines to larger, non-buoyant helium-filled soap bubbles (HFSB) introduced through seeding rakes. These particles are illuminated using a laser or LED source, and their movement is tracked by high-speed cameras, which capture the light reflected by the particles. The main advantage of this technique is the high spatial resolution meaning it is capable of instantly measuring an entire velocity field or volume. There are three main types of PIV:

- Planar PIV
  This method utilizes a single camera and a thin laser sheet, allowing for the measurement of two velocity components within a 2D domain. The research from Scharnowski considers classical operating rules from a recent perspective and proves their validity. Additionally, conditions for using stereo or tomographic PIV are established [50].
- Stereo PIV
  This method utilized two cameras and a thin laser sheet, allowing for the measurement of three velocity components within a 2D domain. To review an application of this method, refer to Tescione et al [51]. This study applies stereo PIV in the near wake of a VAWT.
- Tomographic PIV
  This method utilizes three or more cameras and a thick laser sheet or LED unit, allowing for the measurement of three velocity components within a 3D domain.

Tomographic PIV is the most suitable technique for wind farm experiments of this kind due to its ability to cover large volumes of interest and investigate multiple orientations of planes within the wind farm. This technique was first introduced in 2006 by Elsinga et al. [52], while Scarano's review provides an overview of its usage and the most relevant applications in fluid mechanics [53]. Figure 2.20 illustrates the working principle of tomographic PIV. Three or more cameras capture the scattering of particles illuminated by the laser within the measurement volume. The individual images are then reconstructed into 3D volumes through tomographic reconstruction. From these reconstructed volumes, the velocity vector field is generated using cross-correlation.

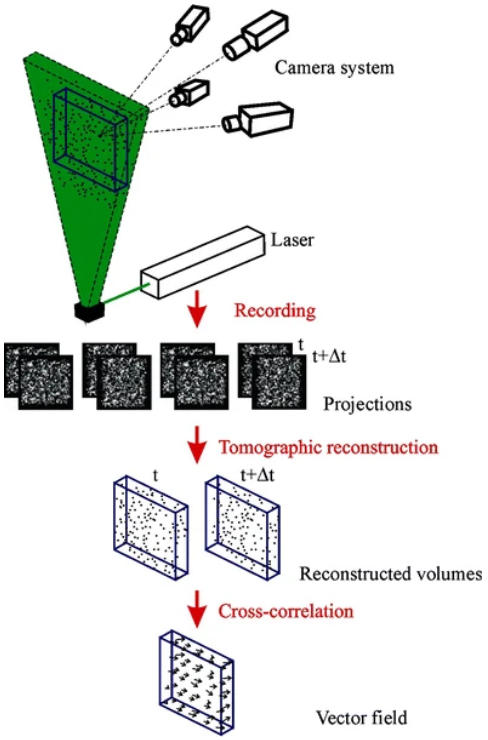

Figure 2.20: Working principle of tomographic PIV [52].

Particle Tracking Velocimetry (PTV) is closely related to PIV, but in this method, each individual particle is tracked by the software. Instead of using cross-correlation, advanced algorithms like Shake-the-Box (STB) are employed for particle tracking. STB is a lagrangian tracking method, which relies on time-resolved information to predict the position of particles. For a more detailed explanation of this method, refer to the work of Schanz et al. [54].

2.5. Research Design

The previous sections of this chapter have examined several key aspects of wind energy. First, the aerodynamics involving energy extraction by wind turbines were surveyed, followed by a review of wind farm aerodynamics. Possible solutions for enhancing wind farm efficiency through accelerated wake recovery were then discussed, with a focus on wake redirection-based methods. Additionally, the experimental elements chapter covered the elements needed for wind farm wind tunnel testing and the associated measurement setups. This section summarizes the main findings from earlier considerations and outlines the research objective of this master's thesis project. Finally, the research questions arising from the stated objective are presented.

2.5.1. Key Findings

The key findings of this chapter are listed below.

- The equation for the power from wind shows that the extracted power relates to the wind speed cubed $P_w \sim u_\infty^3$. The relationship indicates that wind farm efficiency declines rapidly when turbines extract energy from the slow wind speed wake of upstream turbines.
- Meeting offshore energy yield targets within the space allocated by the Dutch government will be financially challenging with the current wind farm performance. Increasing capacity density would result in lower capacity factors due to wake losses, ultimately making offshore wind more expensive.
- The scale of offshore wind farms is increasing in size to an extent where the length of the wind farm exceeds the height of the ABL. This reduces the efficiency of wind farms as the wake effects cause significant reductions in energy capture. The generally dominant hori-

zontal wind flows become disturbed and the turbines further in the wind farm rely for the largest part on vertical entrainment from the ABL for the exchange of momentum and energy. Reaching the asymptotic limit of energy and momentum entrainment is called the "infinite" or "fully developed" wind farm.

- Among wind farm layout optimization, rotor yaw and tilt strategies, and vertical forcing, the latter is less researched but highly impactful. While the other methods offer more modest efficiency improvements, vertical forcing demonstrates a huge potential for boosting overall wind farm performance.
- Ferreira's innovative concept incorporates lift-generating devices into the support structure of a large offshore MRS to create vertical forcing, while the experiment from Broertjes demonstrates the effectiveness of incorporating lift-generating devices to enhance streamwise momentum recovery.
- Li's CFD simulations reveal significant efficiency gains in infinite wind farms when lift-generating devices are integrated into a conventional wind farm setup.
- No experimental studies have been conducted to evaluate the aerodynamic performance of wind farms using lift-generating devices specifically designed to enhance vertical entrainment.

2.5.2. Research Goal

The key findings from the literature highlight the need for an experimental study on wind farms that utilize lifting devices to actively enhance vertical entrainment. Broertjes' experimental campaign demonstrates the potential of lifting devices by focusing on the near wake, while Li's CFD simulations show improved wind farm performance. Consequently, experimental testing is required to investigate far-wake behavior in a wind farm setup, particularly examining the velocity at downstream turbines.

The research objective is to find out whether the implementation of lift-generating devices is effective in improving wind farm efficiencies through increasing vertical entrainment by doing wind tunnel experiments. The experiment is designed to use arrays of meshed surfaces representing wind farms.

2.5.3. Research Questions

Building on the research objective and the key findings of this literature review, the following main research questions and the corresponding sub-questions are presented and will be answered by the conduction of wind tunnel experiments in the master thesis project:

- **To what extent can wind farm efficiency be improved by increasing vertical energy entrainment using lifting devices?**
  Since vertical entrainment plays a crucial role in large wind farms, this study explores whether vertical forcing through lift-generating devices can enhance wind farm efficiency. To assess efficiency improvements, key flow field characteristics must be examined, with a particular focus on wind speeds at hub height and vertical entrainment within the farm. Additionally, comparing the thrust values of downstream turbines to a reference case serves as an important indicator of overall wind farm performance. Ultimately, the impact of lift-generating devices on the closest actuator surface will also be evaluated.

  1. **What are the flow field characteristics of the wind farm with and without lifting devices configured?**
     This question aims to investigate how the presence of lifting devices affects the airflow within the experimental wind farm. From the flow field specifically, it seeks to understand factors like wind speed and vorticity both when lifting devices are present and when they are not.
  2. **What are the relative wind speeds inside the MRSL projection area and the vertical wind speeds in the wind farm, both with and without the lifting devices installed?**
     The relative wind speeds in the MRSL projection area are an important factor for iden-

tifying the effect of the lifting devices. Besides this, the literature research states the importance of vertical entrainment. With and without the lifting devices configured, the difference in vertical interaction can be identified using the vertical velocity data.

3. **What are the thrust values and the available power for the downstream turbines in the center column of the wind farm with and without lifting devices configured?**
   The thrust values on the actuator surfaces in the center column of the wind farm will be measured. This indicates the force difference with and without lift-generating devices configured. The available power can be identified by the velocity field.
4. **To what extent is there an interaction, between the lifting devices and the porous disk it is attached to?**
   The generation of lift involves the acceleration of flow, this accelerated flow can influence the thrust force on the actuator surface. Therefore, variation of thrust force in the presence of lifting devices should be investigated.

2.6. Concluding Remarks

This chapter has studied the literature on several key topics related to wind farm wake losses. First, the focus was on single wind turbine wakes and their recovery for foundational understanding, followed by a review of wind farm aerodynamics. This chapter highlighted the importance of vertical entrainment in fully developed wind farms, which directly relates to the power harvested by wind turbines. Methods to enhance wind farm wake efficiency were discussed, emphasizing the reduction of wake losses. Among these methods, wind farm layout optimization and rotor yawing and tilting ultimately postpone wake loss issues rather than eliminate them. In contrast, vertical forcing demonstrates significant potential gains for wind farms by actively enhancing vertical entrainment through advection terms. The concept of regenerative wind farming emerges from vertical forcing, utilizing atmospheric boundary layer interactions to increase total energy output while minimizing the overall area used. Recent studies conducted by TU Delft have identified a research gap in experimentally assessing vertical forcing within a wind farm layout. Additionally, experimental elements for such a study have been investigated. For the master's thesis project, the research goal and questions have been formulated based on the key findings of this chapter.

3

Designing the MRSL

This chapter shows the process of selecting the parameters for the MRSLs described in the previous chapter, which is based on preliminary wind tunnel tests. The primary objectives of these tests are to determine the airfoil profile for the MRSLs' wings, establish suitable pitch angles for the wings, and provide benchmark data to guide the final design of the MRSL. All of these investigations are being conducted in the presence of a porous disk, as it mimics an energy harvesting system.

3.1. Experimental Setup

The preliminary tests were conducted in a low-speed wind tunnel (W-Tunnel) at the Aerodynamic Laboratories of TU Delft prior to the main experimental campaign. The wind tunnel operates as an open-jet facility with an exit cross-section of $600 \times 600\,\mathrm{mm}^2$. Photos of the experimental setup are shown in Figure 3.1. In this figure, the porous disk which functions as an energy harvesting device, and the wings can be seen. It should be noted that the floor was not included in these preliminary tests. The coordinate axes x, y, and z correspond to the streamwise, vertical, and lateral directions of the MRSLs/regenerative wind farms as described in the main context.

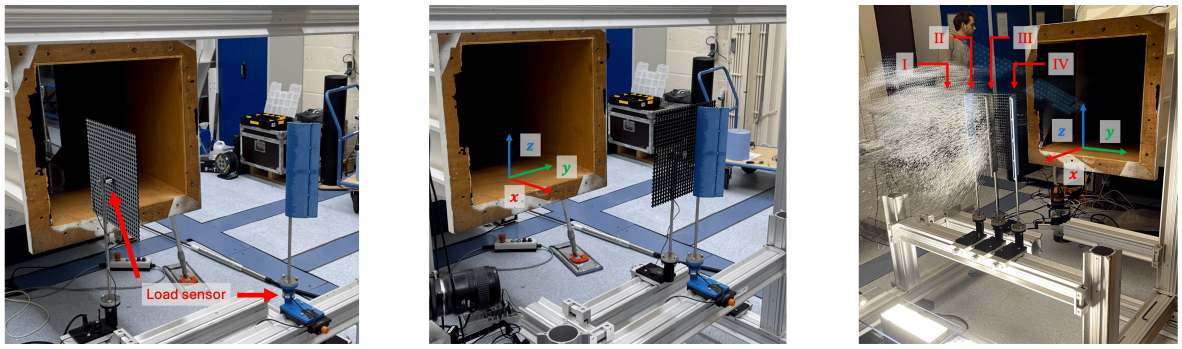

Figure 3.1: Left: Experimental setup for the preliminary tests to evaluate wing performance. The load sensors for both the wing and the porous disk are indicated by red arrows (the porous disk in this photo is positioned outside the jet). Middle: Setup for evaluating the combined performance of the single wing and the disk. Right: Photograph showing the positions of the loci for the wings. The configuration shown represents the Up-Washing configuration, with the wing at locus I absent. This photo was taken during the 3D-PTV measurements.

3.2. Evaluation of the Multi-Element Airfoil

This section benchmarks the performance of the MRSL's wings used in the final design, which are categorized as multi-element airfoils, and explains the rationale for selecting them over single-element airfoils. While single-element airfoils are simpler, multi-element airfoils may be preferred as they tend to offer higher maximum lift coefficients ($C_{l,\mathrm{max}}$) [55]. This high lift coefficient

is needed as it contributes to high lift forces. These high lift forces ensure the wake of energy harvesting devices is washed up or down and therefore reduce wake recovery. Thus, a two-element airfoil designed by [43] is selected as a candidate for the MRSL model. The airfoil configuration consists of two E423 airfoils [56] and it is optimized using the MSES software [57]. The profile of the two-element airfoil is shown on the left of Figure 3.2. Although multi-element airfoils that offer even higher $C_{l,\max}$ are available, this specific profile is chosen for its relatively simple structure (facilitating manufacturing), high thickness-to-chord ratio (aiding assembly and installation), and moderate camber (reducing flow blockage). Additionally, for comparison, a single-element S1223 airfoil (shown on the right of Figure 3.2) [58] is also tested to verify whether this two-element airfoil provides superior lift performance.

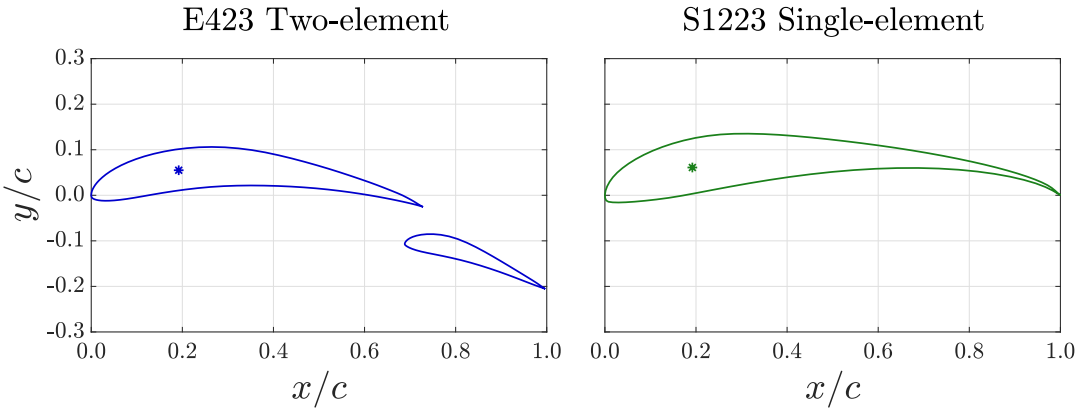

Figure 3.2: Left: The XY-plot depicts the multi-element airfoil used in this study, designed by [43] using the MSES optimization tool [57]. This configuration consists of two E423 airfoils [56]. Right: The XY-plot shows the single-element airfoil, S1223 [58], used as a reference to evaluate the performance of the multi-element airfoil employed in this work. The pitching axes for both airfoils are indicated with $*$ and are located at $(x/c = 0.192, y/c = 0.055)$ for the multi-element airfoil and $(x/c = 0.192, y/c = 0.061)$ for the single-element airfoil.

For both tested wings, the span and chord are set to 300 mm and 100 mm, respectively, matching the dimensions of the final MRSL design. Their performance is evaluated using three-dimensional lift and drag coefficients (C_l^{3D} and C_d^{3D}). The forces are measured using a six-axis force-torque sensor (F/T Sensor: mini40 with SI-40-2 calibration, ATI Industrial Automation), with an uncertainty of 0.01 N. The sampling rate is set to 500 Hz, and the measurements are conducted over a duration of 20 s. The wings and sensors are mounted on a frame (LINOS X95 System) using a combination of metal and 3D-printed components, as shown in Figure3.1.

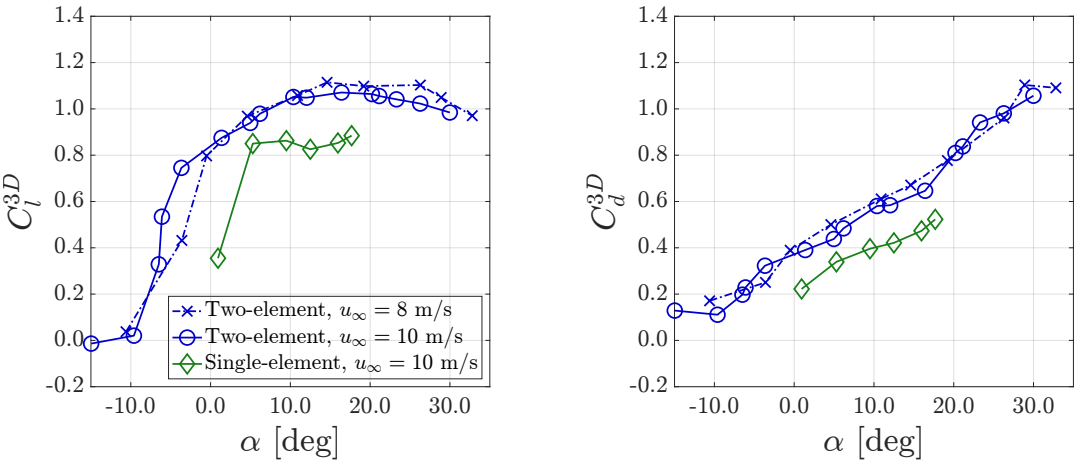

Figure 3.3: Time-averaged three-dimensional lift coefficients (C_l^{3D}) and drag coefficients (C_d^{3D}) measured in the preliminary experimental tests. The tested airfoils are shown in Figure 3.2, and the experimental setup is depicted in Figure 3.1. The uncertainties in C_l^{3D} and C_d^{3D} due to the load sensor are below 0.01, while the uncertainties in the angle of attack α are approximately $1°$.

The C_l^{3D} and C_d^{3D} values for both airfoil profiles are plotted against the angle of attack (α) in Figure 3.3. The tests are conducted at a reference velocity of 8 and 10 m/s for the two-element airfoil and 10 m/s for the single-element airfoil. This corresponds to Reynolds number of $Re = 55000$ and $Re = 68500$ for 8 and 10 m/s respectively. The additional 8 m/s test on the two-element airfoil was conducted under the assumption that this airfoil shape would yield a higher lift coefficient. The reduced speed ensures that the Reynolds number sensitivity is evaluated, making the testing of this two-element airfoil type more comprehensive and robust. The challenges when testing at such low Reynolds numbers originate from boundary layer behavior. At lower Reynolds numbers, the boundary layer tends to be thicker and can separate more easily. Early separation reduces the effective circulation around the airfoil, thereby lowering the lift coefficient. For this experiment, the difference in Reynolds number does not show an effect on its aerodynamic performance.

The angles of attack are measured before and after testing using a camera and image processing software (ImageJ [59]), with uncertainties estimated to be approximately $1°$. The positions of the pitching axes for the airfoils are indicated in Figure 3.2.

Based on the C_l^{3D} results presented in Figure 3.3, the maximum C_l^{3D} for wings with the two-element airfoil profile is 25% higher than that for wings with the single-element airfoil profile. According to classical lifting-line theory [31], stronger lift corresponds to a stronger induced vertical velocity behind the wing (commonly referred to as downwash), which is advantageous for MRSL performance [60]. As a result, the two-element airfoil profile is chosen for the final MRSL design, despite its significantly higher drag. The increased drag is primarily attributed to stronger induced drag and the larger surface area of the two-element configuration.

3.3. Selecting the Pitch Angles of the MRSL

The performance of the wing with the two-element airfoil profile, characterized by C_l^{3D} and C_d^{3D}, is evaluated under freestream conditions. However, because the wings of the MRSL model are expected to experience significant aerodynamic interactions with the porous disk, it is necessary to measure the loads of the wings and the porous disk when placed together. This approach allows the determination of the pitch angles θ_p for the wings based on the measured loads, with the goal of achieving the largest possible vertical (y-directional) force.

To independently measure the loads on the wings and the porous disk, it is essential to eliminate any solid contact between them. This is achieved using the setup shown in the middle of Figure 3.1. Additionally, the relative positions between the wing and the disk are expected to influence their aerodynamic interactions, making it necessary to measure the loads at every position where the wings may be mounted.

Prior to the experiment, it has already been determined that the MRSL will be equipped with three wings and both Up-Washing and Down-Washing configurations will be investigated. This is based on the assumption that the combined lift coefficient of the three wings will be sufficient, ensuring the feasibility of producing airfoils for the wind farm experiment. Additionally, it minimizes the orientation changes of the wings between Up-Washing and Down-Washing configurations, thereby reducing wind tunnel downtime during the regenerative wind farm experiment. Both configurations are tested, as unpublished CFD calculations by Li indicate that they significantly enhance wake recovery. Since the preliminary tests do not include a floor, some wing loci can be used for both configurations, reducing the number of required test positions to four. Specifically, for the Up-Washing configuration, the wings are placed at loci IV, III, and II as the top, middle, and bottom wings, respectively. For the Down-Washing configuration, the wings are positioned at loci I, II, and III as the top, middle, and bottom wings, respectively. The positions of these four loci are located at $-0.05D$, $0.32D$, $0.68D$, and $1.05D$, with the origin placed at the edge of the disk on the negative-y side. The positions of these loci are illustrated on the right side of Figure 3.1.

The (time-averaged) three-dimensional wing loads measured in the presence of the porous disk (with a porosity of 60%) are displayed in the left and middle panels of Figure 3.4. Here, C_y and C_x represent the vertical and streamwise force coefficients, respectively, as defined in Equation 3.1, with $u_\infty = 8$ m/s. Notation of C_l^{3D} and C_d^{3D} are not used here, as the presence of the disk com-

plicates and alters the inflow conditions, including the direction of the inflow. The results show that C_y for loci I, II, and III generally under-perform compared to cases without the disk. This is expected, as the porous disk slows down the flow, reducing the forces, a trend also observed in C_x. Interestingly, C_y for locus IV significantly outperforms the case without the disk. This can be attributed to the fact that the wing at locus IV is not shadowed by the porous disk. Additionally, the blockage effect of the disk accelerates the flow and alters its direction, which further enhances C_y for locus IV compared to conditions without the disk.

Regarding the maximum vertical force (maximum C_y) measured at different loci, it is observed that the maximum C_y for loci I, II, and III occurs around $\theta_p = 15°$, while for locus IV, it occurs at $\theta_p = 25°$. However, visualizing the flow field with smoke reveals severe flow separation at locus IV when θ_p is set to $25°$ to $10°$, which is only alleviated at $\theta_p = 5°$. Based on these findings, the pitch angles for the final design are set as follows. For the Up-Washing configuration, θ_p for top, middle, and bottom wings are all set at $-15°$. As for the Down-Washing configuration, θ_p are set to $5°$, $15°$, and $15°$ for top, middle, and bottom wings, respectively. The values of θ_p given here are those used in the final design described in section 3.5.

$$C_y \triangleq \frac{|f_y^W|}{0.5\rho u_\infty^2 cS}, \qquad C_x \triangleq \frac{|f_x^W|}{0.5\rho u_\infty^2 cS} \tag{3.1}$$

The thrust coefficient C_T of the porous disk, which is measured simultaneously with C_y and C_x, is presented in the right panel of Figure 3.4. The load sensor used for the disk is a unidirectional strain gauge (KD24s 10N, ME-Meβsysteme) capable of measuring tensile and compressive forces with a precision of 0.1 N. The sampling rate is set to $1,000$ Hz, and the sampling period is 20 s. The plot shows that the load on the disk is generally higher when the wing is positioned at loci III or IV compared to loci I or II. This result aligns with expectations, as the bound circulation of the wing alters the flow field around the disk. When the wing is situated at loci III or IV, its circulation system tends to accelerate the flow over the disk, whereas the circulation of the wing at loci I or II slows the flow down.

Interestingly, despite the additional blockage and drag introduced by the wing, the presence of a wing at loci III or IV can result in higher loads on the disk compared to a stand-alone disk. This happens due to the acceleration of flow induced by the wing. The phenomenon is also observed in measurements of the thrust force for the Up-Washing configuration in Section 5.1. These observations highlight the significant aerodynamic interactions between the wings and the porous disk in the MRSL model.

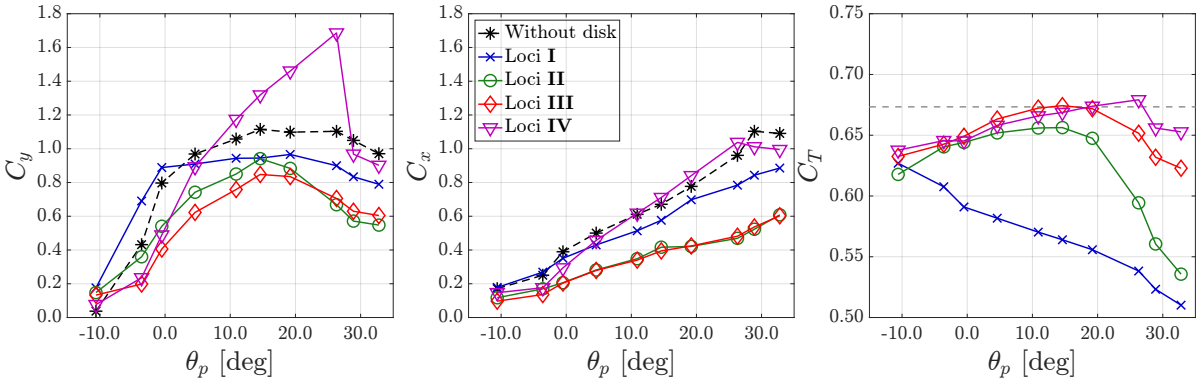

Figure 3.4: Left and Middle: Time-averaged three-dimensional wing loads measured in the presence of the porous disk (porosity: 60%). Note that only a single wing (two-element airfoil) is placed during the measurements, as depicted in the middle panel of Figure 3.4. Wing loads are measured at different positions, with the loci positions illustrated on the right of Figure 3.4. C_y and C_x denote the vertical and streamwise force coefficients, respectively, as defined in Equation 3.1. The uncertainties of C_x and C_y due to the load sensor are below 0.01, while the uncertainties in the pitch angle θ_p are approximately $1°$. Right: The corresponding thrust coefficient C_T measured simultaneously with C_y and C_x. The gray dashed line indicates the C_T level for the disk without wings. The uncertainties in C_T due to the load sensor are below 0.03.

3.4. Concluding Remarks for Preliminary Experimental Tests

The preliminary experiments provided valuable insights into the MRSL model, which significantly informed the final design used in the main context for farm testing. Notably, three-dimensional PTV measurements were also conducted during these tests. While the PTV results offered useful insights that contributed to the decision-making process for the final design, they are not included in this report, as many of the findings can be inferred from the results presented in chapter 5. Additionally, several interesting and potentially important aspects of the MRSL model remain unexplored, such as the aerodynamic interactions between the wings within the MRSL model. These topics are left for future investigations.

3.5. The MRSL

Based on the conducted measurements described in this chapter so far, a final design for the regenerative wind farm experiment is created. This section shows the design of the MRSL for the regenerative wind farm experiment. The experimental models representing multi-rotor systems with lifting devices (MRSL) are illustrated in Figure 3.5. The three configurations, Up-Washing (UW), Without-Lifting (WL), and Down-Washing (DW), are displayed from left to right.

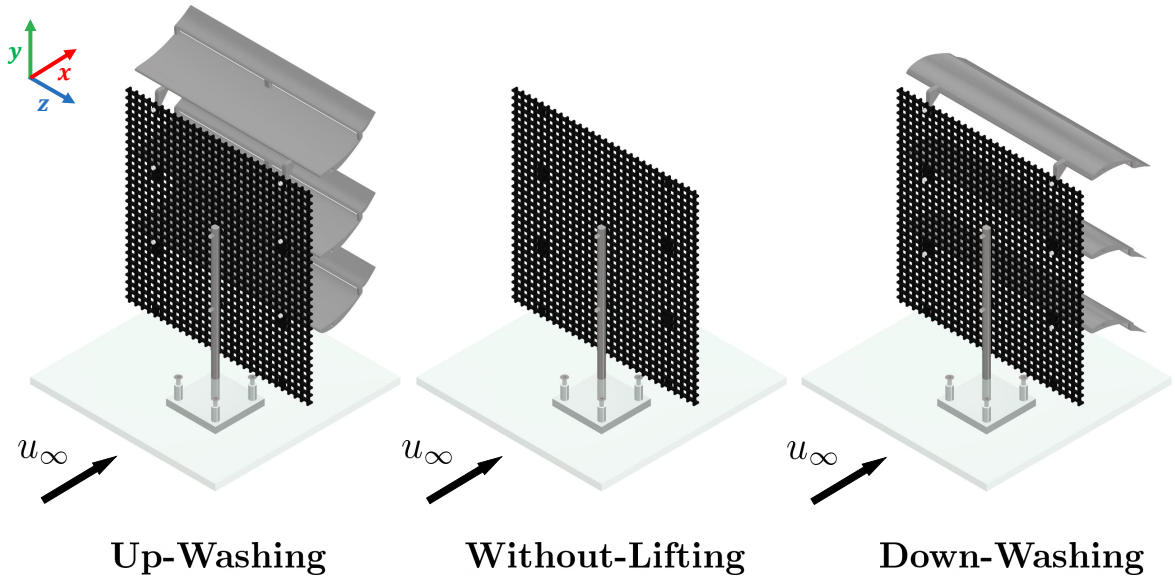

Figure 3.5: A perspective view of the MRSL models used in the experiments. Their configurations are labeled at the bottom. The flow direction is from bottom-left to top-right.

The specifications of the MRSL are presented in Figure 3.6. The rotor parts of MRSL, i.e., the multi-rotor system with several sub-rotors, are simplified as a single square porous disk ($300 \times 300\,\mathrm{mm}^2$). Modeling wake effects of wind turbines using porous disks is a well-established approach in the wind energy community [61]. This method reduces modeling complexity by avoiding the high rotational speeds of small wind turbine models, which can exceed thousands of rpm. Additionally, adjusting the porosity of the disk allows for modeling MRSLs/wind turbines with specific thrust coefficients (C_T). In this study, a porosity of 60% is chosen, which results in a C_T of 0.72 (see section 5.1) and no reverse flow is observed in the wake (see Figure 5.3). The disk's material is acrylic and its pattern is realized through laser cutting. Figure 3.6 provides the specifications of the porous disk, including its critical dimensions and the layout of bolting points for attaching the tower/rod and wings. The porous disk can be deemed to be permeable to flow tracers, as the hole size ($8 \times 8\,\mathrm{mm}^2$) is significantly larger than the tracer diameters ($300{-}400\,\mu$m, see section 4.3).

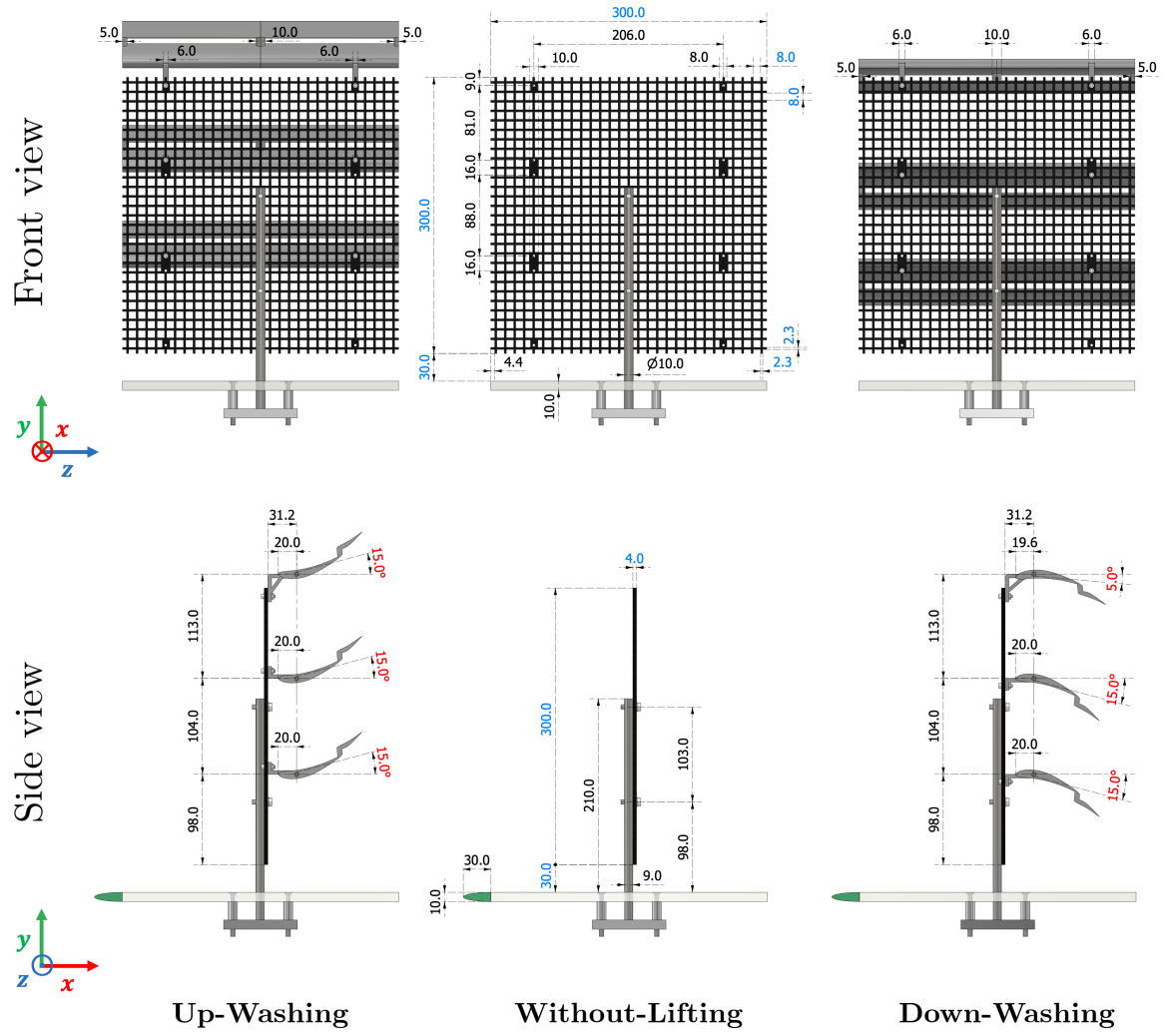

Figure 3.6: The specifications of the MRSL with different configurations are presented. The top and bottom rows show the front and side views of MRSL, respectively. The left, middle, and right columns correspond to the Up-Washing, Without-Lifting, and Down-Washing configurations, respectively. Critical dimensions are marked in blue, while the pitch angles of the MRSL's wings (θ_p) are indicated in red. Additional specifications are labeled in black. In this figure, lengths are given in millimeters (mm), and angles are expressed in degrees (°). The green semi-ellipses in the side view depict the profile of the leading edge installed upstream of the flat plates.

The lifting-devices of the MRSL consist of three wings. A two-element airfoil profile is chosen for the wings due to its relatively higher lift coefficient. A detailed rationale for this selection, along with the XY-plot of the two-element airfoil, is provided in chapter 3. The span of the wings matches the side length of the MRSL (denoted as D), and the chord length is set to $c = D/3$. These wings are fabricated using 3D-printing and are integrated with supporting structures. The supporting structures feature bolting points for mounting the wings onto the porous disk (see Figure 3.6).

The vertical positions of the wings, determined by the positions of the pitching axes (see Figure 3.2), are at $1.05D$, $0.67D$, and $0.33D$ when measured from the bottom of the MRSL. The wings are positioned downstream of the disk, with the streamwise distance between the pitching axes of the wings and the porous disk being $0.10D$ (see Figure 3.6). The clearance between the leading edge of the wings and the disk is $0.04D$ (11 mm). The pitch angles of the wings, θ_p, are indicated in Figure 3.6 and are determined based on preliminary experimental tests documented in chapter 3. The results of preliminary tests demonstrate that the MRSL with these configurations can generate lift that is comparable to its thrust.

The MRSL is held upright with a steel rod with a diameter of 10 mm. The side of the rod in contact with the porous disk is machined flat to ensure a seamless contact between the disk and the rod, providing a sturdier installation for MRSL (porous disk) and the strain gauges (see Section 4.1.2). It is worth noting that machining the rod flat reduces its apparent “diameter” in the side view from 10 mm to 9 mm, as shown in Figure 3.6.

4

Experimental Setup of the Regenerative Wind Farm Experiment

The previous chapter introduced the concept of regenerative wind farming, which leverages vertical forcing and atmospheric boundary layer interactions to enhance total energy output while minimizing the overall land area required. Furthermore, the identified research gap highlights the need for experimental assessment of vertical forcing within a wind farm layout. This chapter outlines the approach used to conduct the wind farm experiment. The first section provides a detailed description of the experimental setup, including the multi-rotor systems with lifting devices (MRSL) and the complete regenerative wind farm configuration within the wind tunnel. The force measurement methodology is also thoroughly discussed. Additionally, this chapter describes the wind tunnel, explains the flow measurement techniques employed, and outlines the post-processing procedures. Finally, it presents the various cases studied and the experimental procedure followed.

4.1. Experimental Setup

The hardware for the regenerative wind farm experiment can be subdivided into two parts. The regenerative wind farm setup and the force measurement setup. The regenerative wind farm setup focuses on the setup required to obtain PTV results, while the force measurement setup aims to acquire load data.

4.1.1. Regenerative Wind Farm Setup

Figure 4.1 presents sketches of the regenerative wind farms (RGWF) tested in the experiments. The floor, representing the sea surface of the regenerative wind farm, is modeled using seven sheets of transparent flat plates (plexiglass), each having a size of 244 cm by 122 cm. Details of their assembly are provided in Figure 4.2. These plates are supported by wooden pieces resting on a metal frame (LINOS X95 System) and are positioned approximately 7 cm above the height where the wind tunnel begins to converge in width (the wind tunnel features an octagonal outlet). The leading edge of the plates is placed about 10 cm from the wind tunnel outlet, and an elliptical profile with an aspect ratio of 3 is added to the leading edge to reduce turbulence generation and prevent flow separation [62]. The profile of the leading edge is illustrated in Figure 3.6, and it is manufactured through 3D printing.

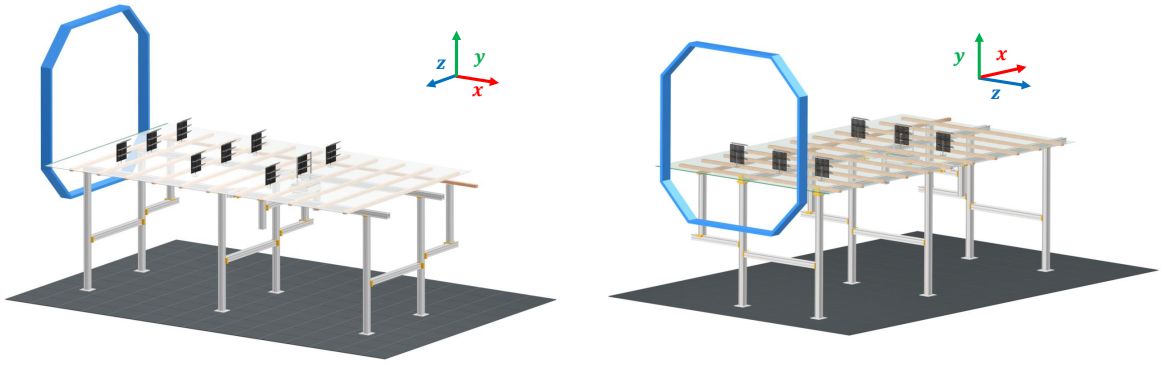

$\Delta_R = 5.0D, \Delta_C = 3.0D$ $\Delta_R = 10.0D, \Delta_C = 3.0D$

Figure 4.1: Illustration of the experimental setups for the regenerative wind farms. The left is a regenerative wind farm with the row-spacing Δ_R being $5.0D$ and having MRSLs in Up-Washing configuration. The right is a regenerative wind farm with the row-spacing Δ_R being $10.0D$ and having MRSLs in Down-Washing configuration. The blue octagonal in both the left and right perspectives represents the wind tunnel outlet. The force measuring devices are installed in the last row of the regenerative wind farm for both left and right.

To fasten MRSLs onto the flat plates, several holes are drilled, and sunken bolts are used, as shown in Figure 3.6. Most of the complex structures supporting the MRSL are positioned beneath the flat plates to minimize flow disturbance. As illustrated in Figure 4.1, the regenerative wind farm layout includes nine loci for MRSL, arranged in three rows and three columns. The row spacing between rows is $5D$ (150 cm), and the lateral spacing between columns is $3D$ (90 cm). The distance from the 1^{st} row of MRSL to the leading edge of the flat plate is $2.6D$ (77 cm). Note that not all cases tested in this study occupy all nine loci (see Section 4.4.1). Additionally, except for case **U-05-MA** in Table 4.1, the MRSLs in different rows are aligned with the inflow velocity (aligned along the x-direction).

In this work, the origin of the regenerative wind farm is defined at the top of the porous disk of the MRSL located in the mid-column of the 1^{st} row (marked as "$\otimes$" in Figure 4.2). The x, y, and z directions correspond to the streamwise, vertical, and lateral directions, respectively.

For a comprehensive understanding of the regenerative wind farm setup, detailed descriptions of the layout of the RGWFs and a photo of the experimental setup are provided. The layout, with labeled dimensions, is shown in Figure 4.2, which illustrates the assembly of the flat plates, their relative distance to the wind tunnel, the locations of the fields of view (FOVs), and other relevant details. The layout of the misaligned case is represented in Figure 4.3. The range of measure region is $8.1 \leq x/D \leq 15.5$ (streamwise), $-2.7 \leq z/D \leq 2.2$ (lateral), and $-1.36 \leq y/D \leq 1.6$. Photos of the experimental setup with critical components labeled are provided in Figure 4.4 and 4.5. Additional photos of the Regenerative Wind Farm experiment are shown in Appendix A.

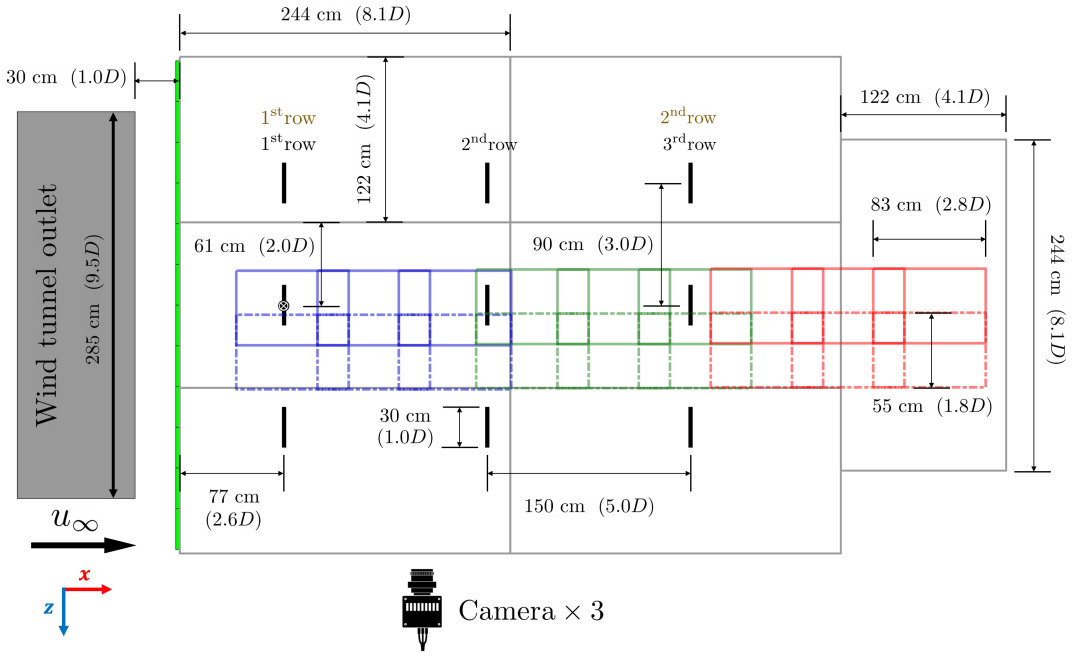

Figure 4.2: The layout of the experimental setups for regenerative wind farms with dimensions labeled. The viewing angle is from above, with flow blown from left to right by the wind tunnel. Seven flat plates (plexiglass) represent the floor (sea surface) and are indicated with gray rectangles, and the loci for MRSLs are marked with thick black lines. The origin of the coordinate system is labeled with "⊗", which is located at the mid-column of the 1st row. Row numbers are shown in black for cases with $\Delta_R = 5D$ and brown for cases with $\Delta_R = 10D$. The field of views (FOVs) of the 3D-PTV system are depicted as blue, green, and red rectangles, corresponding to the three different positions of the traverse system. Green elongated blocks are the elliptical leading edge of the flat plates, and the wind tunnel outlet is represented by a gray block. During the experiment, the cameras shoot from the positive z-direction.

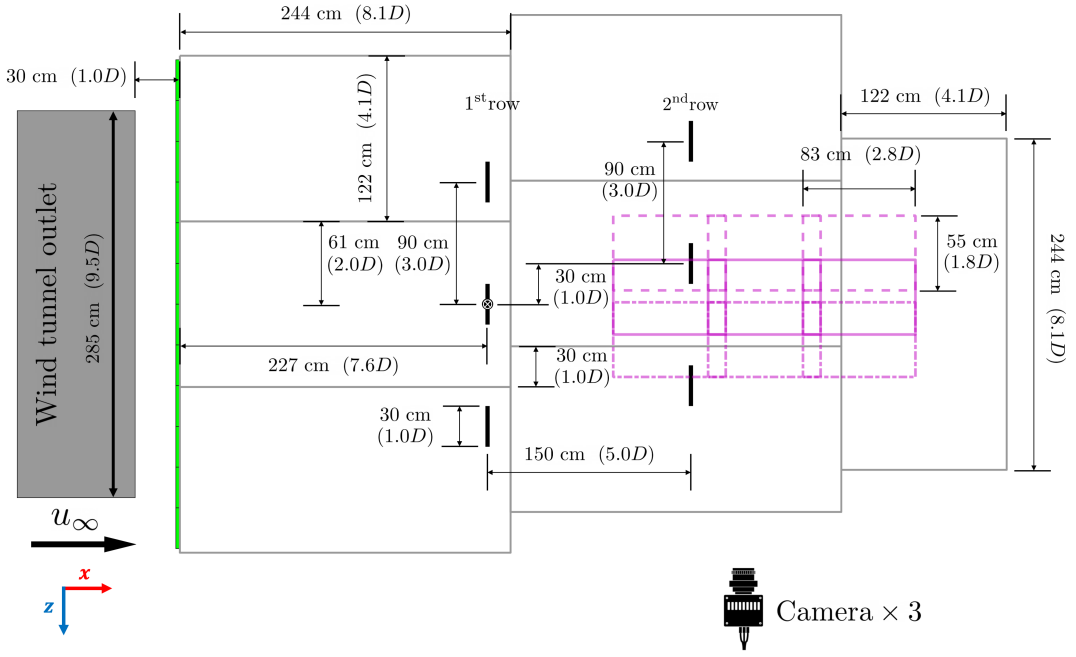

Figure 4.3: The layout of the experimental setups for regenerative wind farms with dimensions labeled for the misaligned case (case **U-05-MA** in Table 4.1). The viewing angle is from above, with flow blown from left to right by the wind tunnel. The origin of the coordinate system is marked with "⊗". Seven flat plates (plexiglass) representing the sea surface are shown as gray rectangles. The loci for MRSL placements are indicated by thick black lines. Magenta rectangles with solid, dashed, and dotted-dashed lines depict the field of views (FOVs) of the 3D-PTV system.

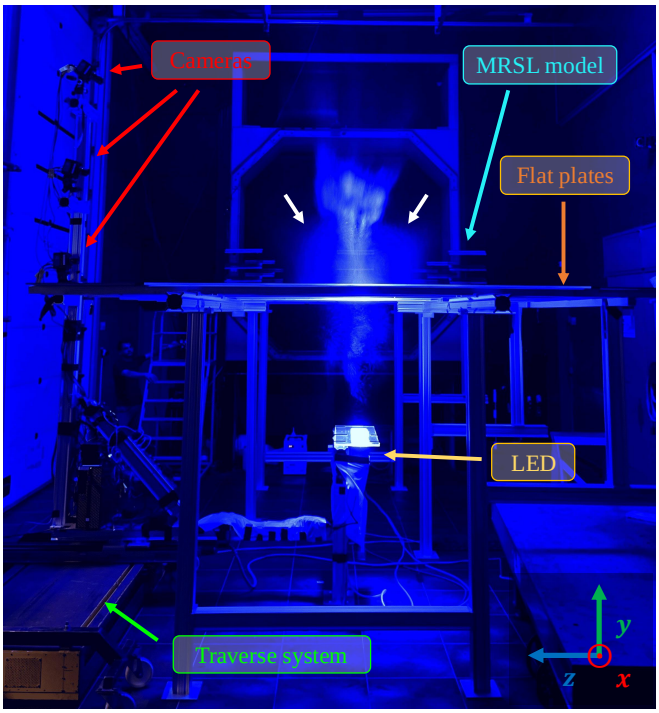

Figure 4.4: Photo of the experimental setup with critical components labeled. The photo is taken during the flow field measurement of case **D-05** in Table 4.1, featuring MRSLs in the Down-Washing configuration. A pair of counter-rotating vortices, which brings the flow downward from above the wake, can be observed and is marked with two white arrows.

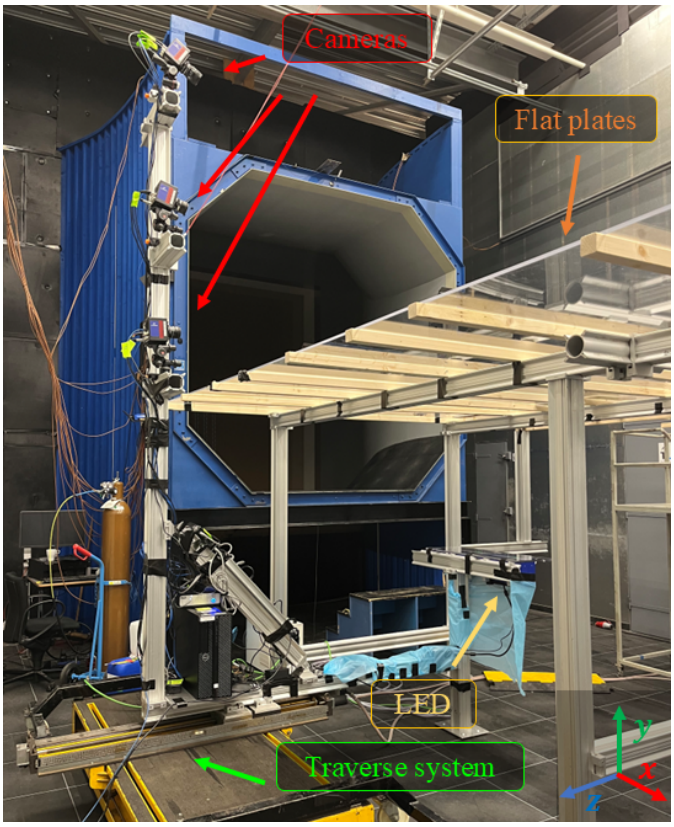

Figure 4.5: Photo of the experimental setup with critical components labeled. The large L-shape beam holds the cameras and the LED unit and is mounted to the traverse system.

4.1.2. Force Measurement Setup

To quantify the forces exerted by MRSLs in a regenerative wind farm, the streamwise (thrust and drag) and vertical (lift) forces of the MRSLs located in the mid-column are measured. The streamwise forces are recorded using two one-component strain gauges, capable of measuring tensile and compressive forces with a precision of 0.1 N (KD24s 10N, ME-Meβsysteme). The vertical forces are measured using a bench scale with a precision of 4×10^{-4} N (FKB 6K0.02, KERN). Unless otherwise specified, the measurement duration for both streamwise and vertical forces is 30 s. The sampling frequencies are $1,000$ Hz for streamwise forces and 1 Hz for vertical forces.

Since the forces of the disk and wings are aerodynamically coupled, measurements are taken both when the wings are attached and when they are detached from the disk, as shown in Figures 4.6. Note that the wing holders which appear in the right of Figure 4.6 do not have contact to the flat plates as additional holes are drilled (these holes are taped when not needed). By subtracting the streamwise forces measured in these two setups, the thrust of the disk and the drag of the wings can be determined separately even though they are coupled. The implementation of force measurement devices in the farm setup is also illustrated in Figure 4.1. However, note that these force measurement devices are dismounted during flow measurements to avoid disturbances to the flow field.

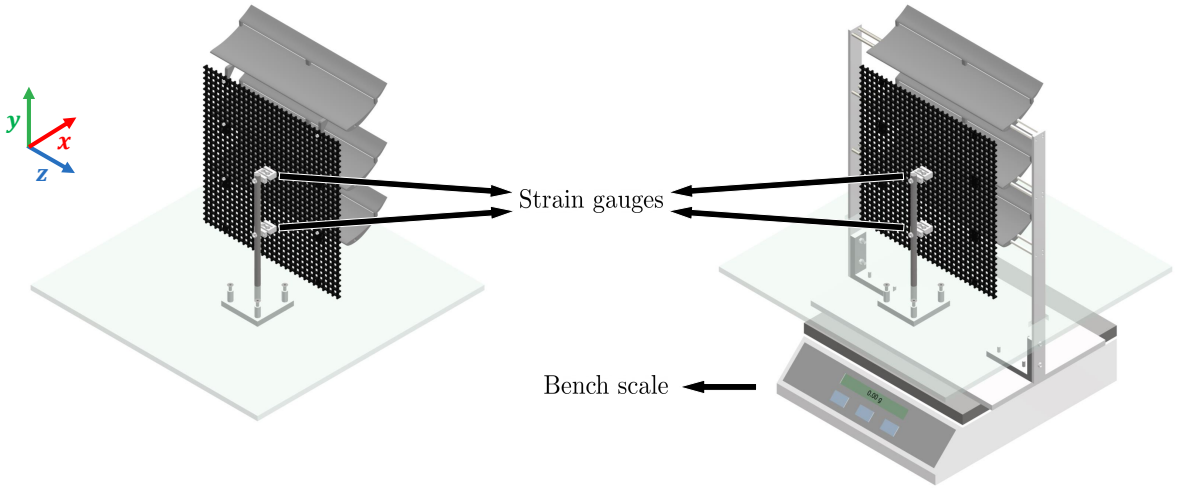

Figure 4.6: The setups for acquiring the forces exerted by MRSL. Left: Measuring the total streamwise force exerted by MRSL (disk's thrust T^R plus wing's drag D^W). Right: Measuring the disk's thrust T^R and the wings' lift L^W simultaneously. Note that the wings' drag D^W is not measured with the setup on the right.

4.2. The Wind Tunnel

The experiment is performed in the atmospheric closed-circuit Open Jet Facility (OJF) wind tunnel at the Aerospace Engineering Laboratories of Delft University of Technology. The OJF has an area contraction ratio of $3:1$ and features an octagonal outlet of 2.85×2.85 m^2. Additional specifications of the OJF are detailed in [16]. An illustration of the entire circuit of the OJF can be seen in Figure 4.7 and originates from [1].

[1] `https://www.tudelft.nl/lr/organisatie/afdelingen/flow-physics-and-technology/facilities/low-speed-wind-tunnels/open-jet-facility`

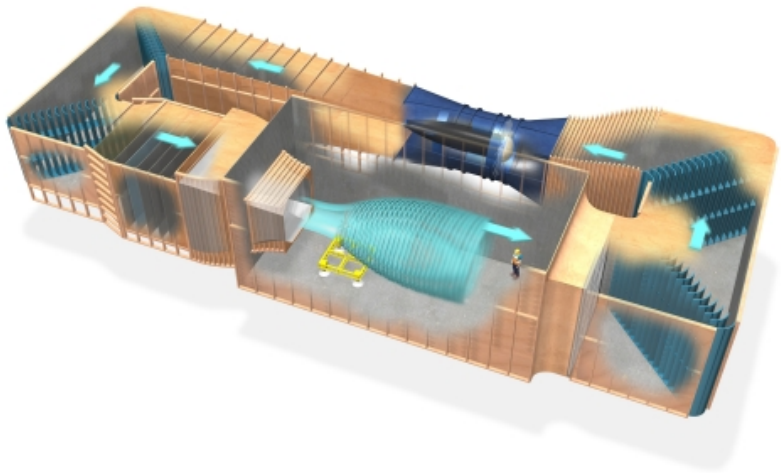

Figure 4.7: Illustration of the OJF which shows the entire closed-circuit open jet configuration. The figure shows the test section, flow direction, fan, and guiding vanes in the corners.

4.3. PTV Equipment and Settings

In this work, a large-scale three-dimensional particle velocimetry (3D-PTV) is employed, where the flow fields are obtained through the measured particle tracks. For each measured volume, $3,000$ images are captured using three high-speed cameras operating at an image rate of $1,000$ Hz. The individual measurement volume is approximately 830 mm, 550 mm, and 880mm, corresponding to $2.8D$, $1.8D$, and $2.9D$ in the streamwise, lateral, and vertical directions, respectively. The PTV system is mounted on a traverse system, enabling it to scan through the regenerative wind farm. After stitching the measured volumes, the total measured domain for the regenerative wind farm spans $-1.2 \leq x/D \leq 14.5$, $-1.4 \leq y/D \leq 1.6$, and $-0.8 \leq z/D \leq 2.1$ in the streamwise, vertical, and lateral directions with respect to the origin. See Figure 4.2 for the FOVs' positions of each measurement.

A detailed description of the setup for the three-dimensional particle tracking velocimetry (3D-PTV) used in this work is provided. The specifications of the software and hardware utilized are outlined in the following.

- **Software and algorithm**
  Commercial software packages, DaVis 11 and DaVis 10 (by LaVision GmbH), are used for image acquisition and processing. The Shake-the-Box (STB) algorithm [54] is employed for detecting the tracks of the tracer particles.
- **Seeding of the tracer particles**
  Neutrally buoyant helium-filled soap bubbles (HFSB) are used as flow tracers, with a median diameter of approximately $300-400$ μm [63, 64]. The HFSB are released from an in-house developed seeding system located in the settling chamber of the wind tunnel (OJF). The seeding system comprises 400 generators, each producing $30,000$ bubbles per second. This system is reported to have a minimal impact on the flow. Particularly, the turbulence intensity is increased by approximately 0.5% to 0.8% [65]. The seeding system measures approximately 1 m in the lateral direction and 2 m in the vertical direction. However, due to the contraction at the wind tunnel exit, the lateral width of the seeded region narrows to about 570 mm as the tracers reach the region of interest. The seeding system can be moved laterally to accommodate different measurement volumes. For more detailed specifications of the seeding system, refer to [66] and [67].

- Illuminating source
  The tracer particles are illuminated using two LED arrays that emit blue light (LED-Flashlight 300 blue, LaVision GmbH). Each array has a dimension approximately 330 mm by 110 mm. During the measurements, the LED arrays are positioned beneath the wind farm by around $1,200$ mm and aligned in the streamwise direction, with their longer sides parallel to the flow. The entire FOV is observed to be adequately illuminated after the light sheet expands (see Figure 4.4).
- Cameras and field of view
  Three high-speed cameras (Photron Mini AX100) are used, each equipped with a CMOS image sensor of 1024 px $\times$ 1024 px and a uniform pixel pitch of 20 μm. As shown in Figure 4.4, the three cameras are mounted on a straight column aligned with the vertical direction (y-direction), with separations of approximately 700 mm. The bottom-most camera is positioned at a height around the center of the MRSL, and the maximum angle of the cameras is about $36°$. The lateral distance (z-direction) between the cameras and the center of the field of view (FOV) is approximately $2,050$ mm. The focal lengths of the objective lenses are 50 mm, 50 mm, and 60 mm for the bottom, middle, and top cameras, respectively. An $f\#$ of 16 is used, providing a depth of focus of around $1,000$ mm. The FOV for this setup measures 830 mm, 550 mm, and 880 mm in the streamwise, lateral, and vertical directions, corresponding to $2.8D$, $1.8D$, and $2.9D$, respectively. Note that the lateral thickness of the FOV is limited by the seeding density of the tracer particles. The center of the FOV is located near the top of the MRSL, and the scaling factor for this setup is approximately 1.43 px/mm.
- Traverse system
  The cameras and the illumination system are mounted on a traverse system (see Figure 4.4), enabling quick shifts of the measurement volume. The traverse system has a range of 1.5 m in the streamwise direction and 1.0 m in the lateral direction, with a precision of 1 mm. The traverse system step size in streamwise and lateral directions ($\Delta_{\text{Tra},x}$ and $\Delta_{\text{Tra},z}$) are set to 600 mm and 375 mm, respectively. During the measurement campaign, the traverse system is manually repositioned to cover the entire region of interest, as described in Section 4.4.2 and illustrated in Figure 4.2. Note that larger overlapping regions are employed when the traverse system is repositioned manually.
- Calibration
  The initial geometric calibration of the cameras is performed by fitting a third-order polynomial to an image of a calibration plate. Subsequently, a volume self-calibration is applied by taking images of the flow field, reducing the root mean square (RMS) of image distortion residuals to 0.1 voxels [68]. The geometric calibration is repeated at the beginning of each day and whenever the traverse system is repositioned manually, while the volume self-calibration is frequently re-applied to maintain the quality of the calibration.

4.4. Conducting the Main Experiment

For executing the main experiment, subsection 4.4.1 highlights the cases that are being performed. subsection 4.4.2 explains the procedure followed during the experimental campagin.

4.4.1. Test Matrix

In this work, RGWFs with three different configurations of MRSL are tested, which are Up-Washing (**UW**), Down-Washing (**DW**), and Without-Lifting (**WL**). To examine how the spacing between rows in the RGWF affects MRSL performance, cases with row-spacings Δ_R being $5D$ and $10D$ are performed (see Figure 4.1). Additionally, to explore the impact of incoming wind direction, an extra case (**U-05-MA**), where the MRSLs in different rows are misaligned, is included. Note that load measurements are not conducted for case **U-05-MA**. Finally, a case without MRSLs (**Clean**) is performed to characterize the conditions of the unperturbed flow for the tested RGWFs. The freestream velocity in the experiments is in the range of $7.1 < u_\infty < 7.3$ m/s.

4.4.2. Procedure of the Experiment

To measure the flow fields, the traverse system is initially positioned upstream, where the FOVs labeled in red in Figure 4.2 can be accessed. After scanning through all the FOVs of this traverse positions, the regenerative wind farm will reconfigured for the next configuration. This procedure allows us to minimize the need for frequent re-calibration of the camera system, which is time-consuming. After running through all the cases/configurations listed in Table 4.1 (except for case **U-05-MA**, which is tested in the last), the traverse system is moved to the next downstream position, and the procedure is repeated. In total, there are three traverse locations, requiring the traverse system to be manually repositioned twice.

For load measurements, the force measuring devices are always positioned at the locus in the mid-column of the last row (see Figure 4.1). The MRSLs in other rows are installed or removed. For example, to measure the forces exerted by the MRSL in the 1^{st} row, the MRSLs in both the 1^{st} and 2^{nd} rows are removed. This approach is considered valid because the flow field does not exhibit significant variation along the streamwise direction until $x/D > 12.0$, as shown in Figure 4.9. Also, as the closest possible Δ_R is $5D$ for our work, it is expected that the downstream MRSLs will not affect the flow fields of upstream MRSLs.

The measurement campaign for the flow fields spans approximately 1.5 weeks, while the load measurements are completed in a single day.

Table 4.1: The tested regenerative wind farms of this work. The first character of the case number indicates the configuration of the MRSL, where **WL**, **U**, and **D** stand for Withouth-Lifting (**WL**), Up-Washing (**UW**), and Down-Washing (**DW**), receptively. The two digits in the middle indicate the row-spacing Δ_R of RGWFs, where **05** and **10** indicate Δ_R being $5D$ and $10D$, respectively. Moreover, suffix **MA** stands for mis-aligned, indicating the MRSLs of the two consecutively row are not aligned with the direction of inflow velocity. Lastly, case **Clean** refers to the test condition where all MRSLs are removed. For all RGWF configurations, the number of columns is fixed at three, and the lateral spacing Δ_C between consecutive columns is $3D$.

Case number	MRSLs' configuration	$\boldsymbol{\Delta_R}$	Number of rows	Load measurement
WL-05	WL	$5D$	three	yes
U-05	UW	$5D$	three	yes
D-05	DW	$5D$	three	yes
WL-10	WL	$10D$	two	yes
U-10	UW	$10D$	two	yes
D-10	DW	$10D$	two	yes
U-05-MA	UW	$5D$	two	no
Clean	-	-	-	-

4.5. From Raw Images to Fields of Flow Quantities

The general procedure for post-processing in this work is outlined as follows. First, subtract-average time-filter (with the window being 11 time steps) is applied to the raw images to mitigate the noise. Then, the particle tracks are detected from the filtered images using the Shake-the-Box (STB) algorithm [54]. Next, the detected tracks are binned onto a Cartesian grid, converting the Lagrangian data into an Eulerian field. Finally, the binned Eulerian fields from each measurement are stitched together to create a complete flow field for each regenerative wind farm configuration. Detailed descriptions of these steps are provided in this subsection.

4.5.1. Particle Tracking

The images are processed using the Shake-the-Box (STB) algorithm [54] to obtain particle tracks. The STB algorithm involves three passes, which are forward in time, backward in time, and reconnection of interrupted tracks. The maximum allowable triangulation error is set to 1.0 voxel. Typically, the number of tracks obtained per time step with this configuration ranges from 4 k to 20 k. These tracks generally cover the measurement volume effectively, except in regions obstructed by the MRSL models. The wide range in track counts primarily arises from the blockage effects caused by the MRSL, including optical obstructions and interference with particle seeding.

4.5.2. Binning

Once the tracks are obtained, they are binned onto a Cartesian grid to compute the spatiotemporal statistics of the flow fields. The binning window is configured as $16 \times 16 \times 16$ voxels ($22.9 \times 22.9 \times 22.9$ mm^3) with 50% overlap, and spatial fitting is performed using a second-order polynomial. Particle tracks shorter than 10 time steps are excluded, and temporal filtering is applied using a second-order polynomial fit with a filtering window of 3 time steps.

In general, the particle count N for each bin exceeds $1,000$. However, in regions near the MRSL model and swirling regions, the particle count can drop to 300 or lower. The 95% confidence interval (uncertainty) of the mean velocity field, denoted as ε_{95}, is defined in Equation 4.1 [69]. For regions not significantly influenced by the MRSL, ε_{95} is typically much smaller than 1%. In contrast, for the waked regions, ε_{95} values are substantially higher due to smaller N. This is especially for the cases where MRSLs are in the configuration **WL** because the replenishment of the tracers is milder due to reduced mixing. Nevertheless, ε_{95} generally remains below 5%.

$$\varepsilon_{95} \triangleq Z_{95} \times \frac{\sqrt{\sigma_u^2 + \sigma_v^2 + \sigma_w^2}}{\sqrt{N}} \times \frac{1}{|\boldsymbol{u}|}, \qquad Z_{95} = 1.96 \tag{4.1}$$

4.5.3. Stitching

Since the domain of interest for the RGWF is significantly larger than the FOV of the 3D-PTV setup, multiple volumes are measured to cover the entire region. After the measurements, the individual volumes are stitched together to reconstruct the complete flow field of the RGWF. The stitching process employs a weighting function, with a hyperbolic tangent function selected for this purpose. Additionally, the variations in wind tunnel speed across different measurements are addressed by scaling the flow quantities during the stitching process. An overview of the stitching process is presented in the diagrams in Figure 4.8, while the algorithm itself is described in detail from Equation 4.2 to 4.6. During the stitching process, volumes are stitched recursively, as illustrated in Figures 4.8(b) and 4.8(c). It is important to note that the algorithm handles only one direction at a time, requiring the stitching sequence to be designed in advance.

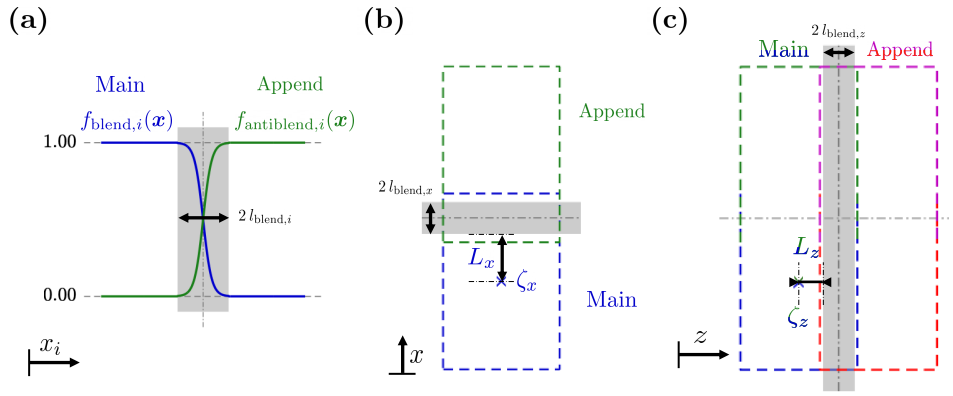

Figure 4.8: Schematic diagrams illustrating the stitching of measured volumes. The dashed lines in different colors represent the fields of views from various measurements. In the diagrams, volume Append is stitched onto volume Main, with the shaded areas indicating the blending/overlapping regions. (a) Blending weights for volume Main and anti-blending weights for volume Append. (b) Stitching volume Append onto volume Main in the x-direction. (c) Stitching another volume Append onto the existing volume in the z-direction. Note that both Main and Append can represent volumes that have already been stitched together with several sub-volumes.

In Figure 4.8 and Equations 4.2 to 4.6, $\boldsymbol{x}$ represents the position vector of the point of interest, while $\boldsymbol{\zeta}$ denotes the position vector of the stitching reference point within volume Main, which is used to determine the blending weightings. Throughout this subsection, the suffix i indicates the stitching direction, which in this work corresponds to x (streamwise direction) or z (lateral direction). The variable δ_i is the distance between $\boldsymbol{x}$ and $\boldsymbol{\zeta}$ in the i-direction.

The blending weightings $f_{\text{blend},i}$ and $f_{\text{antiblend},i}$ are defined in Equation 4.3 and 4.4 which are described using a hyperbolic tangent function within the blending zone. The constant Λ_{blend} controls the rate of change of the blending weights, and in this work, $\Lambda_{\text{blend}} = 3$ is used (note that $\tanh(3) > 0.995$). These blending weightings help avoid potential spurious jumps in flow quantities during stitching.

When stitching two volumes, the blending depth is defined as $2\,l_{\text{blend},i}$. In this work, $l_{\text{blend},x}$ and $l_{\text{blend},z}$ are both set to 75 mm. This choice is based on the traverse system step size ($\Delta_{\text{Tra},x} = 600$ mm and $\Delta_{\text{Tra},z} = 375$ mm) and the field of view dimensions ($\text{FOV}_x = 830$ mm and $\text{FOV}_z = 550$ mm), ensuring that the entire blending zone falls within the overlapping region of the two measurements. Specifically, the condition $\Delta_{\text{Tra},i} + 2\,l\text{blend}, i < \text{FOV}_i$ is satisfied for both the x and z directions. This is visualized in Figures 4.8(b) and 4.8(c).

$$\boldsymbol{\delta}(\boldsymbol{x}) = \boldsymbol{x} - \boldsymbol{\zeta}, \qquad \delta_i = x_i - \zeta_i \tag{4.2}$$

$$f_{\text{blend},i}(\boldsymbol{x}) = \begin{cases} 1.00 & \text{if } \delta_i(\boldsymbol{x}) < \frac{L_i}{2} \\ 0.00 & \text{if } \delta_i(\boldsymbol{x}) > \frac{L_i}{2} + 2\,l_{\text{blend},i} \\ 0.5\left(\tanh\left[\Lambda_{\text{blend}}\left(\frac{L_i/2-\delta_i}{l_{\text{blend},i}} + 1\right)\right] + 1\right) & \text{if } \frac{L_i}{2} \leq \delta_i(\boldsymbol{x}) \leq \frac{L_i}{2} + 2\,l_{\text{blend},i} \end{cases} \tag{4.3}$$

$$f_{\text{antiblend},i}(\boldsymbol{x}) = 1 - f_{\text{blend},i}(\boldsymbol{x}) \tag{4.4}$$

Before initiating the stitching process, the binned data is first interpolated onto a global grid shared by all volumes. The grid size of the global grid is comparable to the binning size. This step significantly facilitates the algorithm since the voxel sizes of different measurements may vary slightly due to re-calibration between some measurements. After projecting the binned data onto the global grid, a layer equivalent to two grid sizes is trimmed from the edges to reduce noise before further processing.

An important consideration in the stitching process is that the volumes being stitched together are obtained from separate measurements. Due to limitations of the wind tunnel, the jet wind speed is not perfectly consistent over the weeks-long experimental campaign, fluctuating between 7.2 and 7.4 m/s. To prevent spurious discontinuities, slight scaling of the flow properties is done during stitching. The scaling factor, denoted as Π, is calculated through Equation 4.5 based on the streamwise velocity u measured in the blending zone overlapped by the two volumes.

To minimize noise when calculating the values of Π, only the upper half of the blending region ($\Theta_y = 60$ mm) is considered, as this region is generally less affected by the MRSL and exhibits lower turbulence. Additionally, a particle count threshold of $\Theta_N = 10$ is applied to ensure that Π is less influenced by noise (data is neglected if $N < \Theta_N$).

$$\Pi = \frac{\sum\limits_{\substack{\boldsymbol{x}\in\text{blending zone} \\ \min\left(N_{\text{Main}}, N_{\text{Append}}\right)\geq\Theta_N \\ y\geq\Theta_z}} u_{\text{Main}} \min\left(N_{\text{Main}}, N_{\text{Append}}\right)}{\sum\limits_{\substack{\boldsymbol{x}\in\text{blending zone} \\ \min\left(N_{\text{Main}}, N_{\text{Append}}\right)\geq\Theta_N \\ y\geq\Theta_z}} u_{\text{Append}} \min\left(N_{\text{Main}}, N_{\text{Append}}\right)} \tag{4.5}$$

Finally, with $f_{\text{blend},i}$, $f_{\text{antiblend},i}$, and Π calculated, the stitching process can be performed. The stitching of a property B is described mathematically in Equation 4.6. Here, n_B represents the exponent of the scaling factor Π, and its value depends on the nature of B. This is necessary because Π is determined based on the streamwise velocity component u, regardless of what B represents. For velocity components (u, v, or w) or vorticity components (ω_x, ω_y, or ω_z), $n_B = 1$. For properties such as turbulent kinetic energy or components of Reynolds stress, $n_B = 2$. Additionally, if B represents particle number (N), $n_B = 0$ is used, as no scaling is required in this case.

$$B_{\text{stitched}}(\boldsymbol{x}) = \begin{cases} B_{\text{Main}} & \text{if } \delta_i(\boldsymbol{x}) < \frac{L_i}{2}, \\ \Pi^{n_B} B_{\text{Append}} & \text{if } \delta_i(\boldsymbol{x}) > \frac{L_i}{2} + 2l_{\text{blend},i}, \\ B_{\text{Main}} & \text{if } \frac{L_i}{2} \leq \delta_i(\boldsymbol{x}) \leq \frac{L_i}{2} + 2l_{\text{blend},i} \\ & \text{and } N_{\text{Main}} \geq \Theta_N \text{ and } N_{\text{Append}} < \Theta_N, \\ \Pi^{n_B} B_{\text{Append}} & \text{if } \frac{L_i}{2} \leq \delta_i(\boldsymbol{x}) \leq \frac{L_i}{2} + 2l_{\text{blend},i} \\ & \text{and } N_{\text{Append}} \geq \Theta_N \text{ and } N_{\text{Main}} < \Theta_N, \\ \frac{B_{\text{Main}} N_{\text{Main}} f_{\text{blend, i}} + \Pi^{n_B} B_{\text{Append}} N_{\text{Append}} f_{\text{antiblend, i}}}{N_{\text{Main}} f_{\text{blend, i}} + N_{\text{Append}} f_{\text{antiblend, i}}} & \text{if } \frac{L_i}{2} \leq \delta_i(\boldsymbol{x}) \leq \frac{L_i}{2} + 2l_{\text{blend},i} \\ & \text{and } N_{\text{Main}} \geq \Theta_N \text{ and } N_{\text{Append}} \geq \Theta_N, \\ \text{NaN (set to 0 if } B \text{ is } N) & \text{else.} \end{cases} \tag{4.6}$$

After recursively stitching the measured volumes, the entire field of interest is obtained as a single entity, resulting in a single stitched volume for each case. However, to facilitate comparisons between cases with different configurations of the regenerative wind farm, a final scaling step is required to account for slight variations in inflow velocity between cases due to the wind tunnel. For this purpose, the property B of the stitched volumes is multiplied by $\Pi_{\text{Global}}^{n_B}$, where Π_{Global} is determined in the inflow zone of the regenerative wind farm, as described in Equation 4.7. The inflow zone is defined within the region $-0.95 \leq x/D \leq -0.60$, $0.53 \leq y/D \leq 0.88$, and $0.84 \leq z/D \leq 1.20$, where the reference inflow velocity is in the range of $7.1 < u_\infty < 7.3$ m/s.

$$\Pi_{\text{Global}} = u_\infty \Bigg/ \left[\left(\sum_{\substack{\boldsymbol{x} \in \text{inflow zone} \\ N_{\text{stitched}} \geq \Theta_N}} u_{\text{stitched}} N_{\text{stitched}} \right) \Bigg/ \left(\sum_{\substack{\boldsymbol{x} \in \text{inflow zone} \\ N_{\text{stitched}} \geq \Theta_N}} N_{\text{stitched}} \right) \right] \tag{4.7}$$

4.6. Inflow Conditions

Before the results are presented and discussed, this section shows the inflow conditions of the regenerative wind farm. The results show the behavior of the floor only. This is the regenerative wind farm setup as shown in Figure 4.1 but without MRSLs installed. Figure 4.9 shows the freestream velocity.

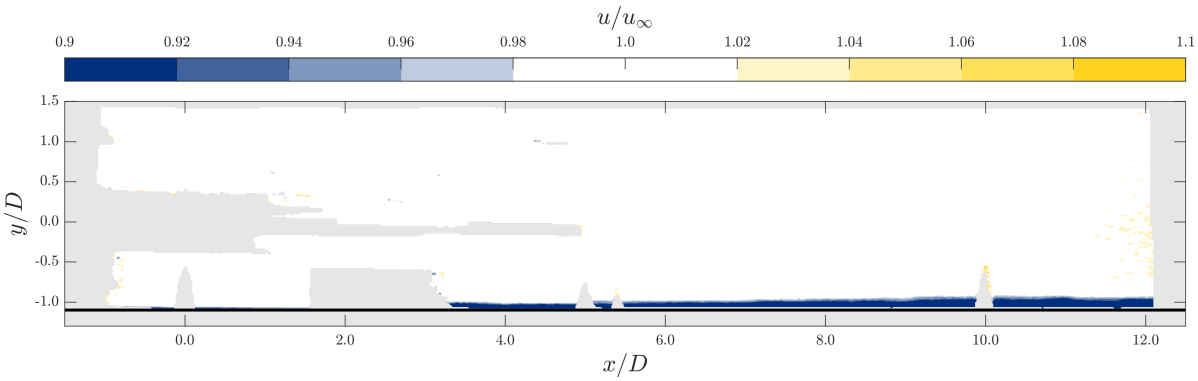

Figure 4.9: Contour plot of the streamwise velocity component, u, normalized by the freestream velocity, u_∞. The black horizontal line indicates the floor of the regenerative wind farm.

The contour plot highlights the accuracy of the freestream velocity. The white region on the color bar corresponds to $0.98 \leq u/u_\infty \leq 1.02$, indicating that the flow field is accurate to within 2%. Additionally, a thin boundary layer develops near the floor. To examine this boundary layer more closely, Figure 4.10 shows the velocity profile of the flow field at $x/D = 8.0$.

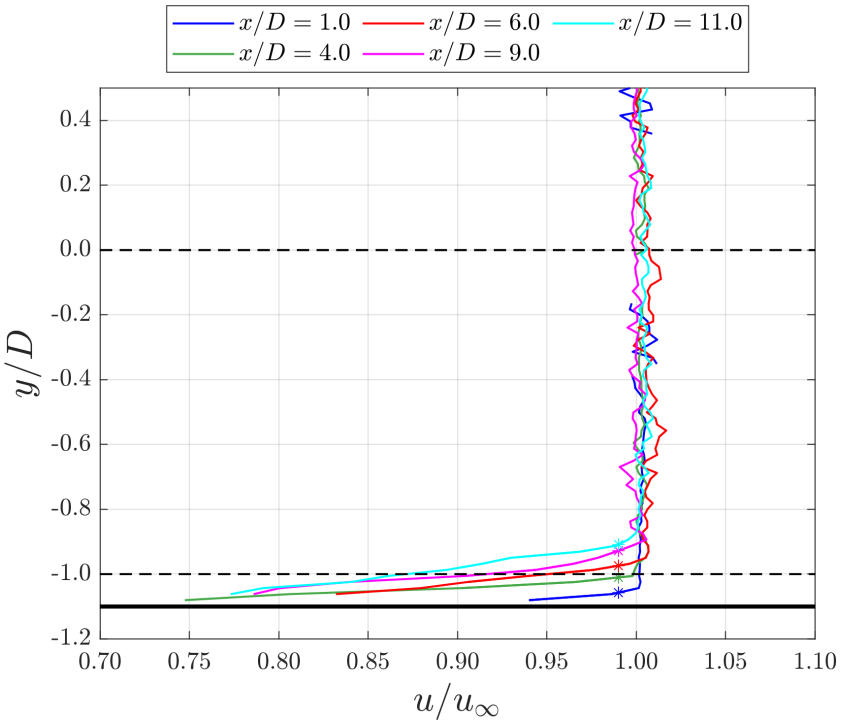

Figure 4.10: The velocity profile of the flow field is represented by the streamwise velocity component, u, normalized by the freestream velocity, u_∞. The velocity profiles for five different x/D values are shown. The black horizontal line denotes the floor, while the dotted lines outline the MRSL projection area of the regenerative wind farm.

This graph indicates that the MRSL projection area is barely affected by the boundary layer development. The bottom of the MRSL projection area still reaches 85% of the freestream velocity at $x/D = 11.0$. Additionally, the boundary layer beneath the MRSL projection area also exhibits relatively high velocities. The thickness of the boundary layer is identified by the stars in the graph. These points mark the δ_{99} in the boundary layer. The boundary layer thickness is quantified in Table 4.2. This quantification shows that the boundary layer never gets close to the bottom wing which is mounted at 123 mm or $y/D = 0.43$ from the floor. As a reference, a velocity profile that does contain an ABL can be seen in Figure 2.5 at $x/D = -1$.

Table 4.2: The boundary layer thickness δ_{99} is shown in terms of non-dimensional y/D value and thickness in milimeters. The x/D positions correspond with the velocity profiles shown in Figure 4.10. The distance between the floor and the bottom of the MRSL is y/D = 0.1 which is 30 mm.

Position	δ_{99} [-]	δ_{99} [mm]
x/D = 1.0	y/D = 0.04	13
x/D = 4.0	y/D = 0.09	27
x/D = 6.0	y/D = 0.13	38
x/D = 9.0	y/D = 0.17	52
x/D = 11.0	y/D = 0.19	57

5

Results and Discussion of the Regenerative Wind Farm Experiment

With the methodology for the regenerative wind farm experiment established, the results can now be analyzed. This chapter presents the findings of the primary experiment, referred to as the regenerative wind farm experiment. The first section focuses on the forces exerted by the MRSLs, examining both the 5D and 10D cases. The following two sections present the PTV results for the 5D and 10D cases, respectively, detailing the velocity components U and V and the vorticity. Finally, the available power is analyzed and discussed.

5.1. Forces Exerted by MRSLs

This subsection presents the forces exerted by MRSLs, with the results demonstrating that the implementation of lifting devices significantly increases the measured thrust of downstream MRSLs by several factors. The methodology for measuring these forces is detailed in Section 4.1.2, and the measurements are only on the MRSLs in the mid-column. In this work, T^R, L^W, and D^W represent the thrust (streamwise force) exerted by the MRSL (porous disk), the lift (vertical force) exerted by the wings, and the drag (streamwise force) exerted by the wings, respectively. For consistency, the positive directions of T^R, L^W, and D^W are defined as negative x, positive y, and negative x, respectively.

The normalized forces, denoted as $\widehat{T}^R$, $\widehat{L}^W$, and $\widehat{D}^W$, are defined in Equation 5.1, where the hat operator $\widehat{(\cdot)}$ indicates the normalization. The normalization is achieved by dividing the forces by T^R measured at the mid-column of the 1^{st} row in case **WL-05**, denoted as $T^R\Big|_{1^{\text{st}}}^{\text{WL-05}}$. Unless otherwise specified, $T^R\Big|_{1^{\text{st}}}^{\text{WL-05}}$ in this study is 2.07 N, corresponding to a thrust coefficient C_T of 0.72. The definition of C_T used in this work is provided in Equation5.2 with $u_\infty = 7.3$ m/s.

$$\widehat{T}^R \triangleq \frac{T^R}{T^R\Big|_{1^{\text{st}}}^{\text{WL-05}}}, \qquad \widehat{L}^W \triangleq \frac{L^W}{T^R\Big|_{1^{\text{st}}}^{\text{WL-05}}}, \qquad \widehat{D}^W \triangleq \frac{D^W}{T^R\Big|_{1^{\text{st}}}^{\text{WL-05}}} \tag{5.1}$$

$$C_T \triangleq \frac{T^R}{0.5\rho u_\infty^2 D^2} \tag{5.2}$$

For both the 5D and 10D row spacing cases, the dependency on the Reynolds number is investigated. This is done to ensure that the experimental results are not significantly influenced by variations in the Reynolds number. The results for different inflow wind speeds are provided in Appendix B.

5.1.1. Cases with 5D Row Spacing

The results of $\widehat{T}^R$, $\widehat{L}^W$, and $\widehat{D}^W$ for cases with a row-spacing Δ_R being $5D$ are presented in Figure 5.1.

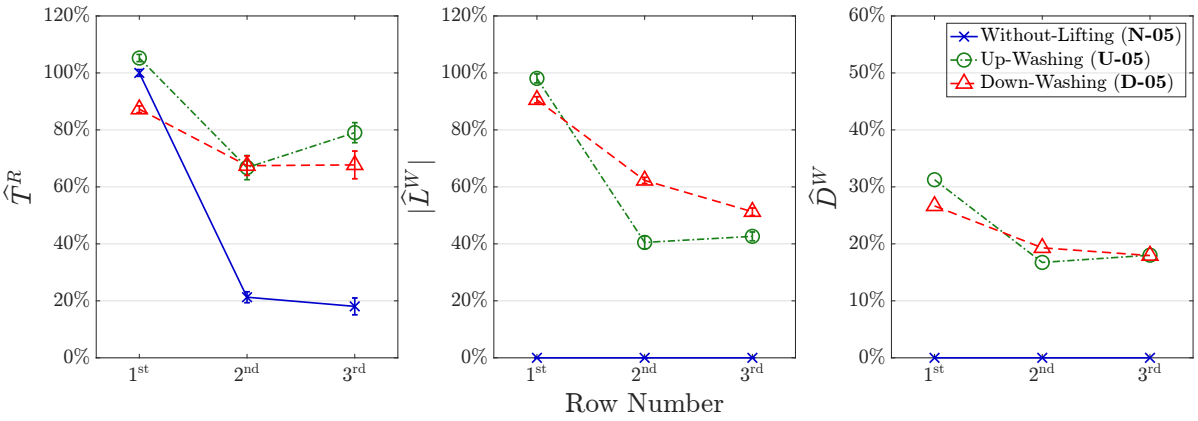

Figure 5.1: Normalized (time-averaged) rotor's thrust ($\widehat{T}^R$), wings' lift ($\widehat{L}^W$), and wings' drag ($\widehat{D}^W$) for cases with row-spacing being $5D$. The measured standard deviations for $\widehat{T}^R$ and $\widehat{L}^W$ are labeled with the error bars. The case numbers corresponding to Table 4.1 are indicated in the legends.

The measured T^R for cases with lifting devices significantly outperforms those without (case **WL-05**). Specifically, despite the additional $\widehat{D}^W$, the measured T^R after the 2^{nd} row is tripled in cases **U-05** and **D-05** compared to case **WL-05**. This result is even more pronounced than what [60] found numerically using a CFD approach with steady RANS, where T^R after the 2^{nd} row in a regenerative wind farm was approximately doubled by equipping MRSLs with lifting devices. It is important to note, however, that the experiments in this study are conducted under near-laminar inflow conditions, whereas the simulations in [60] use an inflow turbulence intensity of 8%.

According to the classic actuator disk theory [70], tripling T^R implies that the power harvested by the MRSLs (P^R) after the 2^{nd} row in cases with lifting devices is more than five times greater than in cases without lifting devices, as $P^R \propto \left(T^R\right)^{3/2}$. This remarkable increase highlights the potential of regenerative wind farms to achieve significantly higher power output per unit surface area compared to the traditional wind farms.

In addition to the transformative advancements in increasing T^R and P^R, several aerodynamic features of the MRSLs and regenerative wind farms are worth noting. As shown in Figure 5.1, the ratios between L^W and T^R are approximately one in the 1^{st} row for cases **U-05** and **D-05**, indicating that the MRSLs perform as designed. However, this ratio gradually decreases in the 2^{nd} and 3^{rd} rows. This reduction can be attributed to the vertical flow induced by the upstream MRSLs, which alters the inflow conditions for the downstream MRSLs. The induced vertical flow significantly affects the angle of attack (α) seen by the MRSLs' wings, as the pitch angle (θ_p) of the wings is kept constant regardless of their position in the regenerative wind farm (see Section 3.5). This observation suggests that for more consistent performance, either the MRSL wings should be able to adjust θ_p or they should be designed to be less sensitive to variations in α. Additionally, in case **U-05**, T^R, $|L^W|$, and D^W in the 3^{rd} row are higher than those in the 2^{nd} row, indicating that the wake recovery effects of MRSLs accumulate as they progress deeper into the regenerative wind farm. This trend is also observed in the simulations by [60]. Lastly, the error bars in Figure 5.1 reveal that the fluctuations (standard deviations) in T^R increase in the later rows, reflecting the impact of turbulence generated by the upstream MRSLs.

5.1.2. Cases with 10D Row Spacing

To investigate whether the effects of lifting-devices are still significant in regenerative wind farms with larger row-spacing, cases with $\Delta_R = 10D$ are tested, namely cases **WL-10**, **U-10**, and **D-10** in Table 4.1. The results of the forces exerted in these cases are presented in Figure 5.2.

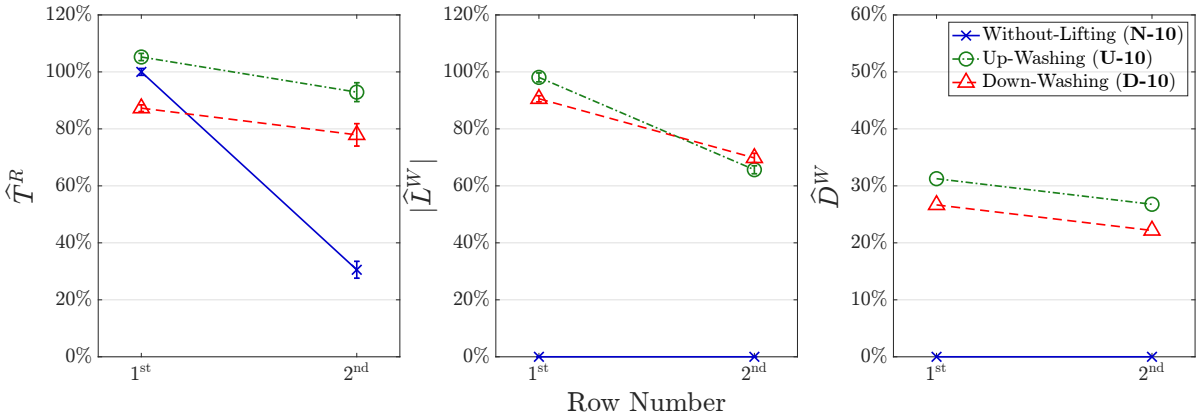

Figure 5.2: Normalized (time-averaged) rotor's thrust ($\widehat{T}^R$), wings' lift ($\widehat{L}^W$), and wings' drag ($\widehat{D}^W$) for cases with row-spacing being $10D$. The measured standard deviations for $\widehat{T}^R$ and $\widehat{L}^W$ are labeled with the error bars. The case numbers corresponding to Table 4.1 are indicated in the legends.

It is evident that the cases with lifting-devices (**U-10** and **D-10**) still significantly outperform the case without lifting devices (**WL-10**). Moreover, when comparing the MRSLs in the 2^{nd} row of cases with $\Delta_R = 10D$ to those with $\Delta_R = 5D$, the 2^{nd}-row MRSLs in the cases with $\Delta_R = 10$ exert stronger forces (T^R, L^W, and D^W) across all three configurations. This result indicates that the wakes recover more effectively with increased row spacing, as expected [5].

5.2. PTV Results for 5D row spacing

This section explores the PTV results from the regenerative wind farm experiment for the 5D inter-turbine spacing cases. First, cross-sectional views of the streamwise velocity are presented. Then, the same cross-sections are used to examine the vertical velocity component. Lastly, various cross-sections of the vorticity field are analyzed.

5.2.1. Streamwise Velocity

The results for the streamwise velocity component, u, are presented in Figure 5.3. The figure illustrates four cross-sectional planes for the Up-Washing, Without-Lifting, and Down-Washing configurations. The first cross-section depicts the inflow conditions one MRSL width upstream of the first MRSL. The cross-section at $x/D = 4.0$ represents the far wake of the first MRSL, located four MRSL widths downstream. The remaining two cross-sections correspond to the far wake of the second and third MRSLs, each situated four MRSL widths downstream.

Starting with the inflow conditions for all cases, the results are very similar. For all configurations, slightly higher velocities are evident in the upper part of the measurement volume. In the Up-Washing case, elevated velocities are also observed on the right side of the MRSL projection area. To account for differences in inflow conditions, a large volume of data points is averaged to find an accurate reference velocity.

Examining the wake of the Without-Lifting case, a velocity deficit is observed directly behind the MRSL projection area. At $x/D = 4.0$, the wake exhibits minimal expansion in both the horizontal and vertical directions. In this region, the freestream velocity remains largely undisturbed, except near the floor, where lower velocities are detected. This behavior aligns with expectations, as the floor induces a boundary layer. The wake downstream of the second MRSL at $x/D = 9.0$ features a region of significantly lower velocities. Besides this, the wake region expands in both horizontal and vertical directions, which happens because of turbulent mixing. The wake behind the third turbine exhibits higher velocities compared to the second turbine but remains lower than those observed behind the first. In this cross-section, more turbulent mixing in the wake ensures more expansion in both directions.

It is important to note that the velocity fields at the cross-sections $x/D = 4.0$ and $x/D = 9.0$ are located just before the second and third MRSLs, respectively. Consequently, these figures illustrate the flow energy available for the MRSLs located in the second and third rows. Regions with a more pronounced blue color indicate lower energy availability for harvesting. Therefore, the Up-Washing and Down-Washing configurations aim to transport the turbine wakes out of the MRSL projection area. This should result in more red areas in the MRSL projection area indicated by the black dashed squares.

To determine whether the Up-Washing case achieves its intended objective, the wake of the first MRSL at $x/D = 4.0$ is examined. The velocity deficit induced by the actuator surface is shifted upward due to the vertical velocity generated by the lifting devices. Moreover, the shape of the velocity deficit transforms from the square-like profile observed in the Without-Lifting case. The vortices induced by the lifting devices flatten and widen the deficit area. Within the MRSL projection area, large regions of high velocity (dark red) are visible, entrained by the induced rotations. These in-plane velocity components are depicted by the arrows. Observing the far wake behind the second turbine at $x/D = 9.0$, the flow deficit area nearly doubles in size. While the MRSL projection area displays slightly more yellow and orange regions, the majority of the flow deficit expands in the positive y-direction. Examining the core of the flow deficit (indicated by the green color), its vertical position is significantly higher compared to the wake behind the first turbine. From the arrows in the figure, it can be inferred that the upwash strength reduces but extends over a larger vertical region. Evaluating the wake behind the third MRSL, the deficit area becomes even larger, with its shape transitioning toward a circular profile. The height of the flow deficit core is slightly reduced, but less green is observed overall. Comparing the Up-Washing cross-sections to the Without-Lifting case, the MRSL projection areas exhibit significantly higher streamwise velocity values. Additionally, the Up-Washing case shows considerably less dark blue, indicating that low-energy flow regions are not only redirected but also diminished.

Examining the Down-Washing case at $x/D = 4.0$, the flow deficit region is split into two parts due to the downward flow toward the floor combined with the introduced tip vortices. The arrows near the floor indicate significant outboard velocities. High streamwise velocity values are observed at the top of the MRSL projection area. Furthermore, this cross-section lacks the green regions present in the Without-Lifting and Up-Washing cases for the same location. At the next cross-section $x/D = 9.0$, the core of the flow deficit shifts further outboard, and the overall deficit region increases in size. Two flow deficit regions are still present in this cross-section, although only part of the left region is in the measurement domain. The streamwise velocity values within the deficit region are comparable to those observed in the Up-Washing case. In the final cross-section at $x/D = 14.0$, the flow deficit region has expanded further in size but no longer exhibits any green regions. Additionally, the deficit region has shifted slightly more outboard. Compared to the Up-Washing case, larger in-plane velocity values are observed, and the flow deficit region shows higher streamwise velocity values.

When comparing the Down-Washing cross-sections to the Without-Lifting case, a conclusion similar to that of the Up-Washing case can be drawn: the MRSL projection areas exhibit significantly higher streamwise velocity values. Additionally, the Down-Washing case displays much less dark blue, indicating that low-energy flow regions are not only redirected but also diminished. Focusing on the key difference between the Up-Washing and Down-Washing cases, the Up-Washing case entrains high streamwise velocity from the sides, whereas the Down-Washing case entrains it directly from above.

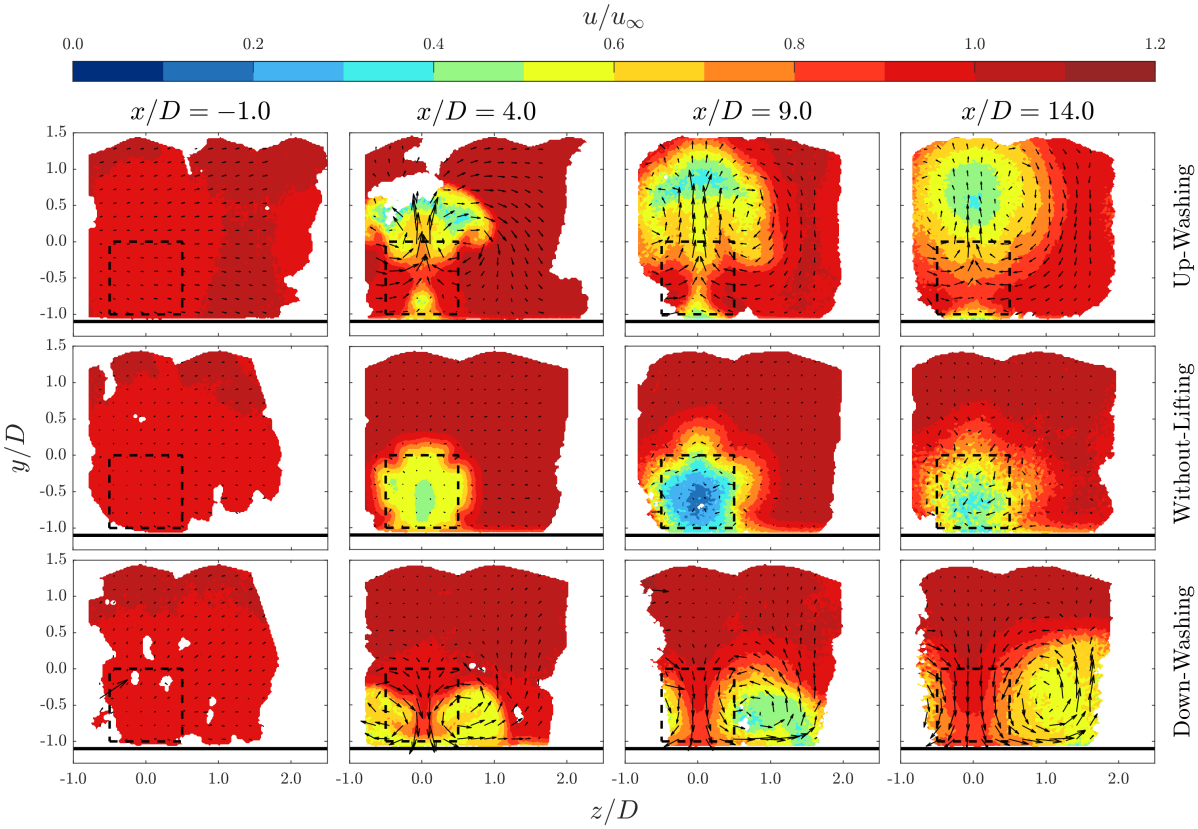

Figure 5.3: The mean streamwise velocity component, u, normalized by the freestream velocity, u_∞, is shown for cases with 5D inter-turbine spacing. The first row corresponds to the (**U-05**) case, representing Up-Washing. The second row shows the (**WL-05**) case, representing Without-Lifting, while the third row illustrates the (**D-05**) case, representing Down-Washing. The MRSL projection area is indicated by black dashed lines, and the floor is marked by solid black lines. Arrows depict the in-plane velocity. The columns represent cross-sections orthogonal to the freestream direction. As an example, $x/D = -1.0$ is a cross-section positioned one MRSL width in front of the first MRSL.

The streamwise velocity component, normalized by the freestream velocity, for the Up-Washing, Without-Lifting, and Down-Washing cases is presented again in Figure 5.4. However, this time the figure depicts a side cross-section at the center of the middle MRSLs, corresponding to $z/D = 0.0$. The turbine configurations at $x/D = 0, 5$, and 10 are also included in the plot.

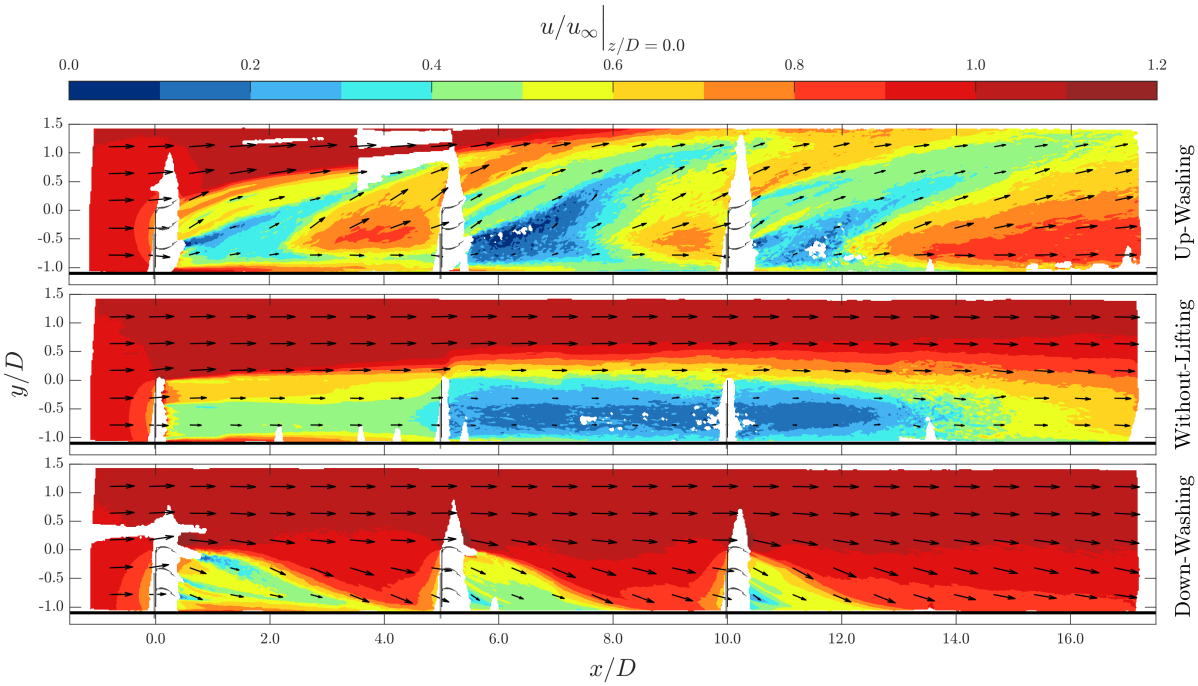

Figure 5.4: The mean streamwise velocity component, u, normalized by the freestream velocity, u_∞, evaluated at $z/D = 0.0$ which is the MRSL center, is shown for cases with 5D inter-turbine spacing. The top plot corresponds to the (**U-05**) case, representing Up-Washing. The middle plot depicts the (**WL-05**) case, representing Without-Lifting, while the bottom plot illustrates the (**D-05**) case, representing Down-Washing. The corresponding MRSL configurations show this too. Arrows represent the in-plane velocity.The floor of the regenerative wind farm is indicated by the black horizontal line in all plots.

Focusing on the Without-Lifting case, it is evident that the wake of the first MRSL shows minimal signs of recovery. The interaction with the high-velocity regions above the wind farm is negligible, as indicated by the sharp shear layer. This sharp profile persists throughout the entire wake, from $x/D = 0.0$ to $x/D = 5.0$. The sharpness of the shear layer is attributed to low turbulent mixing, which is already discussed in subsection 2.1.2. Referring back to Equation 2.7, it is evident that wake recovery resulting from turbine forces is driven by turbulence and vertical advection. In the absence of significant vertical advection, limited turbulent mixing becomes the primary factor responsible for the lack of wake recovery. The wake of the second MRSL exhibits a large blue region, indicating low streamwise velocity values. Behind the second MRSL, the wake shows some vertical expansion, accompanied by a less sharp shear layer compared to the wake of the first MRSL. However, the blue region persists up to the third MRSL. In the wake of the third MRSL, the same blue region is observed, but after four MRSL widths downstream, the wake begins to recover. This recovery is associated with the least sharp velocity profile in this wind farm configuration.

The Up-Washing case is analyzed to assess the impact of introducing vertical advection by configuring the actuator surface with lifting devices. The use of lifting devices leads to significant differences in the wind farm's wake. A substantial interaction with the high-velocity region above the wind farm is observed. The wake of the MRSL reaches heights of 1.5 times the MRSL width, starting from the top of the MRSL. This represents a marked difference compared to the y/D expansion of 0.5 in the Without-Lifting case. Furthermore, pockets of high streamwise velocity are observed before the second and third MRSLs. These regions represent high-momentum flow entrained from the sides, as shown in Figure 5.3. This explains why these MRSLs experience significantly higher thrust values, as seen in Figure 5.1. The lifting devices induce substantial deflections in the wake and facilitate energy replenishment into the wind farm layer. This process can be viewed as an exchange of low-momentum flow from the wind farm layer with high-momentum flow from the layer above the wind farm.

Similar phenomena can be seen in the Down-Washing case. However, in this configuration, the low momentum flow is directed down and outboard of the MRSL which ensures that high momentum flow entrains from the top. The wake of the top airfoil in the first MRSL is pronounced, while the wakes of the second and third MRSL are significantly diminished. This corresponds to a reduction in the length of the wake region. Consequently, it can be concluded that the angle of attack of the top wings varies, as the inflow conditions differ for the second and third MRSL and the wings start performing better as noticed by the reduced wake region. It should be noted that although very large red areas are seen in this case, the cross-section only shows the middle of the actuator surface. To further investigate the development of the wake inside the wind farm, multiple cross-sections are shown. Figure 5.5 shows the cross-section at the edge of the MRSLs.

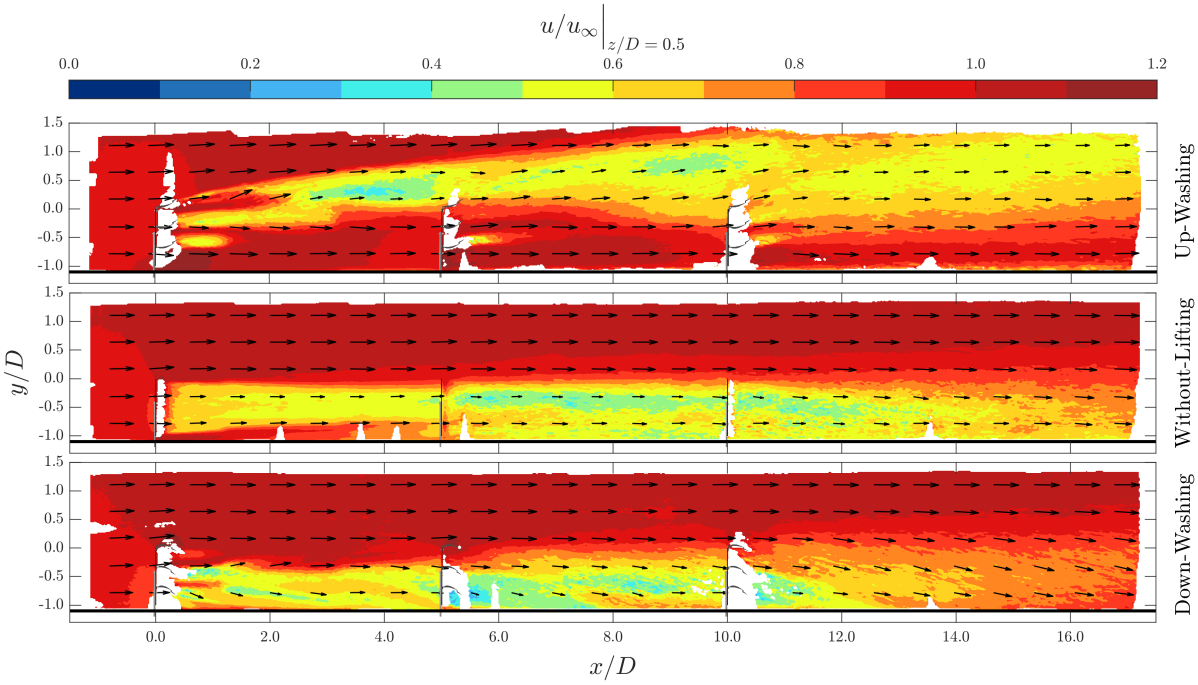

Figure 5.5: The mean streamwise velocity component, u, normalized by the freestream velocity, u_∞, evaluated at $z/D = 0.5$ which is the MRSL edge, is shown for cases with 5D inter-turbine spacing. The top plot corresponds to the (**U-05**) case, representing Up-Washing. The middle plot depicts the (**WL-05**) case, representing Without-Lifting, while the bottom plot illustrates the (**D-05**) case, representing Down-Washing. The corresponding MRSL configurations show this too. Arrows represent the in-plane velocity. The floor of the regenerative wind farm is indicated by the black horizontal line in all plots.

In this cross-section, the Without-Lifting case exhibits similar wake characteristics to the previous cross-section, albeit with fewer regions of low-velocity values. As shown earlier in Figure 5.3, the dark blue velocity deficit is confined in the MRSL projection area.

For the Up-Washing case in this cross-section, high-momentum flow is observed in the lower layers of the wind farm. Notably, higher velocity values are seen at the sides of the MRSL projection area, as confirmed by Figure 5.3. This behavior is not observed in the Down-Washing configuration, which exhibits similarities to the Without-Lifting case. However, for the Down-Washing case, high-momentum flow is directed toward the center of the MRSL projection area, as illustrated in Figure 5.4.

To gain a deeper understanding of wind farm wake behavior between rows, Figure 5.6 presents the normalized streamwise velocity at a z/D value of 1.0.

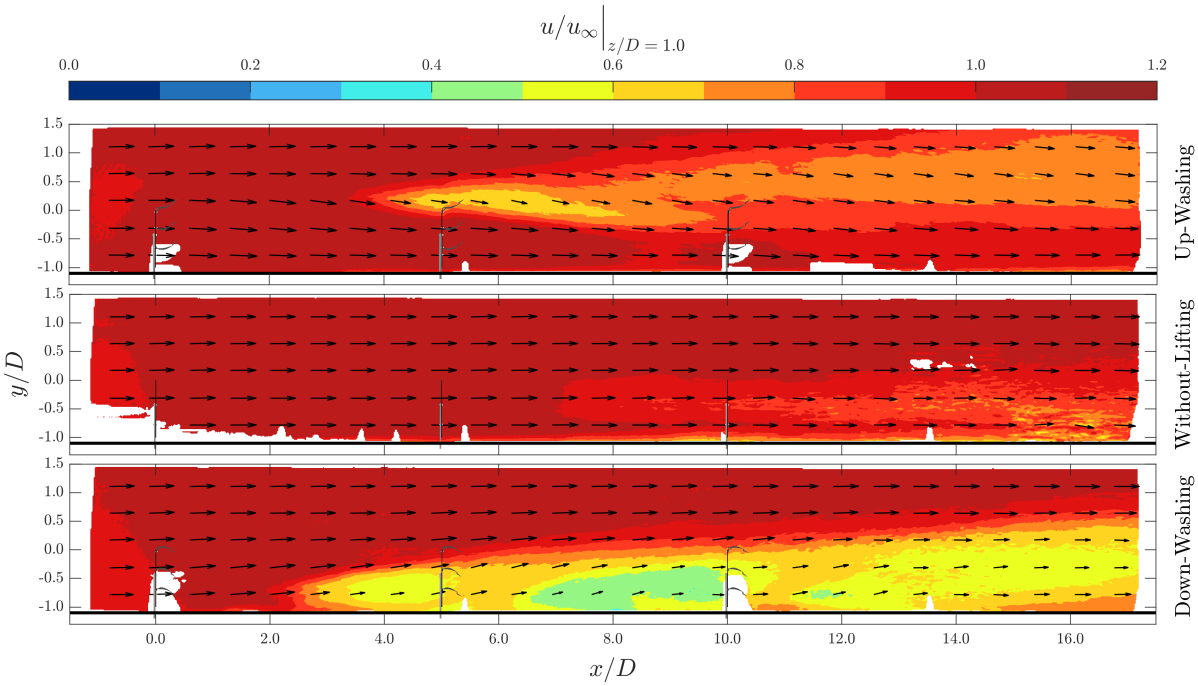

Figure 5.6: The mean streamwise velocity component, u, normalized by the freestream velocity, u_∞, evaluated at $z/D = 1.0$, is shown for cases with 5D inter-turbine spacing. The top plot corresponds to the (**U-05**) case, representing Up-Washing. The middle plot depicts the (**WL-05**) case, representing Without-Lifting, while the bottom plot illustrates the (**D-05**) case, representing Down-Washing. The corresponding MRSL configurations show this too. Arrows represent the in-plane velocity. The floor of the regenerative wind farm is indicated by the black horizontal line in all plots.

The Without-Lifting case shows minimal wake deficit in this cross-section. This indicates that the low-velocity values really remain close to the turbine array, ultimately reducing thrust forces. The Up-Washing case shows a bit more of the wake deficit, although it is still minimal since the wake is pushed up instead of to the sides. It can be noted that at this cross-section, a down-wash in the upper layers in the flow field is seen by the arrows. This shows that high-momentum flow is transported into the wind farm. For the Down-Washing case, a significant wake region can be identified. As already stated, this configuration splits the wake and pushes it out of the MRSL projection area instead of up. Therefore, the wake remains in between rows in the wind farm layer.

So far, the streamwise velocity of the regenerative wind farm has been reviewed. The next section discusses the vertical velocity component to gain a more comprehensive understanding of the magnitude of the up and down-washing cases.

5.2.2. Vertical Velocity

The vertical velocity component for the regenerative wind farm is illustrated in Figure 5.7, using the same cross-sections as in Figure 5.3. This component is normalized by the freestream velocity. The maximum values reach half of the streamwise velocity component in the vertical direction, which determines the range of the color bar.

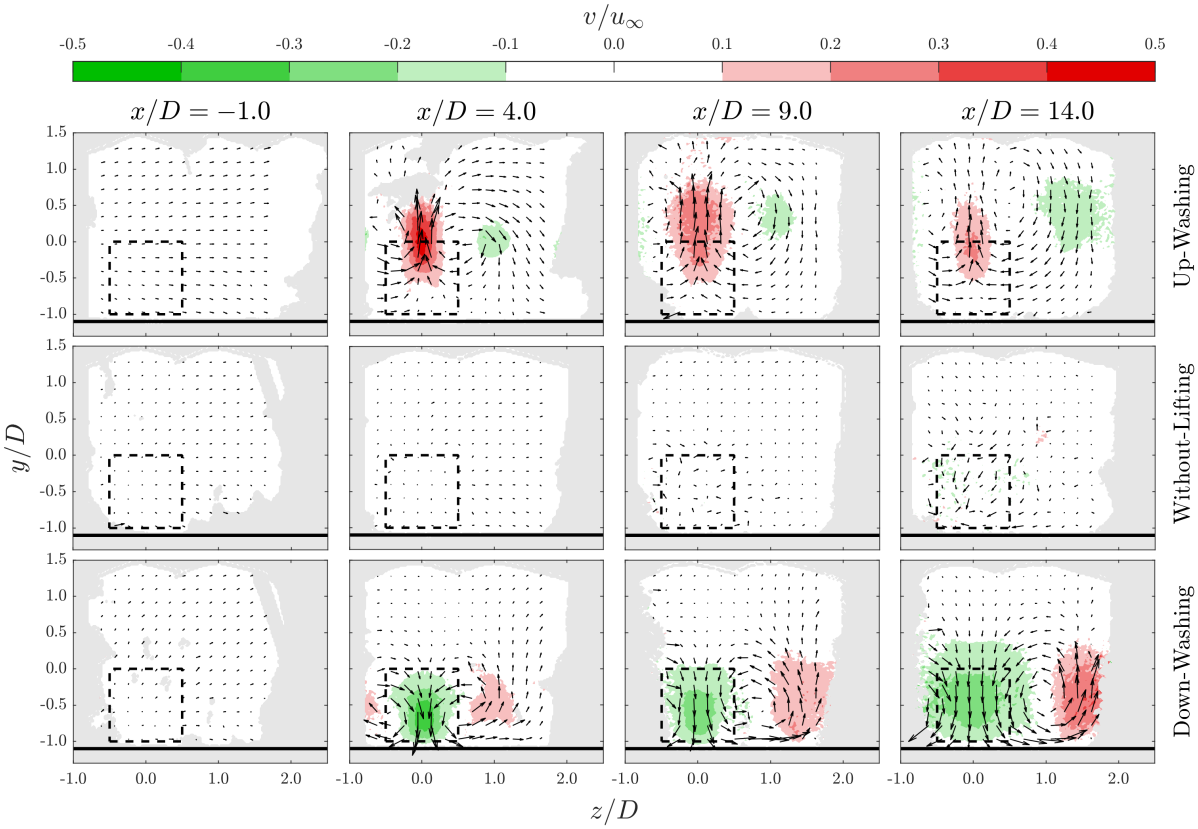

Figure 5.7: The mean vertical velocity component, v, normalized by the freestream velocity, u_∞, is shown for cases with 5D inter-turbine spacing. The first row corresponds to the (**U-05**) case, representing Up-Washing. The second row shows the (**WL-05**) case, representing Without-Lifting, while the third row illustrates the (**D-05**) case, representing Down-Washing. Black dashed lines indicate the MRSL projection area and solid black lines mark the floor. Arrows depict the in-plane velocity.

For the inflow conditions, no vertical velocity is observed in the flow across all three cases. In the Without-Lifting case, no vertical velocity is present in the wakes of the first and second MRSL. However, in the wake of the third MRSL at $x/D = 14.0$, light red and green spots appear in the cross-section. These spots in the Without-Lifting case result from turbulence, which increases progressively after each MRSL.

In the Up-Washing case, the wake of the first turbine exhibits significant upwash, with the center reaching values in the range of $v/u_\infty = 0.4$ to 0.5. Due to the rotation induced by the wings, the outer regions of the MRSL projection area experience a downwashing effect. The magnitude of this downwash is reduced to $v/u_\infty = 0.1$ to -0.2, as it is distributed over a larger area, which can be seen by the arrows. The wake of the second MRSL shows vertical velocity values that are spread over a larger area in both vertical and horizontal directions. This stretching reduces the velocity values. A slightly larger green spot is observed in this cross-section compared to the first wake, and its position is shifted upward in the positive vertical direction. This shift occurs due to the expanded upwash region. In the wake of the third MRSL, the upwash is significantly weakened in both intensity and area. This reduction is primarily caused by unfavorable inflow conditions for the lifting devices. As seen in Figure 5.1, the lift forces for the second and third MRSLs are considerably reduced. This reduction arises from two factors: first, the increased turbulence di-

minishes the wings' effectiveness, and second, the altered angle of attack caused by the upwash from the preceding MRSL. The upwash reduces the angle of attack, leading to a corresponding decrease in lift force. For all three wake cross-sections, the green area increases, indicating a strengthening of the downwash within the wind farm. This increased downwash enhances energy entrainment from higher layers above the wind farm. Additionally, the center of circulation rises progressively in height, which positively impacts the entrainment of high-momentum flow from higher altitudes above the wind farm.

The Down-Washing configuration shows a strength similar to that of the Up-Washing case in the wake of the first MRSL. However, the upwash region adjacent to the MRSL projection area is larger compared to the Up-Washing case. This enlargement is attributed to the proximity of the ground, which amplifies the rotational strength. In the wakes of the second and third MRSLs, a progressive increase in upwash is observed, resembling the increase in downwash (green area) seen in the Up-Washing case. Notably, the upwash in the wake of the third MRSL is more pronounced than the downwash observed in the Up-Washing case. This difference arises from the combined effects of the floor's proximity and the significantly larger downwash region in the wake of the third MRSL. The extensive green area in the wake of the third MRSL indicates that more lift is generated by the second and third MRSLs compared to the Up-Washing case, as evidenced in Figure 5.1.

The vertical velocity component is presented again, but for a different cross-section. Figure 5.8 illustrates the flow field from the side of the regenerative wind farm at the center of the middle MRSLs.

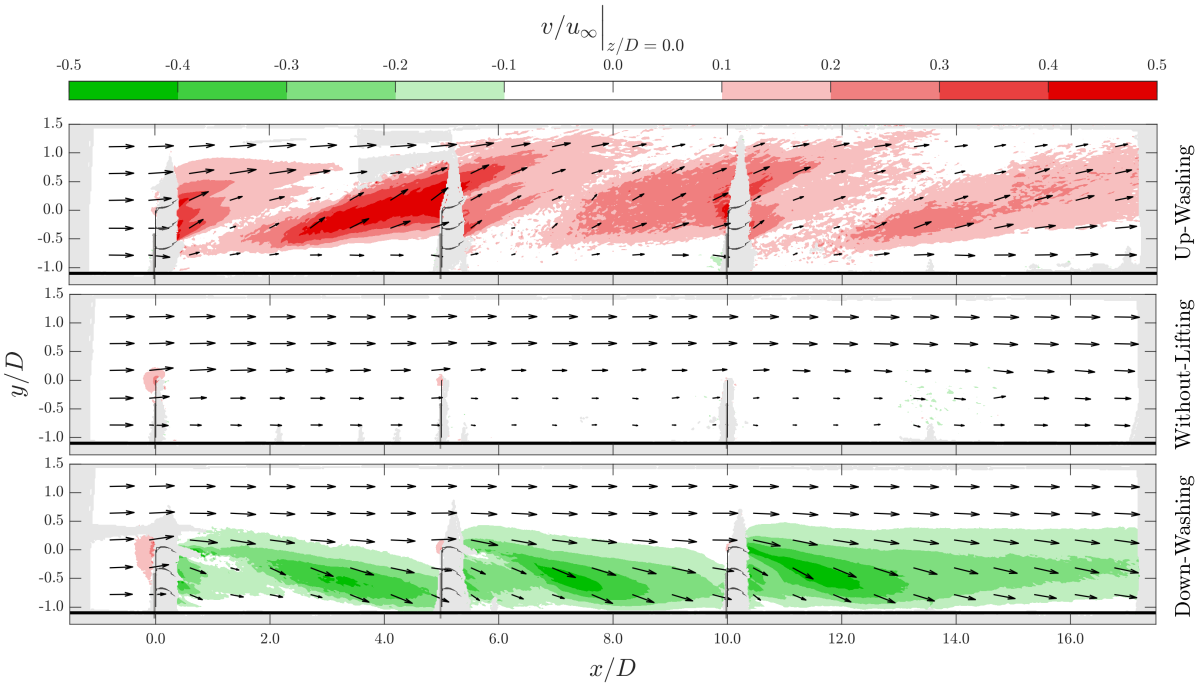

Figure 5.8: The mean vertical velocity component, v, normalized by the freestream velocity, u_∞, evaluated at $z/D = 0.0$, is shown for cases with 5D inter-turbine spacing. The top plot corresponds to the (**U-05**) case, representing Up-Washing. The middle plot depicts the (**WL-05**) case, representing Without-Lifting, while the bottom plot illustrates the (**D-05**) case, representing Down-Washing. The corresponding MRSL configurations show this too. Arrows represent the in-plane velocity. The floor of the regenerative wind farm is indicated by the black horizontal line in all plots.

Starting with the Without-Lifting case, no vertical velocity is observed except near the top of MRSL one and two. This upwash at the edge of the MRSL is explained by momentum theory, which states that stream tubes expand across an actuator surface due to the flow deficit caused by the actuator thrust. The reduced significance of this effect in MRSL two and its absence in MRSL three can be attributed to the less sharp shear layer, as noted in Figure 5.4. This less sharp

shear layer leads to less pronounced vertical velocities, which in this case remain at $v/u_\infty < 0.1$.

In the Up-Washing case, a vertical velocity region is observed directly behind the rotor. This region arises from the upwash generated by the three wings. The top of this region diminishes due to the high-momentum flow passing over the MRSL. Following this initial upwash region, a diagonal zone with minimal vertical velocity is visible behind all MRSLs. A second vertical velocity region, present behind all three MRSLs, is caused by the rotation induced by the wings. This rotational flow entrains high-velocity air into the wind farm, creating a second upwash. This phenomenon is already evident in Figure 5.7. The rotation originating from the wings will be examined in detail in subsection 5.2.3. Furthermore, the strength of the vertical velocity reduces progressively for each MRSL wake.

In the Down-Washing case, the wakes of the first and second MRSLs exhibit a similar phenomenon to that observed in the Up-Washing case. An initial downwash generated by the wings is followed by a stronger downwash caused by the induced rotation of the wings. In the wake of the third MRSL, the distinction between the first and second downwash regions becomes less apparent, merging into a single downwash region. Additionally, the downwash region in the far wake of the third MRSL remains significant, extending more than seven MRSL widths downstream. To investigate the direction of vertical flow in between turbine rows, Figure 5.9 shows the vertical velocity component at a cross-section of $z/D = 1.0$.

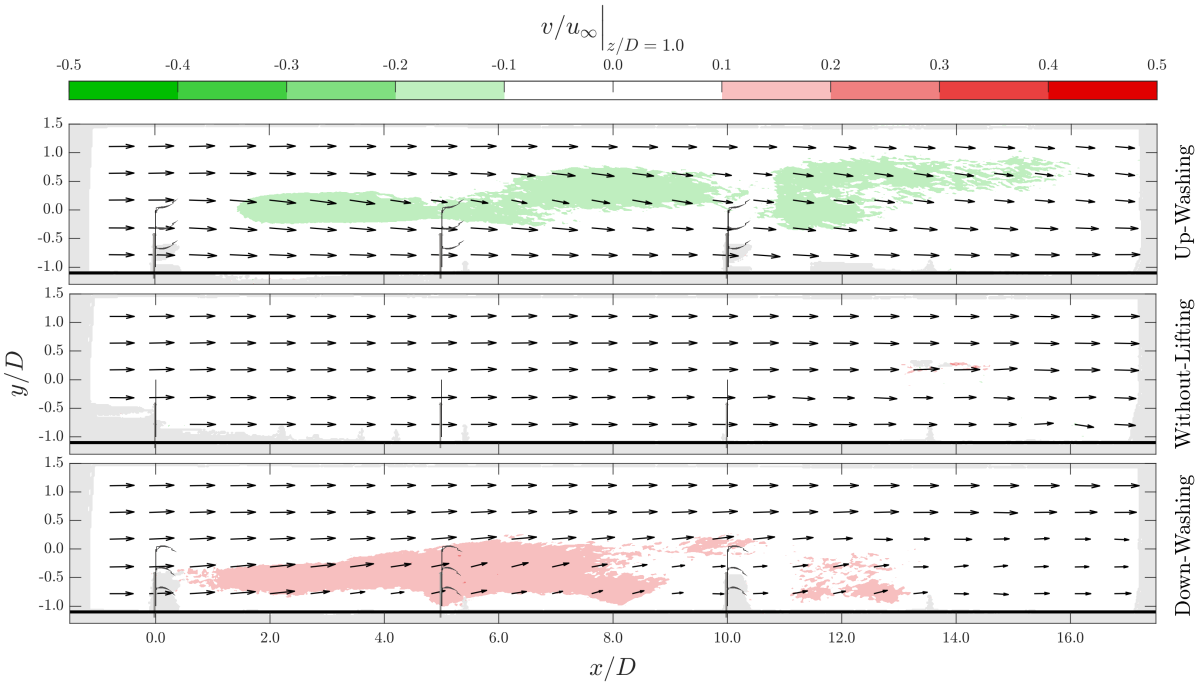

Figure 5.9: The mean vertical velocity component, v, normalized by the freestream velocity, u_∞, evaluated at $z/D = 1.0$, is shown for cases with 5D inter-turbine spacing. The top plot corresponds to the (**U-05**) case, representing Up-Washing. The middle plot depicts the (**WL-05**) case, representing Without-Lifting, while the bottom plot illustrates the (**D-05**) case, representing Down-Washing. The corresponding MRSL configurations show this too. Arrows represent the in-plane velocity. The floor of the regenerative wind farm is indicated by the black horizontal line in all plots.

In the Without-Lifting case, no vertical velocity is observed. Since this cross-section represents the flow field between turbine rows, the vertical velocity at the MRSLs is not visible. However, the figure shows a mild downwash region for the Up-Washing case and an upwash region for the Down-Washing case. This cross-section thus highlights the induced circulation created by the lifting devices. Although the vertical velocity appears to decrease in the wake of MRSL three for both cases, it is important to note that the upwash and downwash shift laterally to higher z/D values. This behavior is also evident in Figure 5.7, particularly in the cross-section at $x/D = 14.0$. The vertical velocity regions are concentrated closer to $z/D = 1.5$.

5.2.3. Streamwise Vorticity

The previously discussed rotation in the flow field originates from the vortex cores generated by the wings. This section investigates this phenomenon in detail. Additionally, interaction between vortex cores is expected, as six vortex cores are produced per MRSL. Since this interaction begins in the near wake, the development of the flow in both the near wake and far wake is analyzed. For an examination of this phenomenon in the wake of the first MRSL, refer to Figure 5.10.

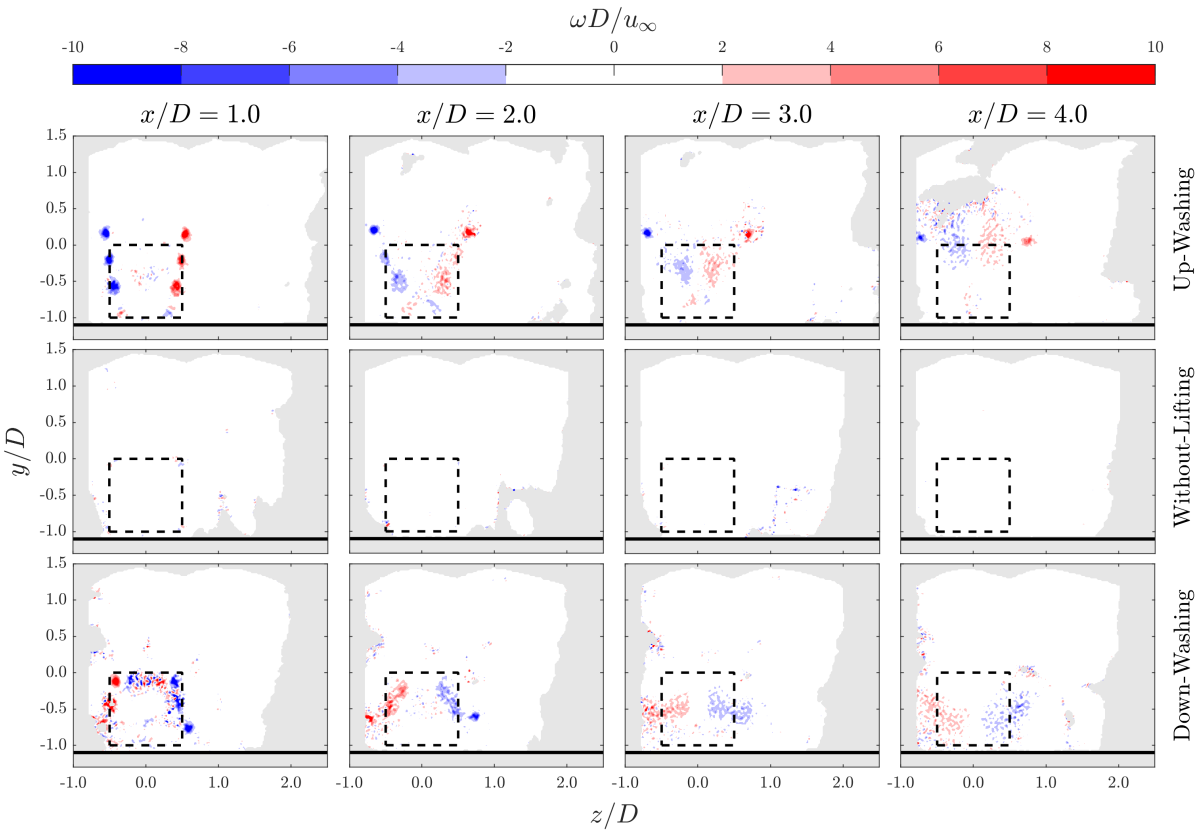

Figure 5.10: The streamwise vorticity, ω, normalized by multiplying with the rotor width D and dividing by the freestream velocity, u_∞, is shown for cases with 5D inter-turbine spacing. The first row corresponds to the (**U-05**) case, representing Up-Washing. The second row shows the (**WL-05**) case, representing Without-Lifting, while the third row illustrates the (**D-05**) case, representing Down-Washing. Black dashed lines indicate the MRSL projection area and solid black lines mark the floor.

In the without-lifting case, no significant vorticity is observed in the wake of the first MRSL. This result is expected, as no circulation is induced in the absence of lifting devices. In the Up-Washing case, three lifting devices generate three bound vortices along the wingspan. At the wing tips, the bound vortex produces two trailing vortices in the streamwise direction for each wing. In the cross-section at $x/D = 1.0$, the trailing vortex cores from each wing are visible. Notably, the wings create an upwash, resulting in a clockwise rotation of the vortex cores on the right and a counterclockwise rotation of those on the left. In the second cross-section, interaction begins between the bottom two vortex cores. Additionally, the vortex cores from the top wing remain stronger, which is attributed to the top wing operating in clean air, unobstructed by the actuator surface, and thus performing more efficiently. Moreover, the vortex pairs from the bottom two wings begin to rotate around the core of the top vortices, indicating an inboard rotation of vorticity. This effect becomes even more pronounced at $x/D = 3.0$. At $x/D = 4.0$, the vortex pair from the top wing can still be identified, although it is weakening. In contrast, the vortex pairs from the other two wings are no longer visible, as their cores have diffused.

In the Down-Washing case, six vortex cores can again be identified at $x/D = 1.0$. However, they are less pronounced compared to the Up-Washing case. In addition to the six vortex cores at the

edges of the MRSL projection area, there is a region of increased vorticity near the top of the MRSL projection area. This heightened turbulence arises from the wake of the top airfoil. Examining the cross-section at $x/D = 2.0$, the bottom vortex pair is observed to remain in place, while the top two vortex pairs begin to rotate around it. This phenomenon can be attributed to the presence of the floor combined with the downwash from the wings. As previously discussed in Figure 5.3 and Figure 5.7, the circulation center shifts outboard and upward, originating from the bottom vortex pair, as indicated by the arrow directions. At $x/D = 3.0$, no vortex cores can be identified. This contrasts with the Up-Washing case, where one vortex pair remains identifiable at $x/D = 4.0$. The difference occurs because the top wing does not correspond to the main center of circulation, causing the strongest vortex pair from the top wing to diffuse more rapidly in the Down-Washing case.

The vortex structures of the consecutive turbines diffuse more rapidly due to the turbulence introduced by the first MRSL. This phenomenon is illustrated in Figure 5.11. For the same reason, only two MRSL widths are shown downstream, as the diffusion of the vortex cores no longer provides relevant information.

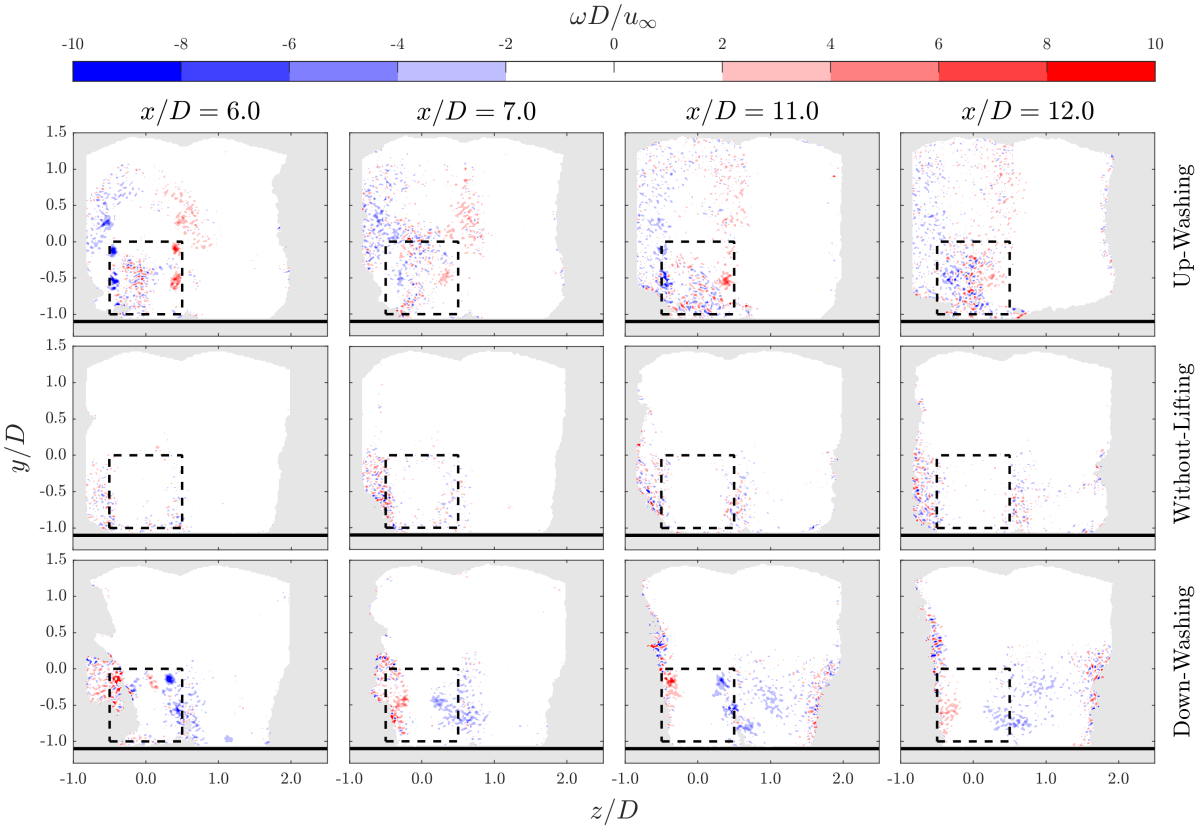

Figure 5.11: The streamwise vorticity, ω, normalized by multiplying with the rotor width D and dividing by the freestream velocity, u_∞, is shown for cases with 5D inter-turbine spacing. The first row corresponds to the (**U-05**) case, representing Up-Washing. The second row shows the (**WL-05**) case, representing Without-Lifting, while the third row illustrates the (**D-05**) case, representing Down-Washing. Black dashed lines indicate the MRSL projection area and solid black lines mark the floor.

As expected in the Without-Lifting case, no vortex cores are observed in the wakes of the second and third MRSL. However, increased turbulence is evident along the sides of the MRSL projection area. This turbulence arises from turbulent mixing, which is the primary mechanism for wake recovery in a conventional wind farm.

In the Up-Washing case, six recognizable vortex cores are still visible at one MRSL width downstream. Among these, the top vortex pair exhibits the least strength. By $x/D = 7.0$, all vortex

cores have diffused. At $x/D = 11.0$, in the wake of the third MRSL, only the bottom vortex pair remains identifiable. The bottom half of the MRSL projection area exhibits a mixed region of higher vorticity values. One additional MRSL width downstream, nearly the entire MRSL projection area transitions into a mixed region of elevated vorticity without recognizable cores. Across all four cross-sections, low vorticity values are observed above the MRSL projection area, corresponding to the wake deficit region.

In the Down-Washing case, the top vortex pair remains identifiable at $x/D = 6.0$. By $x/D = 7.0$, only two regions with low vorticity values persist. In the wake of the third MRSL, only the top vortex pair is visible, though it is weaker compared to the wake of the second MRSL. Finally, at $x/D = 12.0$, the vorticity field becomes diffused, with minor vorticity values present along the sides of the MRSL projection area, marking the region of the wake deficit as seen in Figure 5.3.

5.2.4. Turbulence Intensity

To quantify the level of turbulence in the flow, this section presents the Turbulence Intensity (TI) for the same cross-sections as those used for streamwise and vertical velocity. TI is calculated as the Root Mean Square (RMS) of the fluctuating velocity component divided by the freestream velocity. High TI indicates greater unsteadiness and larger velocity fluctuations within the flow, enhancing mixing by promoting energy and momentum exchange between fluid layers. In contrast, low TI signifies a smoother, more stable flow with minimal fluctuations. Figure 5.12 illustrates the turbulence intensity along the streamwise cross-sections.

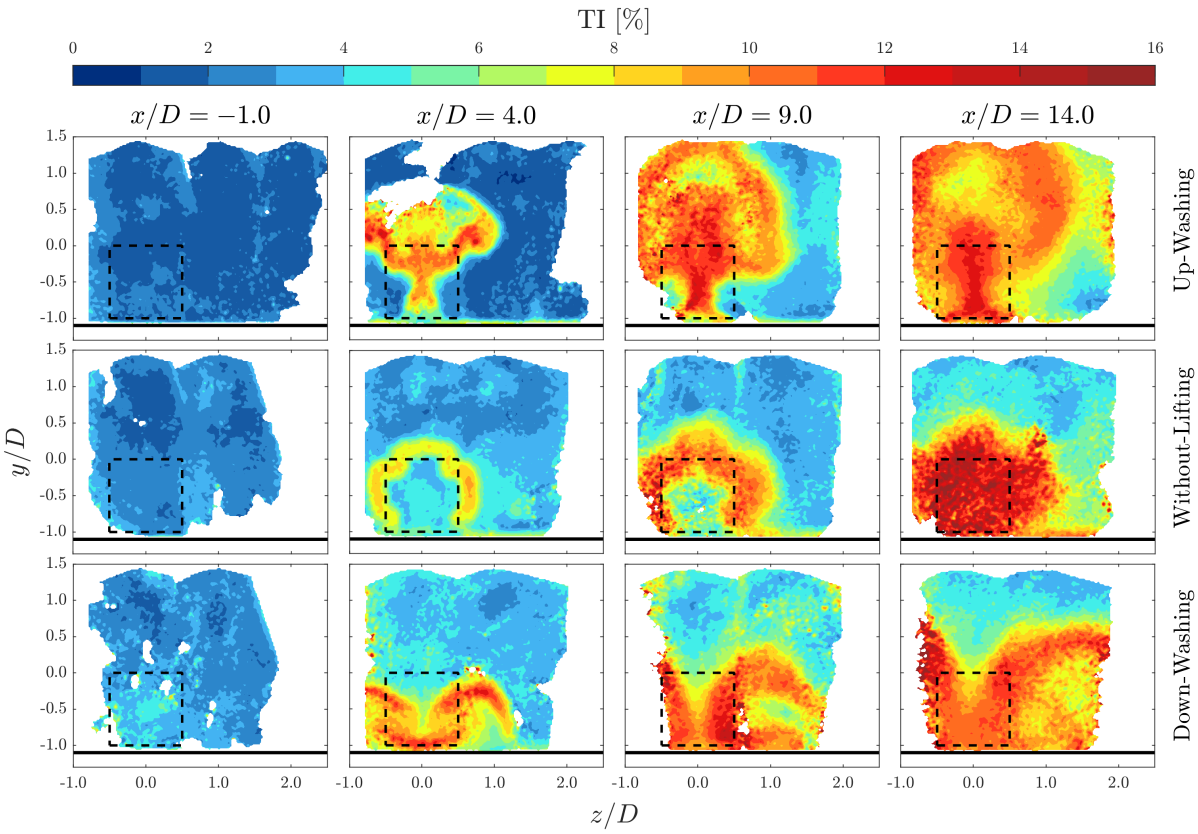

Figure 5.12: The turbulence intensity (TI) expressed as a percentage, is shown for cases with 5D inter-turbine spacing. The first row corresponds to the (**U-05**) case, representing Up-Washing. The second row shows the (**WL-05**) case, representing Without-Lifting, while the third row illustrates the (**D-05**) case, representing Down-Washing. Black dashed lines indicate the MRSL projection area and solid black lines mark the floor. The columns represent cross-sections orthogonal to the freestream direction.

The inflow conditions measured one MRSL width upstream of the first MRSL exhibit low turbulence intensity (TI) values. In the Up-Washing and Without-Lifting cases, TI ranges between 1%

and 4%, while in the Down-Washing cases, some regions display TI values between 4% and 5%. This indicates that the TI is higher than expected from the wind tunnel statistics, suggesting that the inflow region measurements may be affected by uncertainty [65]. However, since the TI values in the other cross-sections are significantly higher, this data can be trusted.

For the Without-Lifting case, turbulence intensity at $x/D = 4.0$ is highest near the edges of the MRSL projection area. This is due to the flow deficit that forms behind the MRSL, causing turbulence intensity to rise in the shear layer between the wake deficit and the freestream velocity bypassing the MRSL. This phenomenon, previously explained as turbulent mixing, is highlighted in this cross-section. In the next cross-section, turbulence intensity increases and extends both toward the center of the MRSL projection area and outward. The second MRSL causes this increase in turbulence intensity, since its obstruction adds more turbulence to the flow, leading to the expansion of the affected region. In the final cross-section, the turbulence intensity forms a closed, circular-like shape, with the entire region inside and around the MRSL projection area exhibiting high turbulence intensity values. Notably, for an extended wind farm, this cross-section is located one MRSL width ahead of the next MRSL. This positioning implies that a potential fourth MRSL would encounter very high turbulence intensity levels, which results in non-uniform blade loading and uneven loading on the support structure.

Examining the Up-Washing case at $x/D = 4.0$, a significantly larger region of higher turbulence intensity (TI) is observed compared to the Without-Lifting case. This region further expands and intensifies at $x/D = 9.0$. The increased TI enhances turbulent mixing, which accelerates the revival of wake deficit regions by facilitating their interaction with high-momentum flow. Although the area of higher TI values grows out of the measurement domain at $x/D = 14.0$, the maximum TI values do not exceed those observed in the previous cross-section. Additionally, the TI values within the MRSL projection area no longer show significant increases—unlike the Without-Lifting case, where such increases are still evident.

The Down-Washing case shows a larger TI compared to the Without-Lifting case and the Up-Washing case. Although the shape of the turbulence region is significantly different, more dark red regions can be seen. The large TI values highlight the shear layer of the splitted wake deficit. Observing the shear layer in Figure 5.3 for the Down-Washing case at $x/D = 4.0$, the shape of the TI plot becomes clear. For the cross-section at $x/D = 9.0$, the TI region grows inside and out of the MRSL projection area. This is seen in the final cross-section too and enhances the turbulent mixing with high-momentum flow. While the previous cross-sections show increased TI compared to the Without-Lifting case, the final cross-section doesn't. The Without-Lifting case shows very high values of TI which is expected to remain for additional rows. Based on the three cross-sections at $x/D = 14.0$, it can be concluded that turbulence intensity within the MRSL projection area is significantly lower in both the Up-Washing and Down-Washing cases compared to the Without-Lifting case. This ensures non-uniform blade loading and non-uniform structural loading are reduced. To examine the turbulence intensity more thoroughly, Figure 5.13 presents a side view at the center of the middle MRSL column.

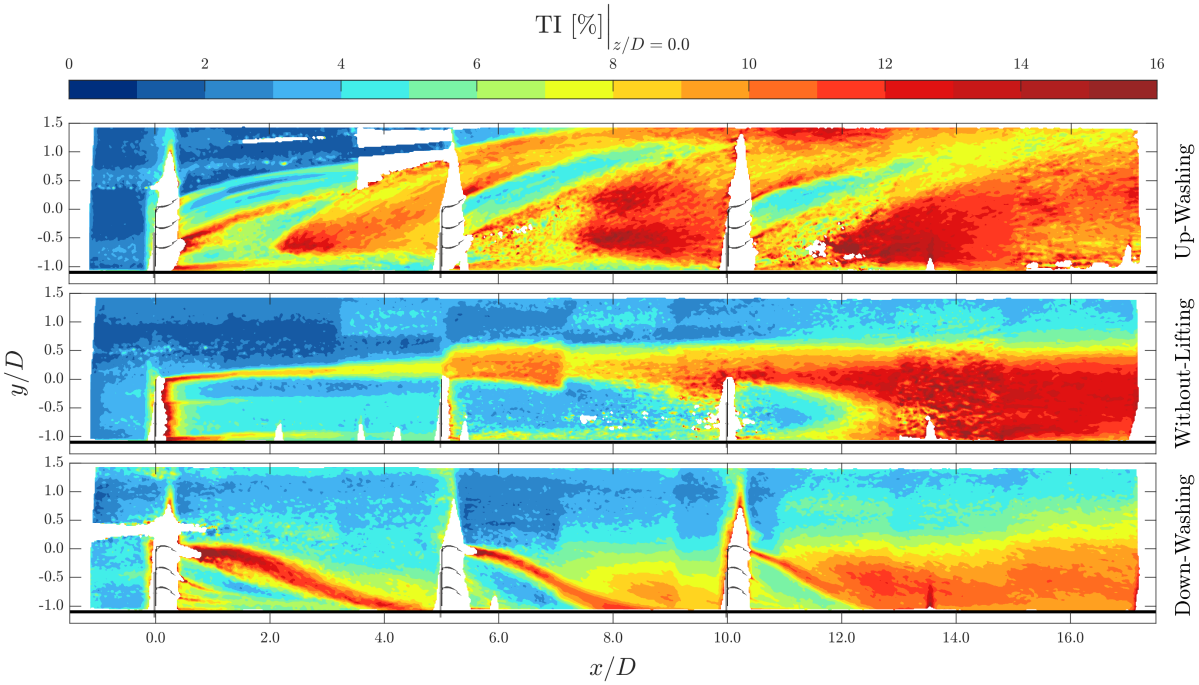

Figure 5.13: The turbulence intensity (TI) expressed as a percentage, evaluated at $z/D = 0.0$, is shown for cases with 5D inter-turbine spacing. The top plot corresponds to the (**U-05**) case, representing Up-Washing. The middle plot depicts the (**WL-05**) case, representing Without-Lifting, while the bottom plot illustrates the (**D-05**) case, representing Down-Washing. The corresponding MRSL configurations show this too. The floor of the regenerative wind farm is indicated by the black horizontal line in all plots.

The Without-Lifting case shows a thin, high-turbulence region immediately behind the MRSL and a trail of high turbulence in the shear layers at both the top and bottom of the MRSL. While the bottom shear layer exhibits a rapid reduction in turbulence intensity (TI), the top shear layer combines a decrease in TI with vertical expansion. This pattern continues with the second and third MRSLs. At $x/D = 12.0$, the center of the wake becomes highly turbulent due to the mixing in the top shear layer and the induced turbulence from the side of the MRSL, as discussed in Figure 5.14.

In the Up-Washing case, a high-TI trail is observed behind the bottom airfoil in the first MRSL, indicating that flow separates along the suction side. A thicker TI region behind the airfoil suggests that the separation occurs closer to the leading edge, reducing the wing's performance. The other two airfoils do not display such a high-TI region, implying only minor flow separation near the trailing edge. Because the airfoils influence each other's performance, the pressure side of the bottom airfoil helps reduce separation in the other two. As discussed in subsection 5.2.2, high-momentum flow from above and beside the MRSL projection area enters at $x/D = 2.0$. This region, marked by high turbulence, grows downstream and in height. Behind the second and third MRSLs, a reduced-TI region is evident, corresponding to the attached flow on the suction side of the top two airfoils. Between $x/D = 10.0$ and $x/D = 12.0$, the intense upwash regions of the first and second MRSLs merge, highlighted by a dark red area at $y/D = 1.5$. This high-TI region likely extends even higher than 1.5 times the MRSL width above the top, though it remains outside the measurement volume.

In the Down-Washing case, the top wing of the first MRSL exhibits a very thick turbulent wake, indicating that flow separates very close to the leading edge and thus suffers reduced performance. Nonetheless, the pressure side of the top wing ensures that the bottom two wings perform significantly better by showing minimal flow separation. This minimal separation for the bottom two airfoils improves further in the subsequent MRSLs, as the top airfoil demonstrates progressive performance enhancements with each MRSL. The TI trail decreases in both thickness and intensity. Additionally, a region of increased TI appears in the far wake of the second MRSL and ex-

pands into that of the third. At $x/D = 16.0$, the reduced TI in the Up-Washing and Down-Washing cases relative to the Without-Lifting case is evident in this cross-section. To further investigate the TI from a side view at the edge of the MRSLs, refer to Figure 5.14.

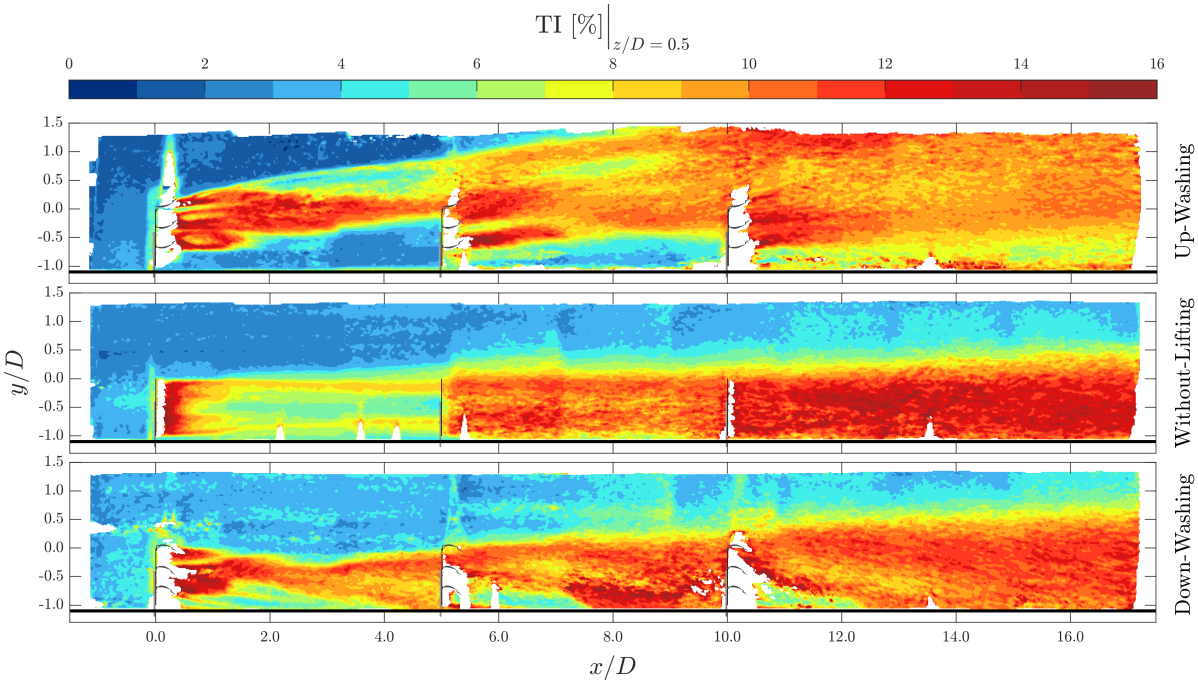

Figure 5.14: The turbulence intensity (TI) expressed as a percentage, evaluated at $z/D = 0.5$, is shown for cases with 5D inter-turbine spacing. The top plot corresponds to the (**U-05**) case, representing Up-Washing. The middle plot depicts the (**WL-05**) case, representing Without-Lifting, while the bottom plot illustrates the (**D-05**) case, representing Down-Washing. The corresponding MRSL configurations show this too. The floor of the regenerative wind farm is indicated by the black horizontal line in all plots.

The Without-Lifting case shows increased turbulence intensity (TI) behind the first MRSL compared to the previous cross-section. This is because this cross-section intersects the vertical shear layer at the side of the MRSL. The far wake of the first MRSL shows reduced TI, as the shear layer moves outboard of the MRSL projection area, as previously seen in Figure 5.12. Since the shear layer expands laterally in both directions, it is visible behind the second and third MRSLs. Moreover, the TI in the layer above the MRSLs exhibits very low values, indicating minimal interaction with the higher layers above the wind farm.

For the Up-Washing case, the wake of the first MRSL displays a highly turbulent region at the edge of the wings, which quickly diminishes in the far wake. In the wake of the second MRSL, a large region with moderately increased TI values is observed. Behind the third MRSL, this region extends toward the floor, meaning that after three MRSLs, a vertical region of more than 2.5D experiences significant TI—one of the driving factors for wake recovery.

The Down-Washing case shows an increase in TI values that continues to grow vertically, with the TI region expanding upward linearly. Due to the position of the wings, the far wake of every MRSL exhibits high TI values near the floor. Figure 5.15 displays the TI values at $z/D = 1.0$.

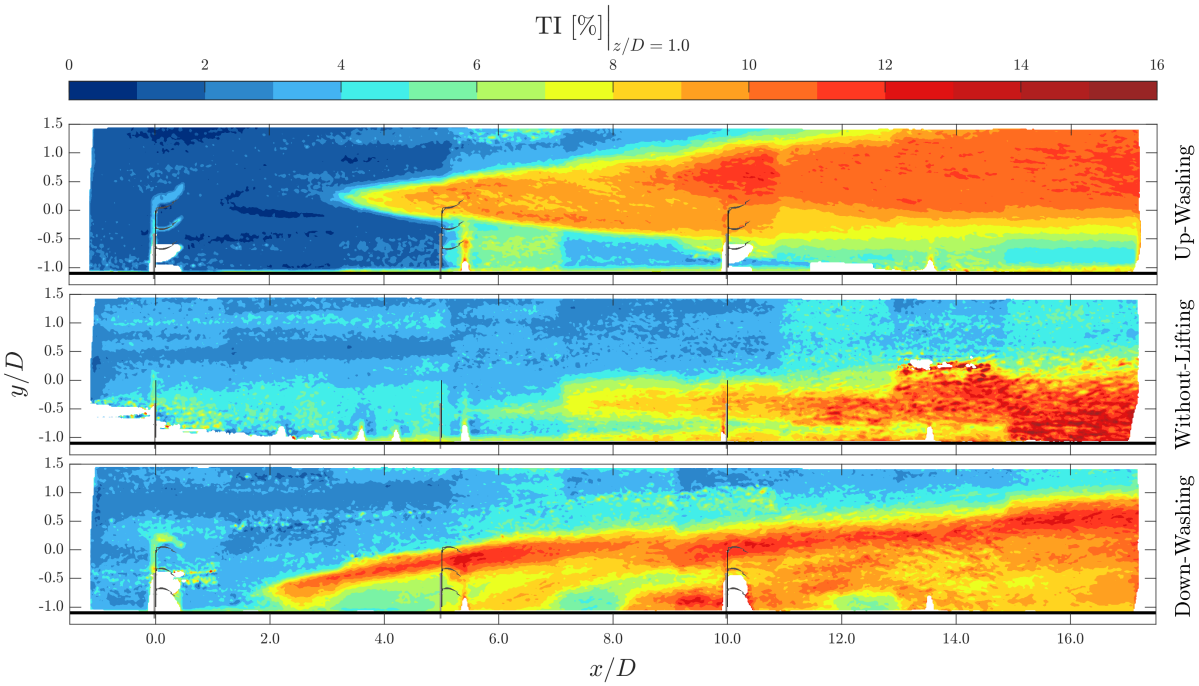

Figure 5.15: The turbulence intensity (TI) expressed as a percentage, evaluated at $z/D = 1.0$, is shown for cases with 5D inter-turbine spacing. The top plot corresponds to the (**U-05**) case, representing Up-Washing. The middle plot depicts the (**WL-05**) case, representing Without-Lifting, while the bottom plot illustrates the (**D-05**) case, representing Down-Washing. The corresponding MRSL configurations show this too. The floor of the regenerative wind farm is indicated by the black horizontal line in all plots.

The Without-Lifting case shows an increased turbulence region starting from $x/D = 7.0$, which grows downstream. The turbulent shear layer outlines the edge of the wake deficit, as shown in Figure 5.6, where the wake deficit region is clearly visible. Comparing this case to the Up-Washing and Down-Washing cases, it is evident that turbulent mixing with the high-momentum flow between wind farm columns is minimal for the Without-Lifting case but very significant for the other two cases.

5.2.5. Concluding Remarks on 5D Row Spacing Cases

In conclusion, for the 5D row spacing cases, the flow field analysis demonstrates that the second and third rows in the wind farm significantly enhance MRSL thrust forces in both the Up-Washing and Down-Washing cases. The increased velocity within the MRSL projection area is driven by high advection values, as indicated by the vertical velocity plots. The vorticity induced by the wings generates large circulation regions, ensuring that high-momentum flow enters the wind farm layer and MRSL projection area. This effect is evident in the flow field results. Additionally, the Up-Washing and Down-Washing cases exhibit much larger regions of turbulence intensity compared to the Without-Lifting case. As previously established, advection and turbulence are the primary drivers of wake recovery. While it is challenging to determine which configuration performs better based solely on the flow field data, load measurements confirm that Up-Washing outperforms Down-Washing. The added benefit of increased thrust on the first MRSL is also seen in the flow field results.

5.3. PTV Results for 10D Row Spacing

This section presents and discusses the PTV results from the regenerative wind farm experiment for the 10D inter-turbine spacing cases. First, two types of cross-sections of the streamwise velocity are presented. Next, the same cross-sections are used to illustrate the vertical velocity component. Finally, different cross-sections of the vorticity field are analyzed. It is worth noting that for the 10D cases, only two MRSLs are configured.

5.3.1. Streamwise Velocity

Similar to Figure 5.3, the streamwise velocity for the 10D row spacing cases is shown in Figure 5.16. Note that, due to the similar inflow conditions for the 5D row spacing cases, the cross-section at $x/D = 1.0$ is not included. Instead, the cross-section at $x/D = 17.0$ is presented to emphasize the far-wake analysis in this study.

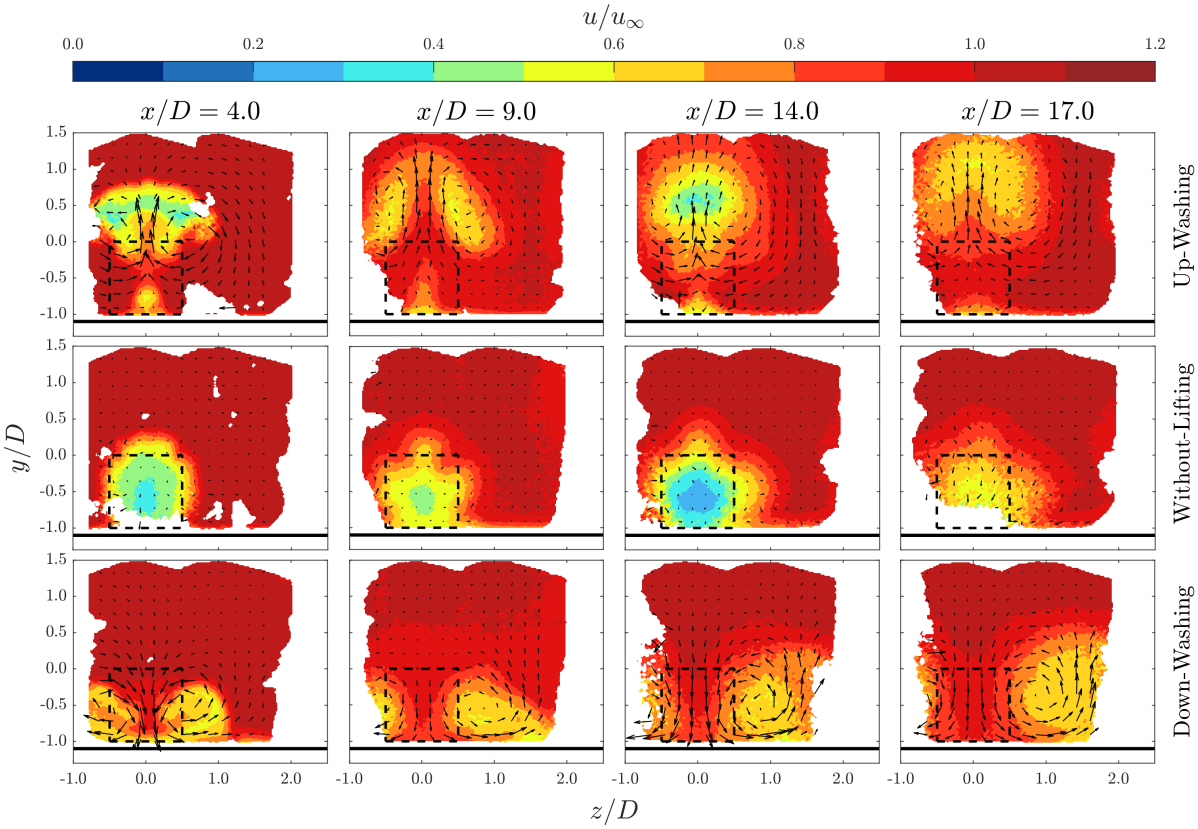

Figure 5.16: The mean streamwise velocity component, u, normalized by the freestream velocity, u_∞, is shown for cases with 10D inter-turbine spacing. The first row corresponds to the (**U-10**) case, representing Up-Washing. The second row shows the (**WL-10**) case, representing Without-Lifting, while the third row illustrates the (**D-10**) case, representing Down-Washing. Black dashed lines indicate the MRSL projection area and solid black lines mark the floor. Arrows depict the in-plane velocity.

For the Without-Lifting case at $x/D = 4.0$, the velocity field exhibits a similar wake expansion compared to the 5D row spacing case shown in Figure 5.3. However, the wake deficit behind the MRSL projection area is slightly smaller in comparison. The next cross-section, located nine MRSL widths downstream and one MRSL width ahead of the second MRSL, reveals wake expansion accompanied by a reduced wake deficit. The shear layer becomes less sharp due to turbulent mixing, which facilitates the reduced wake deficit. At the cross-section $x/D = 14.0$, positioned four MRSL widths downstream of the second MRSL, a reduction in streamwise velocity values is observed, as indicated by the larger blue area. This reduction is accompanied by further wake expansion, highlighted by a less distinct shear layer. At the final cross-section, the wake expansion does not show significant changes. The shear layer remains comparable, but the center of

the wake deficit region exhibits signs of increased recovery, evidenced by the reduced blue area. The arrows in all cross-sections show almost no in-plane velocities.

The first cross-section for the Up-Washing case shows results very similar to those of the 5D row spacing case in Figure 5.3. While this is expected, it underscores the consistency of the experiment. The second cross-section at $x/D = 9.0$ reveals a pattern not observed previously. The increased row spacing causes the green and yellow regions (from the earlier cross-section) to transition into an orange region well above the MRSL projection area. The wake shape also changes noticeably. The wake region begins to split into two, as the arrows in the center of the wake indicate higher vertical velocities compared to the sides. Within the MRSL projection area, velocities approach the freestream value, except near the bottom center. The subsequent two cross-sections show results similar to those for the 5D row spacing case. The second MRSL pushes the wake upward, forming a circular shape above the MRSL projection area. In the final cross-section, higher streamwise velocity values are observed in the MRSL projection area compared to $x/D = 14.0$. This occurs because the wake deficit region retains upward momentum beyond four MRSL widths downstream. This momentum is still there in $x/D = 17.0$ as indicated by the arrows.

For the Down-Washing case, both the expansion and direction of the wake remain similar to those observed in the 5D row spacing cases. The only notable difference for this row spacing is in the velocity values within the wake deficit. In this figure, the wake predominantly displays orange colors, whereas in Figure 5.3, the wake shows mostly yellow and even green regions. The results are logical, as the absence of the third MRSL means less energy is harvested, resulting in less pronounced wake deficit regions.

The cross-sections from the side for the 10D row spacing cases are also presented. The $z/D = 0.0$ cross-section can be seen in Figure 5.17. The figure also indicates the turbine configurations which are positioned at $x/D = 0$ and 10.

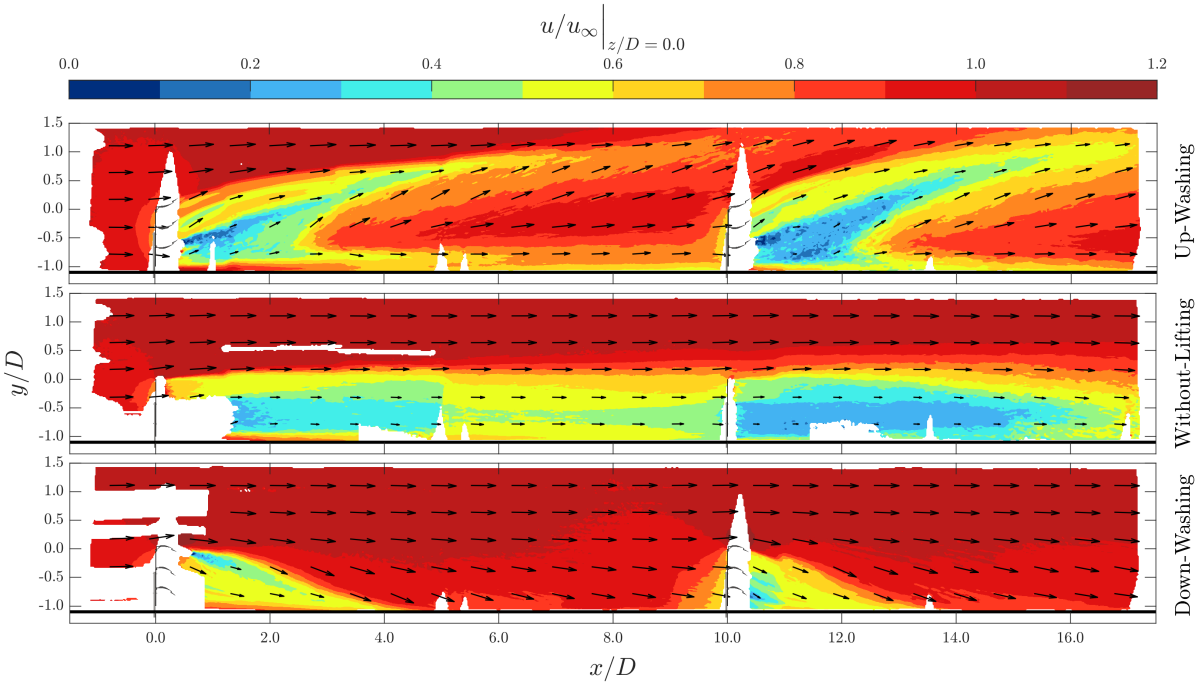

Figure 5.17: The mean streamwise velocity component, u, normalized by the freestream velocity, u_∞, evaluated at $z/D = 0.0$ which is the MRSL center, is shown for cases with 10D inter-turbine spacing. The top plot corresponds to the (**U-10**) case, representing Up-Washing. The middle plot depicts the (**WL-10**) case, representing Without-Lifting, while the bottom plot illustrates the (**D-10**) case, representing Down-Washing. The corresponding MRSL configurations show this too. Arrows represent the in-plane velocity. The floor of the regenerative wind farm is indicated by the black horizontal line in all plots.

The Without-Lifting case produces results similar to those observed in the 5D row spacing case, as shown in Figure 5.4. There is minimal wake expansion compared to the other two cases. While the shear layer becomes slightly less sharp, the effect remains minimal. Wake recovery behind the first MRSL is evident; however, the abrupt transition from blue to yellow in the wake at $x/D \approx 5.0$ is not a physical phenomenon but is likely a stitching-related occurrence. The wake deficit behind the second MRSL is less pronounced (less dark blue) compared to the 5D case, indicating improved wake recovery with increased turbine spacing.

The Up-Washing case highlights the effects of the lifting devices in a more isolated manner. With the second MRSL positioned farther away, the wake of a single MRSL can be studied in greater detail. Starting from $x/D = 4.0$, an increased high-momentum region is observed. While this region was present in the 5D case, it now has more opportunity to expand. The far wake near the floor still shows some wake deficit, which is reasonable, as the counter-rotating circulation in the wake does not easily reach this area. When comparing the Up-Washing case to the Without-Lifting case, it is evident that the wake region is lifted upward and also reduced in overall size. The next cross-section should confirm whether this trend holds across the entire lateral expansion of the wake.

The Down-Washing case presents a very similar pattern to the 5D case. The MRSL directs the wake downward and outward, though the latter effect is not visible in this cross-section. Following this downwash, a high-momentum region extends up to the next MRSL. Examining the wake region behind the top wing of both MRSLs, it is evident that the second MRSL has a better-performing wing with reduced drag. This is reflected in the total wake of the second MRSL, as its wake region is shorter. Specifically, for the second MRSL, the wake region is approximately one MRSL width shorter in this cross-section. Figure 5.5 shows the streamwise velocity at the edge of the MRSLs at $z/D = 0.5$.

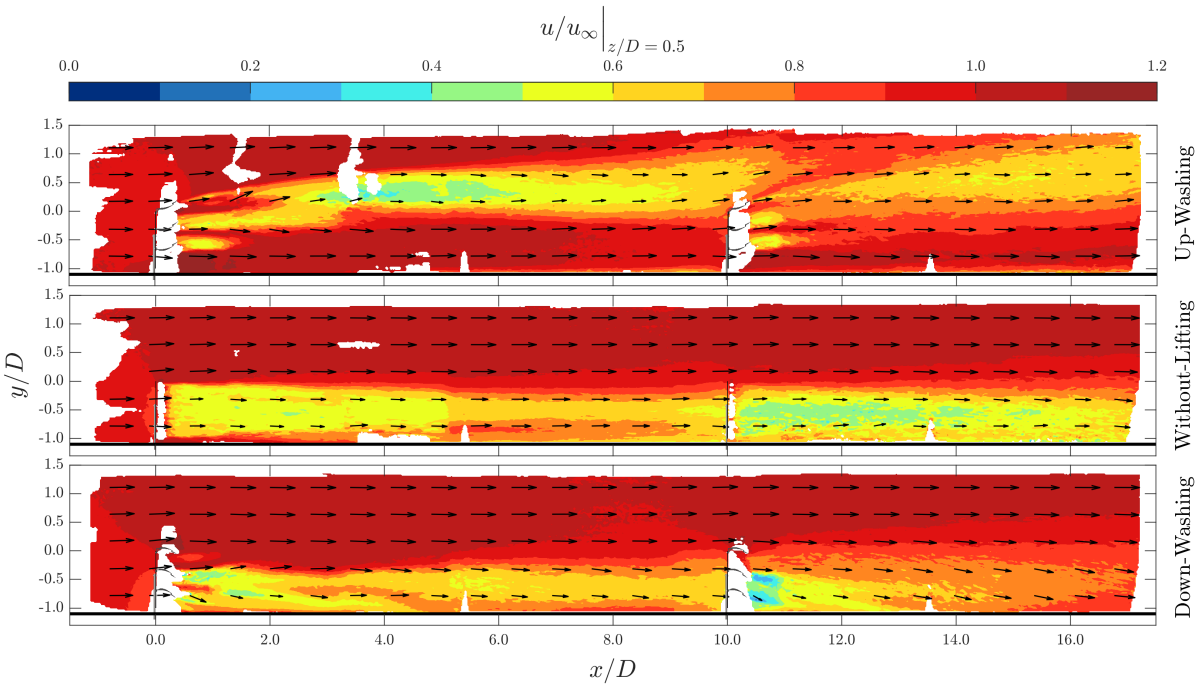

Figure 5.18: The mean streamwise velocity component, u, normalized by the freestream velocity, u_∞, evaluated at $z/D = 0.5$ which is the MRSL edge, is shown for cases with 10D inter-turbine spacing. The top plot corresponds to the (**U-10**) case, representing Up-Washing. The middle plot depicts the (**WL-10**) case, representing Without-Lifting, while the bottom plot illustrates the (**D-10**) case, representing Down-Washing. The corresponding MRSL configurations show this too. Arrows represent the in-plane velocity. The floor of the regenerative wind farm is indicated by the black horizontal line in all plots.

The Without-Lifting case demonstrates results similar to those of the 5D case. The wake deficit decreases at the edge of the MRSL compared to the center. Additionally, the wake exhibits higher streamwise velocity values because only two MRSLs are generating thrust forces. In the Up-Washing case, the lateral expansion of the wake was previously discussed. This cross-section confirms that the wake indeed decreases in overall size. The wake region is less pronounced compared to the Without-Lifting case, except in the region between $x/D = 2.0$ and $x/D = 6.0$. This occurs due to the earlier mentioned phenomenon where the wake splits behind the first MRSL. The Down-Washing case exhibits similar behavior to the 5D case. This cross-section reveals that the wake region shifts outward, as already observed in Figure 5.16. To analyze the behavior of the wake between rows of the wind farm, Figure 5.19 is presented next.

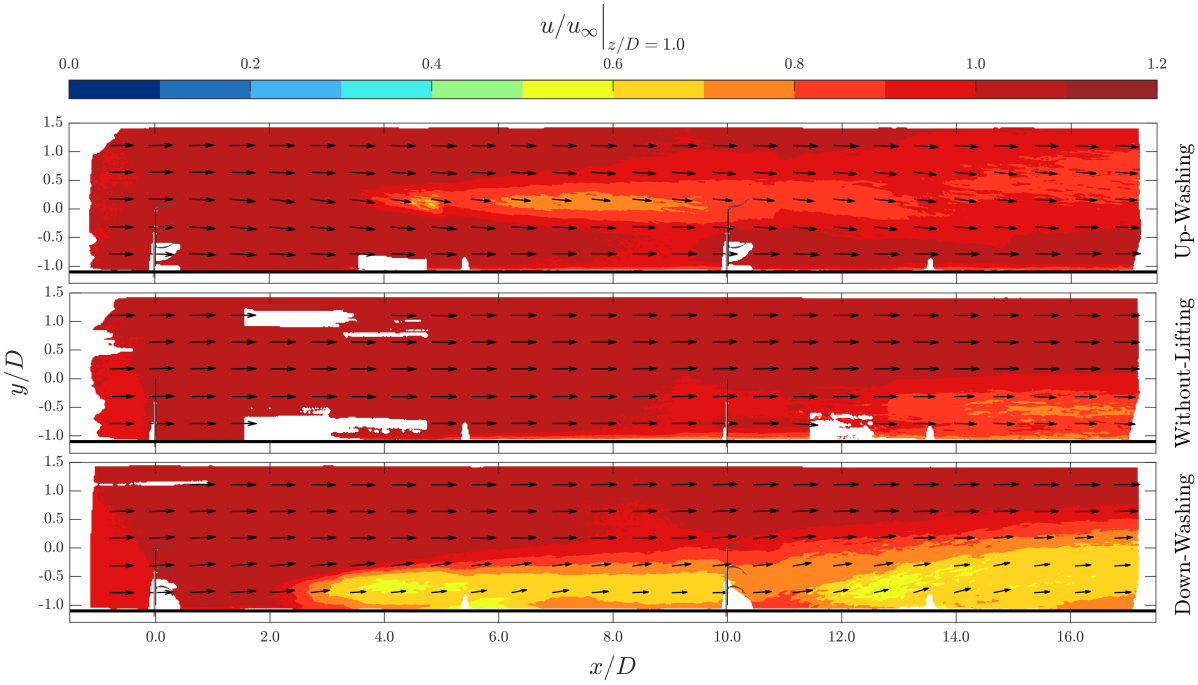

Figure 5.19: The mean streamwise velocity component, u, normalized by the freestream velocity, u_∞, evaluated at $z/D = 1.0$, is shown for cases with 10D inter-turbine spacing. The top plot corresponds to the (**U-10**) case, representing Up-Washing. The middle plot depicts the (**WL-10**) case, representing Without-Lifting, while the bottom plot illustrates the (**D-10**) case, representing Down-Washing. The corresponding MRSL configurations show this too. Arrows represent the in-plane velocity. The floor of the regenerative wind farm is indicated by the black horizontal line in all plots.

The Without-Lifting case shows almost no lateral expansion of the wake. Only a small region near the end of the wake of the second MRSL exhibits a slight reduction in freestream velocity, indicating that the wake has some influence in this lateral position. The Up-Washing case, while showing slightly more wake deficit than the Without-Lifting case, still exhibits minimal wake deficit in this cross-section. The upwashing principle has now been reviewed multiple times. In this case, the wake remains centered along the column but is shifted significantly upward. For the Down-Washing case, the wake is displaced laterally to the sides between MRSL columns while remaining at the height of the MRSL. This mechanism ensures that upwashing introduces high-momentum flow into the sides of the MRSL projection area, while downwashing entrains high-momentum flow from above. The next section quantifies the vertical velocity values once more, this time for the 10D row spacing cases.

5.3.2. Vertical Velocity

The vertical velocity component for the regenerative wind farm is shown in Figure 5.20, using the same cross-sections as depicted in Figure 5.16. This component is normalized by the freestream velocity, and the color bar values remain consistent with those used for the 5D spacing cases, ensuring a fair comparison.

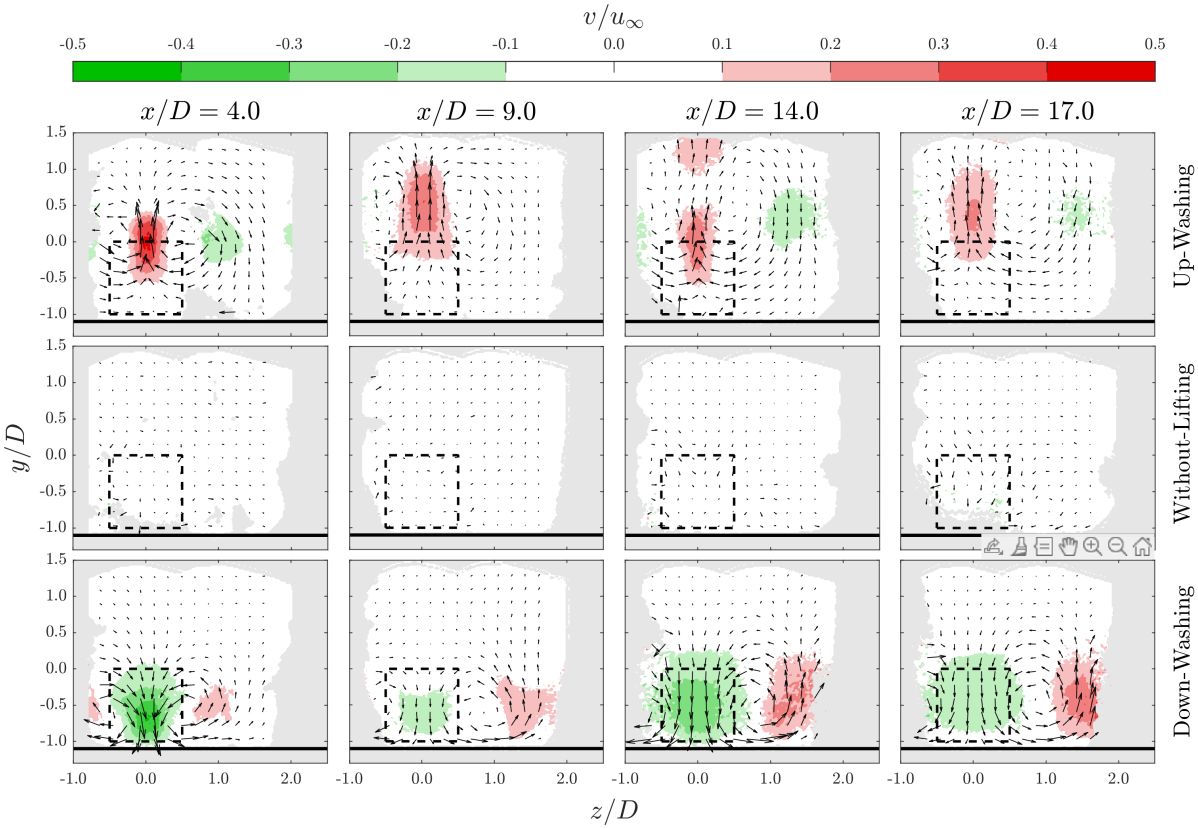

Figure 5.20: The mean vertical velocity component, v, normalized by the freestream velocity, u_∞, is shown for cases with 10D inter-turbine spacing. The first row corresponds to the (**U-10**) case, representing Up-Washing. The second row shows the (**WL-10**) case, representing Without-Lifting, while the third row illustrates the (**D-10**) case, representing Down-Washing. Black dashed lines indicate the MRSL projection area and solid black lines mark the floor. Arrows depict the in-plane velocity.

The Without-Lifting case shows no vertical velocity values larger than 10% or smaller than -10% of the freestream velocity. The 5D row spacing case did show some larger values in the wake of the third MRSL. This can be clarified by the fact that only two MRSLs are used which reduces the amount of turbulence in the wake.

For the Up-Washing case, the cross-section at $x/D = 4.0$ shows a similar result to the 5D case. However, this similarity does not persist in the next cross-section. Since there is no MRSL at $x/D = 5.0$, the vertical velocity region is less pronounced and positioned higher, as the wake remains undisturbed and continues to rise. Additionally, the downwash region exhibits smaller values compared to the 5D case. The cross-section at $x/D = 14.0$ also shows similar results to the 5D case, except for the vertical velocity region at the top of the cross-section. This region corresponds to the vertical velocity generated by the first MRSL and is visible in Figure 5.21. The fact that the cross-section at $x/D = 14.0$ appears similar for both row spacing cases indicates that the strength of the upwash and downwash does not accumulate with the addition of another MRSL. The final cross-section reveals a familiar velocity field, with distinct upwash and downwash regions. This observation confirms that the downwash region accumulates strength behind the wakes of the first and second MRSLs.

The first cross-section of the Down-Washing case shows a similar velocity field compared to the 5D row spacing. This is as expected since until now there is no difference in configuration experienced by the flow. The next cross-section shows a reduced down-wash region and an increased upwash region. The downwashing region is significantly reduced compared to the Up-Washing case at this cross-section. The absence of accumulation of up and down wash from the Up-Washing case is present for the Down-Washing case. The $x/D = 14.0$ cross-section with 5D rotor spacing which was shown in Figure 5.7 shows larger and and stronger regions of up and down wash. Moving another three MRSL widths downstream, the up and down wash remains significant. Something that was not seen at $x/D = 9.0$ behind the first MRSL.

The first cross-section of the Down-Washing case shows a velocity field similar to that of the 5D row spacing case. This is expected, as the flow has not yet experienced any configuration differences. In the next cross-section, the downwash region is reduced, while the upwash region is increased. At this point, the downwash region is significantly smaller compared to the upwash region in the Up-Washing case. Whereas the Up-Washing case did not experience accumulation of up and down wash region by the second MRSL, this does happen for the Down-Washing case. The $x/D = 14.0$ cross-section for the 5D rotor spacing, as shown in Figure 5.7, exhibits larger and stronger regions of upwash and downwash compared to the 10D row spacing case. Finally looking at another three MRSL widths downstream, these upwash and downwash regions remain significant—an observation not seen at $x/D = 9.0$ behind the first MRSL. Figure 5.21 illustrates the upwash and downwash from a side view of the farm at the center of the MRSLs.

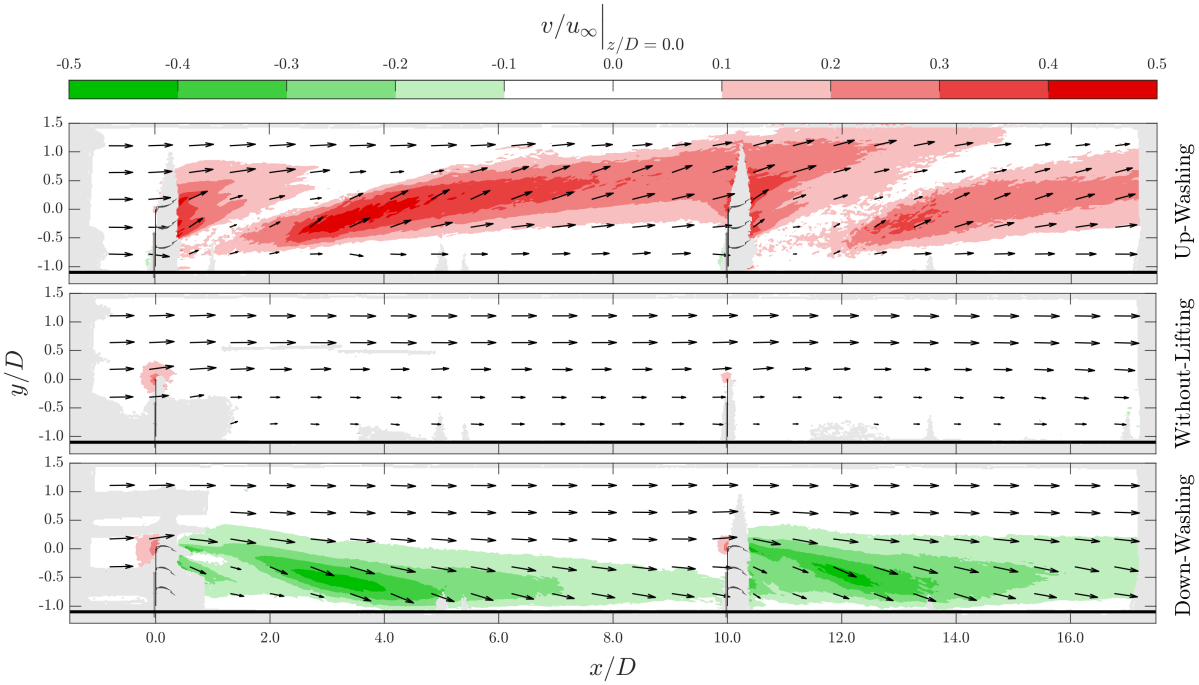

Figure 5.21: The mean vertical velocity component, v, normalized by the freestream velocity, u_∞, evaluated at $z/D = 0.0$, is shown for cases with 10D inter-turbine spacing. The top plot corresponds to the (**U-10**) case, representing Up-Washing. The middle plot depicts the (**WL-10**) case, representing Without-Lifting, while the bottom plot illustrates the (**D-10**) case, representing Down-Washing. The corresponding MRSL configurations show this too. Arrows represent the in-plane velocity. The black horizontal line in all plots indicates the floor of the regenerative wind farm.

The Without-Lifting case shows results similar to those observed in the 5D row spacing cases, as illustrated in Figure 5.8. There is no vertical interaction apart from the stream tube expansion near the actuator surfaces. In the Up-Washing case, the same distinction between two upwashing regions behind the wake of the first MRSL is observed. The first region is the direct upwash induced by the wakes, while the second arises from the high-momentum flow that bypasses the MRSL but is captured by the induced rotation in the flow. This second upwash region connects with the upwash generated by the wings of the second MRSL, a phenomenon noted earlier. Ulti-

mately, the high-momentum flow becomes entrained, creating the second upwash region behind the second MRSL. In the Down-Washing case, the wake behind the first MRSL exhibits a small distinction between the two regions. This result is expected, as high-momentum flow is entrained from above rather than from the sides, making the distinction less pronounced compared to the Up-Washing case. Additionally, the Down-Washing case produces results similar to those of the 5D row spacing case.

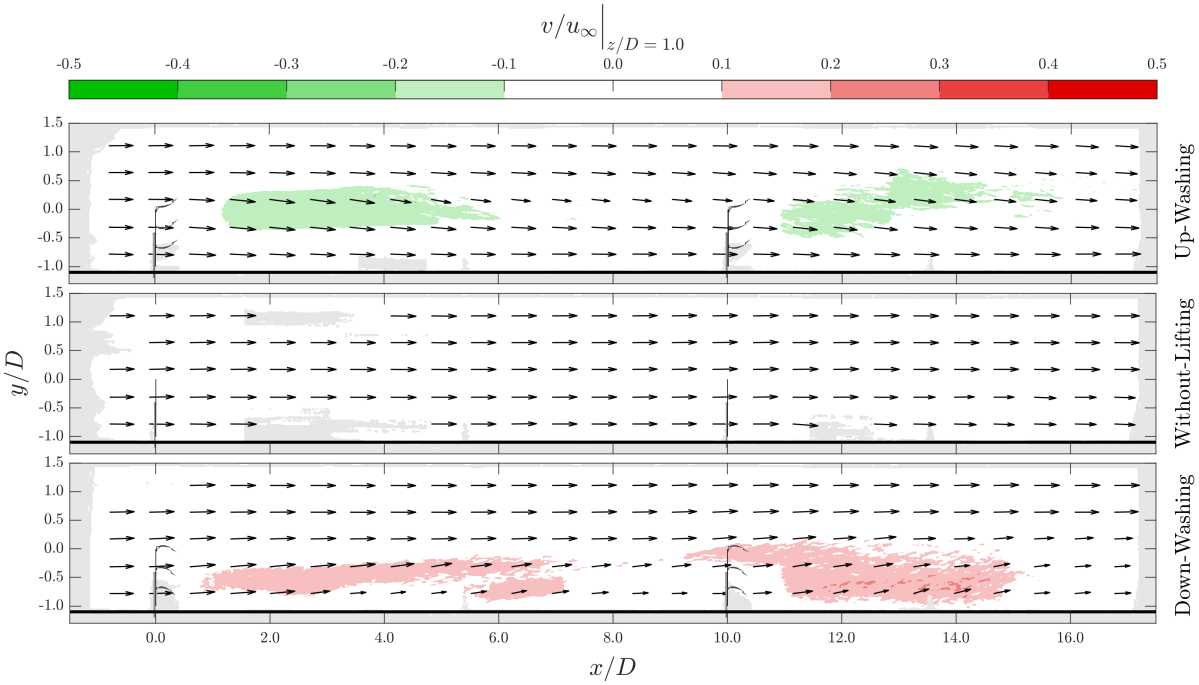

Figure 5.22: The mean vertical velocity component, v, normalized by the freestream velocity, u_∞, evaluated at $z/D = 1.0$, is shown for cases with 10D inter-turbine spacing. The top plot corresponds to the (**U-10**) case, representing Up-Washing. The middle plot depicts the (**WL-10**) case, representing Without-Lifting, while the bottom plot illustrates the (**D-10**) case, representing Down-Washing. The corresponding MRSL configurations show this too. Arrows represent the in-plane velocity. The black horizontal line in all plots indicates the floor of the regenerative wind farm.

Figure 5.22 highlights the rotation in the flow. In the Up-Washing case, a downwash region is observed at this cross-section, while in the Down-Washing case, an upwash region is present. Additionally, the upwash region in the Down-Washing case is more pronounced compared to the downwash region in the Up-Washing case, as the wake region in this case shifts laterally rather than vertically.

5.3.3. Streamwise Vorticity

The vortex cores induced by the wings are also evaluated for the 10D row spacing cases, with the results shown in Figure 5.23. This figure displays streamwise cross-sections at one and two MRSL widths downstream for both MRSLs. While the vortex cores in the wake of the first MRSL are not diffused at $x/D = 2.0$, similar behavior was observed in Figure 5.10 and is therefore not presented again.

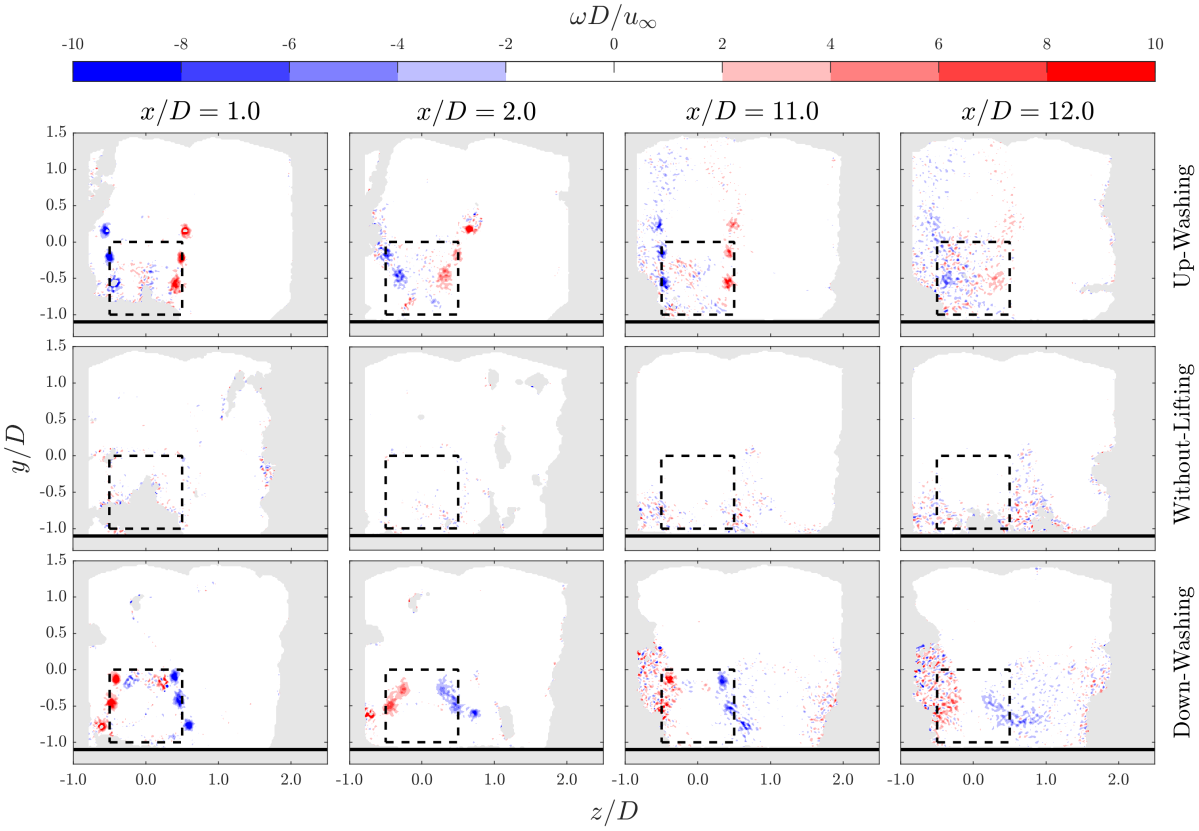

Figure 5.23: The streamwise vorticity, ω, normalized by multiplying with the rotor width D and dividing by the freestream velocity, u_∞, is shown for cases with 5D inter-turbine spacing. The first row corresponds to the (**U-05**) case, representing Up-Washing. The second row shows the (**WL-05**) case, representing Without-Lifting, while the third row illustrates the (**D-05**) case, representing Down-Washing. Black dashed lines indicate the MRSL projection area and solid black lines mark the floor.

The Without-Lifting case does not exhibit any strong vorticity across all cross-sections, as expected due to the absence of lifting devices. In the Up-Washing case, the cross-sections in the wake of the first MRSL show results consistent with earlier observations. At $x/D = 11.0$, six vortex cores are visible once again. While these cores appear slightly more pronounced in this figure, the cross-section shows similarities with the $x/D = 6.0$ cross-section in Figure 5.11. The subsequent cross-section no longer displays distinct vortex cores, instead revealing a diffused region of vorticity. This indicates that increasing the inter-turbine spacing does not enhance the propagation of vortex cores in the wake but the cores show slightly increased strength. In the Down-Washing case, the cross-sections in the wake of the first MRSL show results consistent with earlier observations as well. The cross-section at $x/D = 11.0$ is similar to $x/D = 6.0$ in Figure 5.11 whereas for the 10D row spacing case, vortex cores are more pronounced. The vortex cores are diffused in $x/D = 12.0$. This means the conclusion for the Up-Washing case holds for the Down-Washing case too.

5.3.4. Turbulence Intensity

For the 10D row spacing cases, turbulence intensity is also presented. As mentioned earlier, turbulence intensity quantifies the level of turbulence in the flow. Streamwise cross-sections are shown in Figure 5.24.

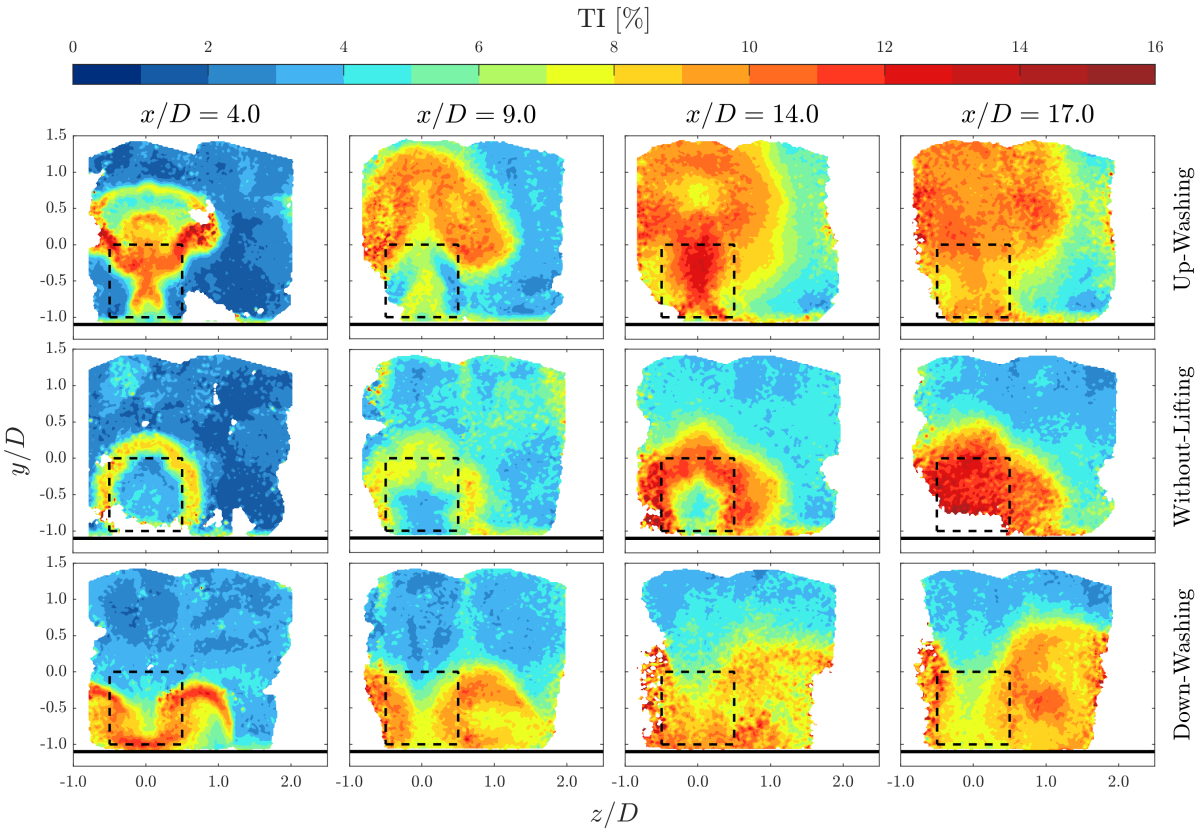

Figure 5.24: The turbulence intensity (TI) expressed as a percentage, is shown for cases with 10D inter-turbine spacing. The first row corresponds to the (**U-10**) case, representing Up-Washing. The second row shows the (**WL-10**) case, representing Without-Lifting, while the third row illustrates the (**D-10**) case, representing Down-Washing. Black dashed lines indicate the MRSL projection area and solid black lines mark the floor. The columns represent cross-sections orthogonal to the freestream direction.

For all cross-sections at $x/D = 4.0$, no significant differences compared to the 5D row spacing cases are observed. This outcome is expected, as the setup remains similar up to this cross-section. However, at the next cross-section, clear differences emerge. While the 5D row spacing case exhibits increased turbulence intensity (TI) and a larger region of high TI values, the 10D case shows a reduction in maximum TI values coupled with a larger area of medium TI. This result aligns with expectations, as no additional MRSL is introduced to generate new turbulence, allowing the turbulence from the first MRSL to dissipate over a larger area. Additionally, in the Up-Washing case, the MRSL projection area displays blue regions, indicating that the second MRSL is not subjected to heavy turbulence in the inflow. In contrast, the MRSL projection area of the Down-Washing case remains more turbulent.

In the Without-Lifting case, the last two cross-sections reveal that with two MRSLs and increased turbine spacing, the entire wake becomes highly turbulent. The reduced TI center observed at $x/D = 14.0$ disappears by $x/D = 17.0$. This indicates that despite the increased inter-turbine spacing, two MRSLs generate a uniformly high-TI region in the far wake of the second MRSL. As previously discussed, this results in unfavorable structural and blade loading. In the Down-Washing case, TI is significantly reduced in both cross-sections at $x/D = 14.0$ and $x/D = 17.0$. For the Up-Washing case, TI remains significant at $x/D = 14.0$ but shows a substantial reduction by $x/D = 17.0$. However, it is important to note that TI in the Up-Washing case remains higher

compared to the Down-Washing case. To gain a more comprehensive understanding of turbulence intensity within the wind farms, side views are provided. The first side view at the center of the MRSLs is shown in Figure 5.25.

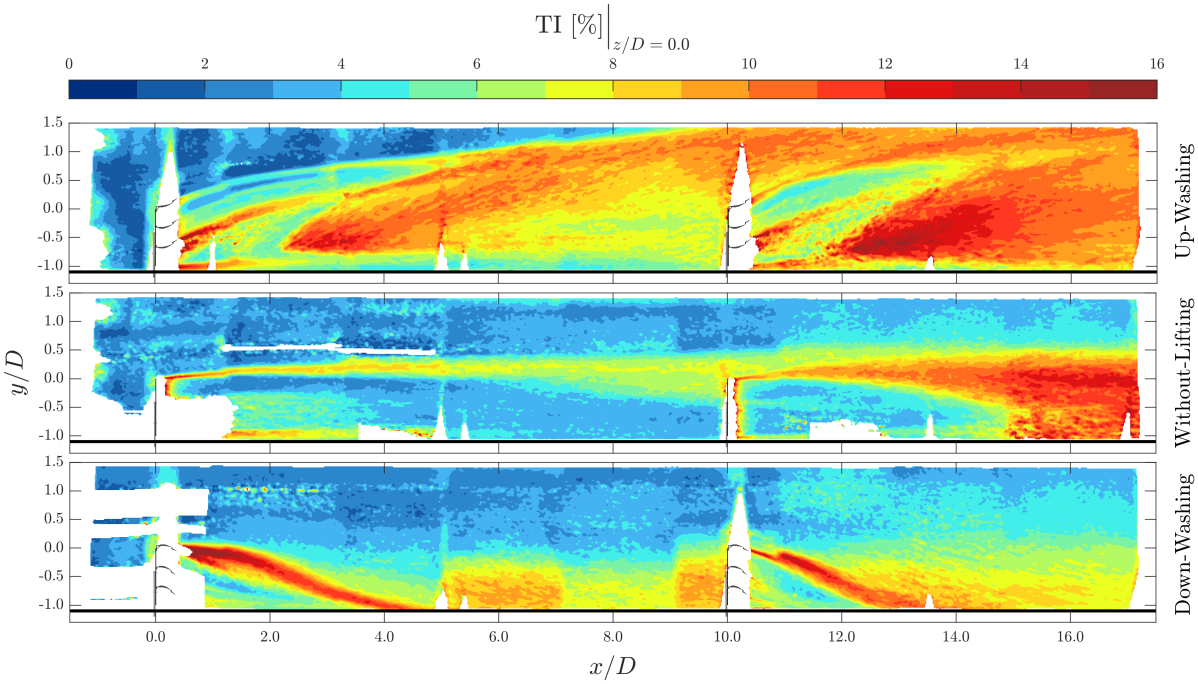

Figure 5.25: The turbulence intensity (TI) expressed as a percentage, evaluated at $z/D = 0.0$, is shown for cases with 10D inter-turbine spacing. The top plot corresponds to the (**U-10**) case, representing Up-Washing. The middle plot depicts the (**WL-10**) case, representing Without-Lifting, while the bottom plot illustrates the (**D-10**) case, representing Down-Washing. The corresponding MRSL configurations show this too. The black horizontal line in all plots indicates the floor of the regenerative wind farm.

The Without-Lifting case exhibits a clear expansion of the shear layer in the wake of the first MRSL, where turbulent mixing helps break down the wake deficit region. In the wake of the second MRSL, the center of the wake becomes highly turbulent at $x/D = 15.0$. Referring back to Figure 5.13, a similar phenomenon occurred earlier, at $x/D = 12.0$, in the case of three MRSLs.

The Up-Washing case produces results similar to the 5D row spacing case. However, the region in front of the second MRSL shows reduced turbulence intensity (TI), indicating that increasing the inter-turbine spacing reduces the TI values experienced by the MRSL—a trend also observed in the previous figure.

The Down-Washing case demonstrates reduced TI in the far wake of the MRSL compared to the 5D row spacing case. Additionally, the performance of the top wing improves in the second MRSL compared to the first. Despite this improvement, the 5D case exhibits a reduced TI region behind the wing of the second MRSL. This suggests that increasing the inter-turbine spacing results in more neutral inflow conditions, which slightly reduces the effectiveness of the top wing in downstream MRSLs. Figure 5.26 presents the turbulence intensity at the edges of the MRSLs.

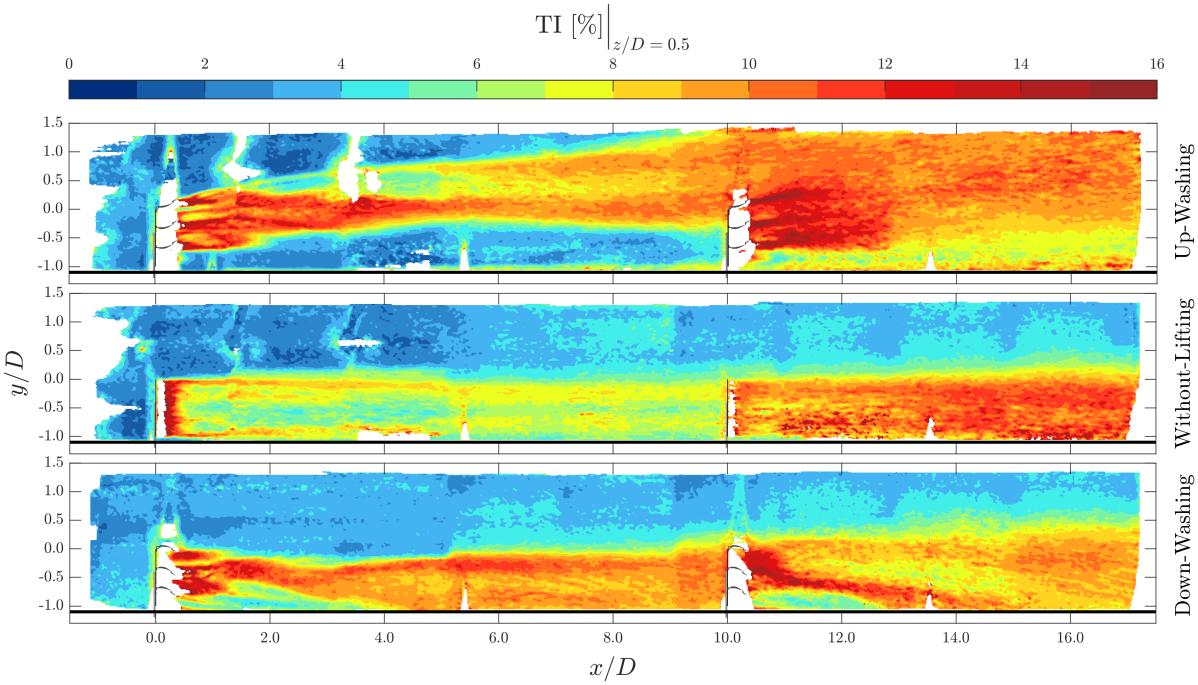

Figure 5.26: The turbulence intensity (TI) expressed as a percentage, evaluated at $z/D = 0.5$, is shown for cases with 10D inter-turbine spacing. The top plot corresponds to the (**U-10**) case, representing Up-Washing. The middle plot depicts the (**WL-10**) case, representing Without-Lifting, while the bottom plot illustrates the (**D-10**) case, representing Down-Washing. The corresponding MRSL configurations show this too. The black horizontal line in all plots indicates the floor of the regenerative wind farm.

Examining all three cross-sections simultaneously reveals that the results resemble a stretched version of the wakes of the first two MRSLs in the 5D row spacing cases. Additionally, the Without-Lifting and Down-Washing cases exhibit significantly reduced turbulence intensity (TI) in the far wake of the second MRSL compared to the 5D case. However, this is not observed in the far wake of the Up-Washing case, which shows similar TI values. Figure 5.27 presents the side view at $z/D = 1.0$.

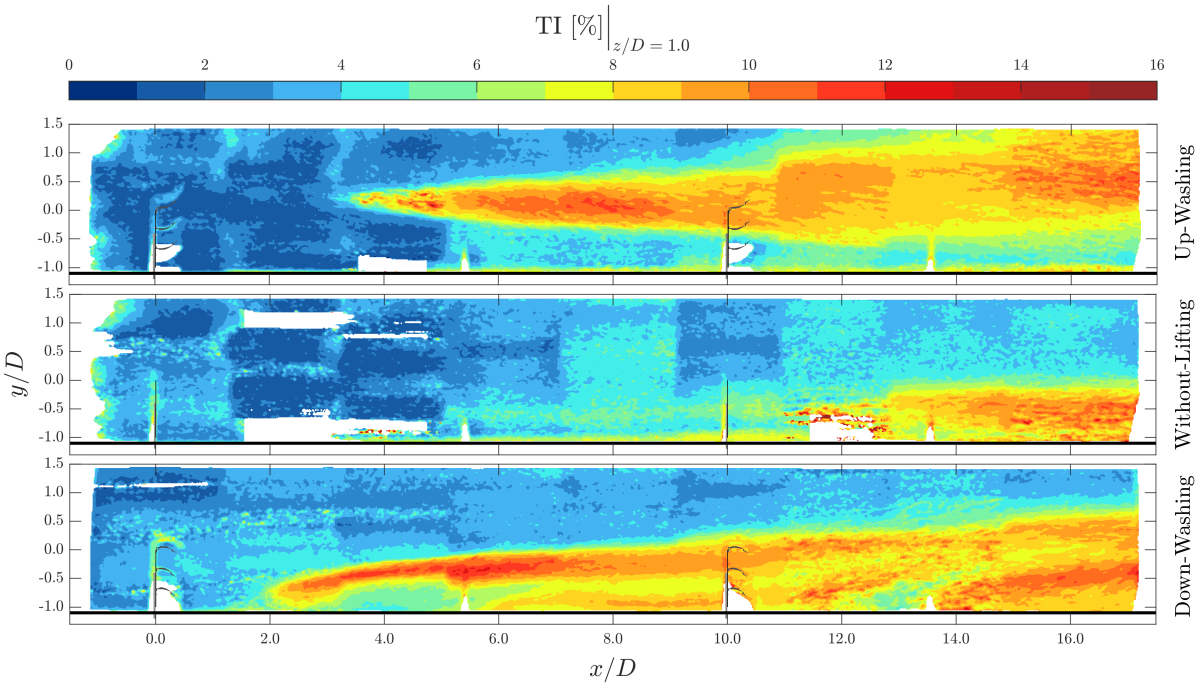

Figure 5.27: The turbulence intensity (TI) expressed as a percentage, evaluated at $z/D = 1.0$, is shown for cases with 10D inter-turbine spacing. The top plot corresponds to the (**U-10**) case, representing Up-Washing. The middle plot depicts the (**WL-10**) case, representing Without-Lifting, while the bottom plot illustrates the (**D-10**) case, representing Down-Washing. The corresponding MRSL configurations show this too. The black horizontal line in all plots indicates the floor of the regenerative wind farm.

In this cross-section, the Up-Washing case exhibits reduced turbulence intensity values compared to the 5D row spacing cases. Consequently, all three cases display similar trends to the 5D cases but with lower TI values. These results are logical, as the removal of one MRSL reduces blockage, leading to less turbulence being introduced into the flow.

5.3.5. Concluding Remarks on 10D Row Spacing Cases

In conclusion, the flow field data for the 10D row spacing cases demonstrate that increased inter-turbine spacing results in higher streamwise velocity values within the MRSL projection areas. The removal of one MRSL leads to reduced vertical velocity due to fewer lifting devices interacting with the flow, which also accounts for the lower turbulence intensity observed. The increased streamwise velocity is confirmed by load measurements, which show that the second row experiences higher thrust values compared to the second row in the 5D row spacing cases. However, as discussed extensively in subsection 2.2.1, wind farm yield encompasses more than just energy yield per turbine. The area in which energy is harvested is of great importance. Based on the load data, the 5D row spacing configuration delivers greater thrust within the same area. This is because the second and third MRSLs in the wake of the first, exhibit higher thrust values than the second MRSL in the 10D case. This underscores the fact that wind farm yield is a holistic metric, where the performance of individual turbines is less critical. In the pursuit of optimizing inter-turbine spacing, available power emerges as an important criterion. The results related to this measure are presented in the following section.

5.4. Available Power

Figure 5.28 shows the available power for six cases. These cases are Without-Lifting, Up-Washing, and Down-Washing for 5D and 10D spacing. The plot shows available power in the MRSL projection area as a function of the streamwise location in the regenerative wind farm. Available power is identified as $\frac{u^3}{u_\infty^3}$. The specific equation used can be seen in the y-label of Figure 5.28.

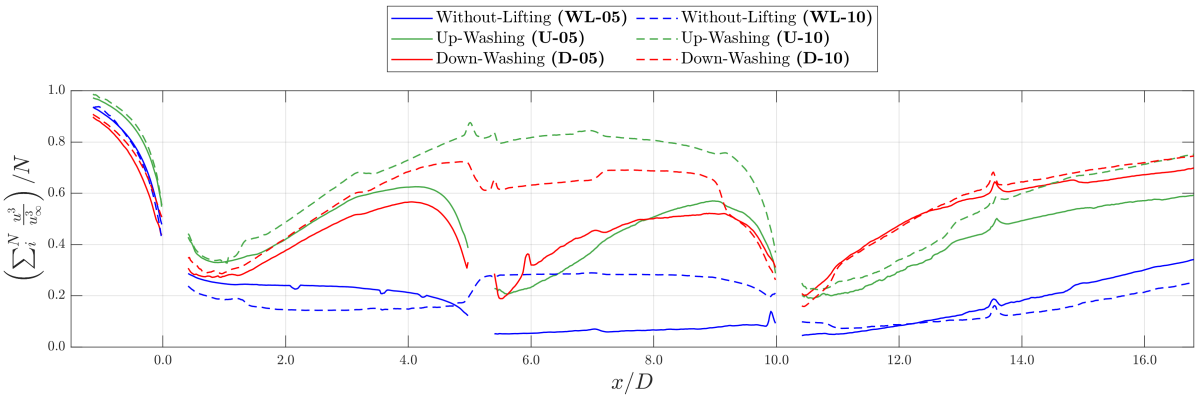

Figure 5.28: Available power for the cases Without-Lifting, Up-Washing, and Down-Washing for both 5D (solid lines) and 10D (dashed lines) row spacing. The MRSLs are positioned at $x/D = 0.0$ and $x/D = 10.0$ for the 10D cases with an additional MRSL at $x/D = 5.0$ for the 5D cases. The available power is calculated for the MRSL projection area of 300 by 300 mm.

From the figure, it is evident that differences already exist in the inflow conditions. At these negative x/D values, the Up-Washing variants exhibit more available power in the MRSL projection area compared to the Without-Lifting cases. Additionally, the Down-Washing variants show even lower available power up to the first MRSL. The principles of airfoil shapes and their method of generating lift explain this observed phenomenon. The suction side of an airfoil accelerates the flow to create a low-pressure region, while the pressure side slows the flow, producing a high-pressure region. The top airfoil of the MRSL is positioned directly above the MRSL area and, therefore, operates in undisturbed flow. For the Up-Washing cases, the suction side is positioned close to the MRSL area, accelerating the flow onto the actuator surface. Conversely, the Down-Washing configuration slows the flow onto the MRSL projection area because the pressure side is closest to the actuator surface. The Without-Lifting case does not experience these effects. This phenomenon is also observed in Figure 5.1 and Figure 5.2. Furthermore, this phenomenon is discussed in the work of Broertjes [43].

The available power decreases toward the first MRSL at $x/D = 0.0$ and continues to decline beyond this point. The available power for the Up-Washing and Down-Washing cases starts to increase at $x/D = 1.0$, marking the onset of wake recovery. From this point onward, the wake can be identified as the far wake, as discussed in subsection 2.1.1. The Without-Lifting case remains constant from here, showing no signs of wake recovery. The continuous decrease in available power downstream of the MRSL aligns with momentum theory, as flow speeds gradually decrease toward the MRSL and continue to slow until wake recovery begins [71].

In the far wake of the first turbine, the distinction between the Without-Lifting case and the other configurations becomes more pronounced with increasing downstream distance, up to $x/D = 4.2$ for cases with 5D inter-turbine spacing. At $x/D = 4.0$, the Up-Washing and Down-Washing cases exhibit nearly three times more available power compared to the Without-Lifting case, with the Up-Washing configuration performing slightly better for both 5D and 10D inter-turbine spacings.

From $x/D = 4.2$ to $x/D = 5.0$, the induction region for the second MRSL can be identified. In contrast, the 10D spacing cases further increase available power up to $x/D = 6.0$ from where the slope is close to zero until the induction region is identified at $x/D = 9.0$. This indicates that turbine spacing greater than 6 MRSL widths is not advantageous for harvesting more energy anymore.

For the 5D cases, the Up-Washing and Down-Washing configurations exhibit similar available power gradients in the far wake of the second MRSL compared to the far wake of the first MRSL. Furthermore, nearly identical available power values are achieved at four MRSL widths downstream of the second MRSL compared to the first MRSL. In contrast, the available power for the Without-Lifting case continues to decrease. This indicates a very low accumulation of power loss due to wake effects. Additionally, the 10D cases demonstrate that higher available power values can be achieved by increasing the inter-turbine spacing. Since the available power curves for the 10D cases approach a constant value, the optimal turbine spacing is likely less than 10 MRSL widths. This also enhances the capacity density of the wind farm (subsection 2.2.1).

The region behind the last MRSL at $x/D = 10.0$ is commonly referred to as the wind farm wake region. In this region, the Without-Lifting cases exhibit a linear increase in available power, whereas the Up-Washing and Down-Washing cases demonstrate a steeper linear increase, with higher rates of power recovery observed initially. Furthermore, the Down-Washing case shows larger values of available power compared with the Up-Washing cases, which is not seen in the wake of the previous MRSLs.

It is important to note that regions within the MRSL projection area with unavailable data can introduce unexpected jumps in the available power graph. Additionally, all 10D cases exhibit disturbances around $x/D = 5.0$. This location corresponds to the boundary between traverse positions 1 and 2, which may explain these irregularities, as the PTV setup was moved, and the regenerative wind farm was partially disassembled and reassembled. Despite these measurement inaccuracies, the overall trend of the graph indicates significant performance improvements for both Up-Washing and Down-Washing configurations.

5.5. Misaligned Case

This section presents the misaligned case, referred to as **U-05-MA**. For this configuration, the streamwise velocity, streamwise vorticity, and turbulence intensity are analyzed. Finally, a comparison of available power is conducted with the aligned Up-Washing case, known as **U-05**.

5.5.1. Streamwise Velocity

Four cross-section for the streamwise velocity are shown in Figure 5.29. The first cross-section is one MRSL width in front of the second MRSL.

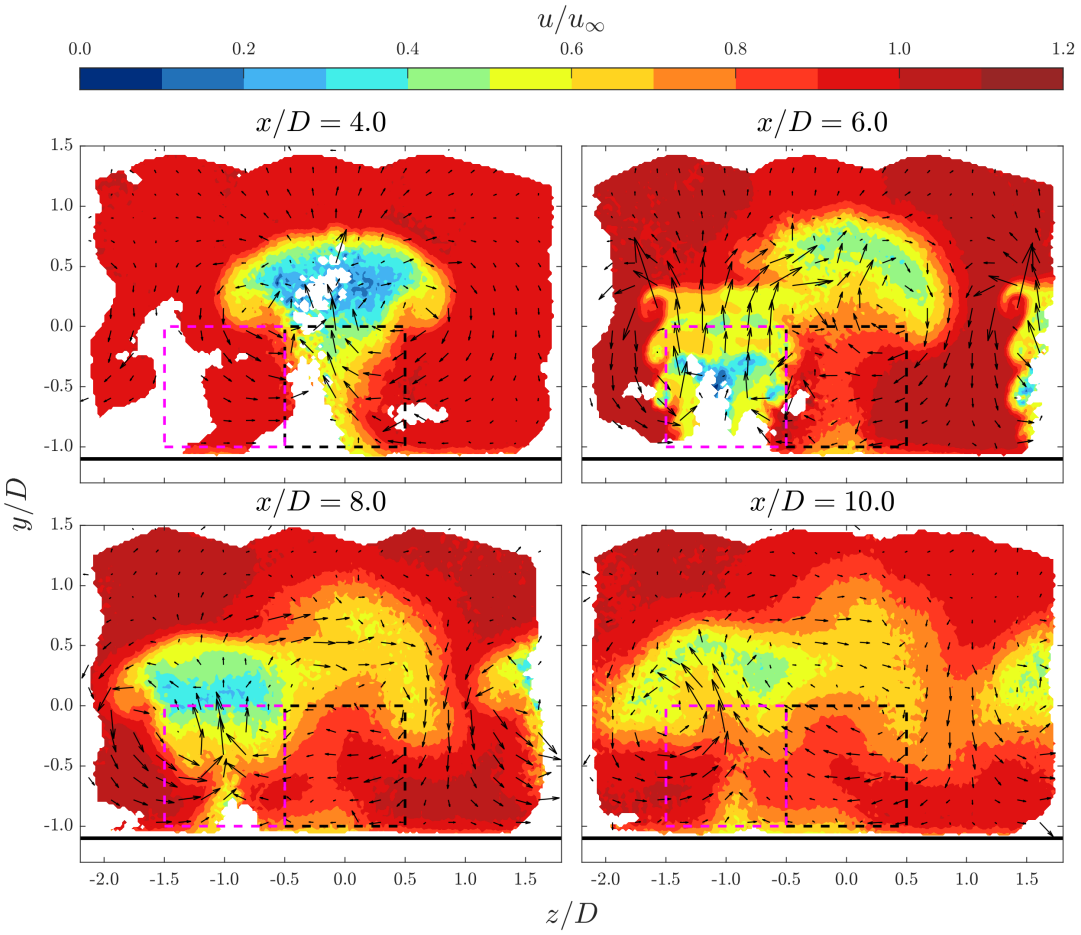

Figure 5.29: The streamwise velocity component, u, normalized by the freestream velocity, u_∞, is shown for the misaligned case with 5D inter-turbine spacing. The case is known as **U-05-MA**. Black dashed lines indicate the right MRSL projection area positioned at $x/D = 0.0$ while purple dashed lines indicate the left MRSL projection area. The purple MRSL is positioned downstream at $x/D = 5.0$. Solid black lines mark the floor while arrows depict the in-plane velocity.

The first cross-section at $x/D = 4.0$ reveals a wake shape similar to that shown in Figure 5.3. However, the wake region displays more pronounced blue hues, indicating lower momentum flow within the wake. The next cross-section at $x/D = 6.0$, located one MRSL width downstream of the second and misaligned rotor, presents a velocity field not observed previously. While the wake region within the projection area of the second MRSL remains similar, interaction with the wake region of the first MRSL is evident. Additionally, the wake of the MRSL in the first column of the wind farm can be identified. The subsequent cross-sections illustrate the progression of this combined wake region. Although the wake region exhibits less vertical displacement compared to the aligned case, the MRSL projection areas still maintain high-momentum flow in the far wake. Figure 5.30 provides the side views of this misaligned case.

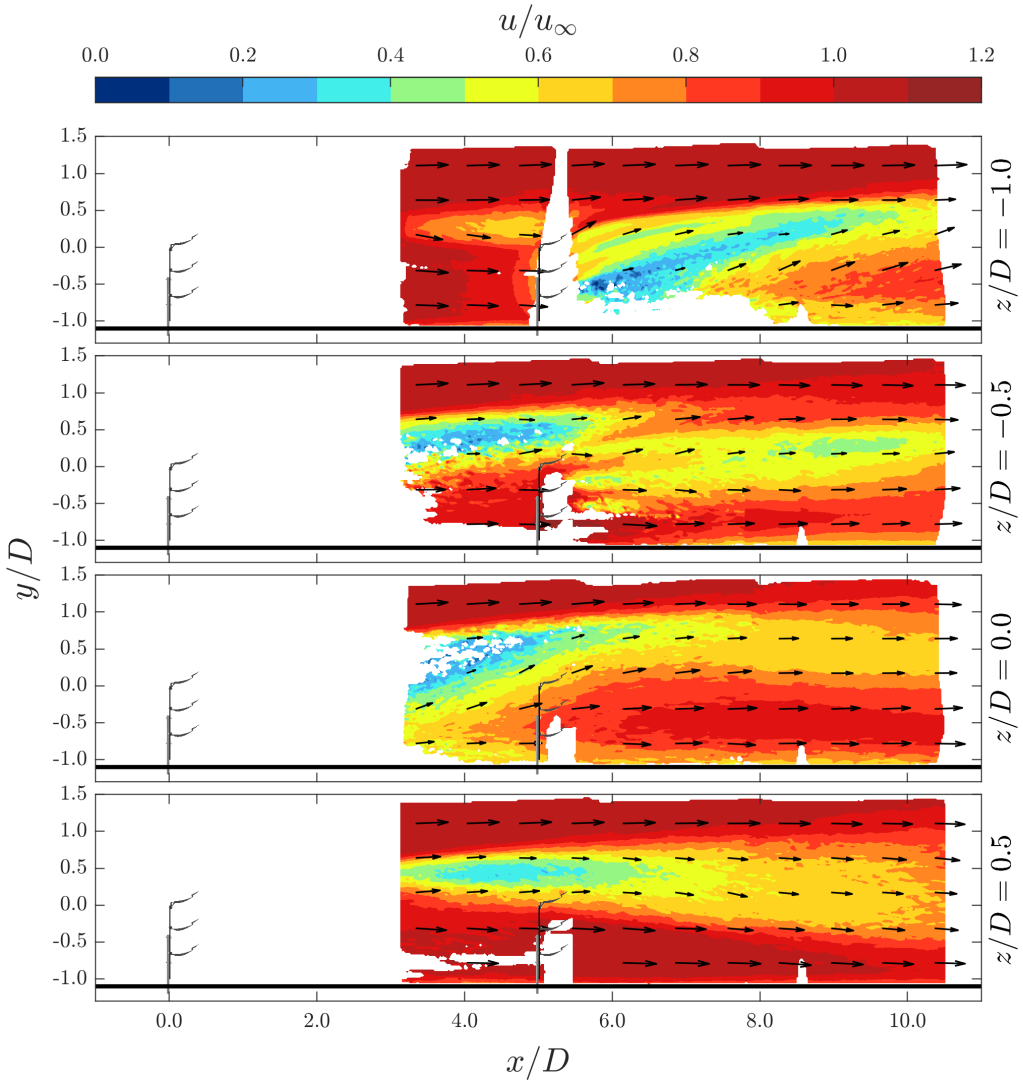

Figure 5.30: The streamwise velocity component, u, normalized by the freestream velocity, u_∞, is shown for the misaligned case with 5D inter-turbine spacing. Multiple side views are presented. The case is known as **U-05-MA**. Solid black lines mark the floor while arrows depict the in-plane velocity.

The cross-section at $z/D = 1.0$, which corresponds to the center of the second MRSL, clearly shows an upwash behind this MRSL as expected. Regarding the inflow on this turbine, the first MRSL does not exert a significant influence. Moving to the cross-section at $z/D = 0.5$, the center of both MRSLs, the wake region of the first MRSL becomes distinctly identifiable, while the wake of the second MRSL remains present. At $z/D = 0.0$, the center of the first MRSL is visible, highlighting the absence of a second upwash. Beyond $x/D = 5.0$, the wake region maintains a horizontal profile. In contrast, for the aligned case, the presence of a second upwash causes the wake region to reach significantly higher altitudes. The final cross-section, located at the edge of the first MRSL, shows a result similar to that of the aligned case as depicted in Figure 5.5. Here, the wake expands vertically in both directions. For a clearer comparison of the MRSL projection area, Figure 5.31 presents the streamwise velocity at four MRSL widths downstream of the second MRSL.

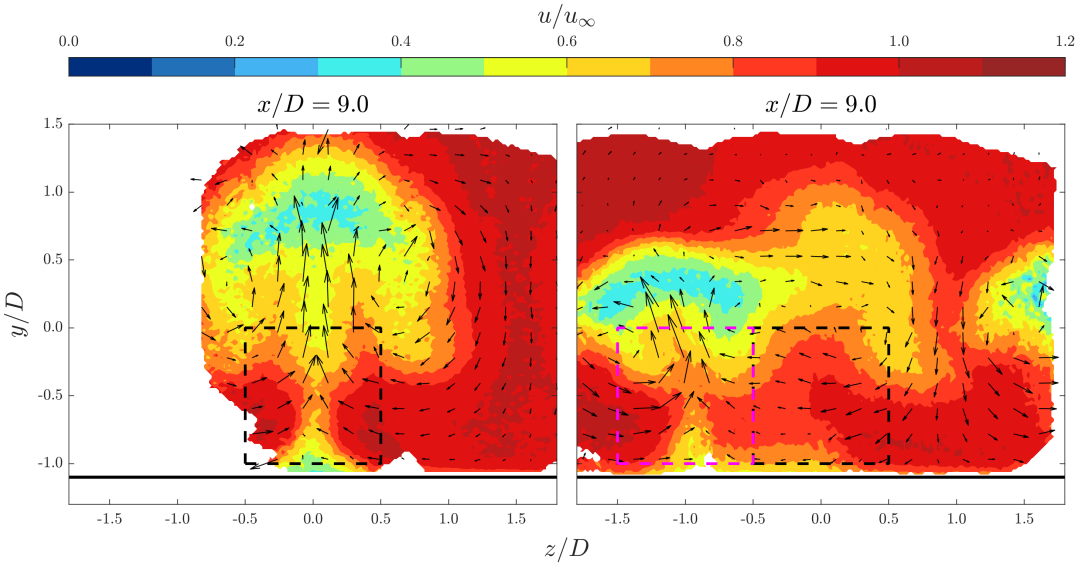

Figure 5.31: The streamwise velocity component, u, normalized by the freestream velocity, u_∞, is shown for the misaligned and regular cases with 5D inter-turbine spacing. The cases are known as **U-05** and **U-05-MA**. Black dashed lines indicate the right MRSL projection area positioned at $x/D = 0.0$ while purple dashed lines indicate the left MRSL projection area. The purple MRSL is positioned downstream at $x/D = 5.0$. Solid black lines mark the floor and arrows depict the in-plane velocity.

What stands out immediately is the elevated position of the wake region in the aligned case. This contrasts significantly with the misaligned case, which exhibits a lower and more widely spread wake region. Regarding the MRSL projection area, both cases show similar behavior, with high-momentum flow being entrained from the sides in both configurations. If a staggered layout were to be implemented, the next MRSL in the misaligned case would align with the right MRSL projection area. This area displays significantly higher streamwise velocity values compared to the left side. While multiple rows of a staggered layout were not tested, such a configuration could potentially yield even higher thrust values due to the increased inflow velocity. The next section explores the development of vortices to provide a more comprehensive understanding of the flow field.

5.5.2. Streamwise Vorticity

The streamwise vorticity is shown in Figure 5.32. The cross-sections are similar to those previously seen in the streamwise velocity.

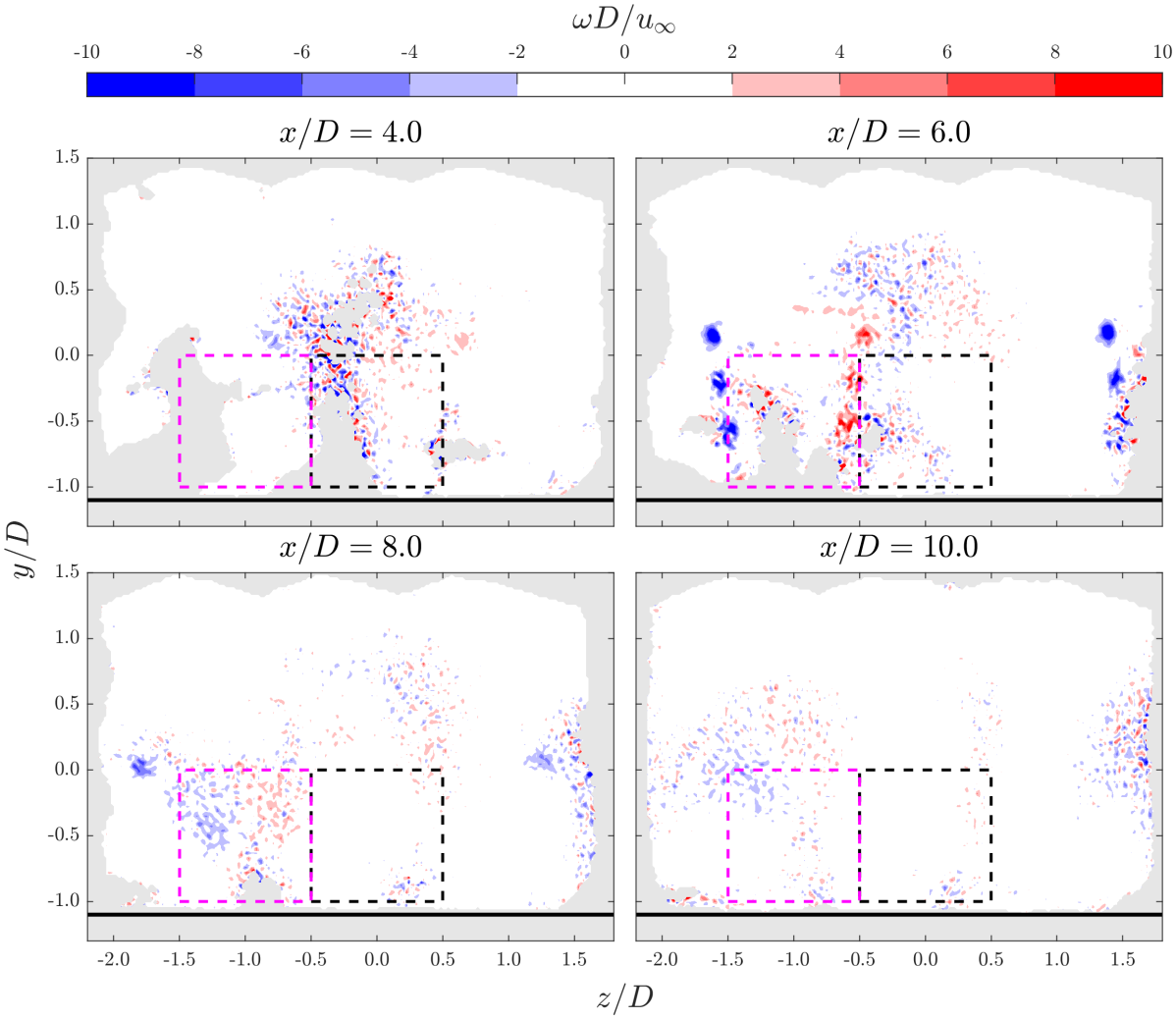

Figure 5.32: The streamwise vorticity, ω, normalized by multiplying with the rotor width D and dividing by the freestream velocity, u_∞, is shown for the misaligned case with 5D inter-turbine spacing. The case is known as **U-05-MA**. Black dashed lines indicate the right MRSL projection area positioned at $x/D = 0.0$ while purple dashed lines indicate the left MRSL projection area. The purple MRSL is positioned downstream at $x/D = 5.0$. Solid black lines mark the floor.

In the first cross-section at $x/D = 4.0$, a diffused vorticity field is observed. Only mild vorticity regions remain at the top right and left of the black MRSL projection area. In comparison, the previously reviewed **U-05** case shown in Figure 5.10 for the same cross-section exhibits more pronounced vorticity regions and less diffusion. The reason for this is the quite significant data gaps, in the misaligned data. These gaps cause edge effects along their boundaries, leading to a reduction in data quality. One MRSL width downstream of the second MRSL, indicated in purple, 6 distinct vortex cores are visible. Additionally, the vortex cores of the second MRSL are visible in the first column, highlighting the periodicity of the velocity field. The final two cross-sections show significantly diffused vorticity fields, where the vorticity eventually dissipates. Figure 5.33 shows a near wake comparison with the aligned 5D case.

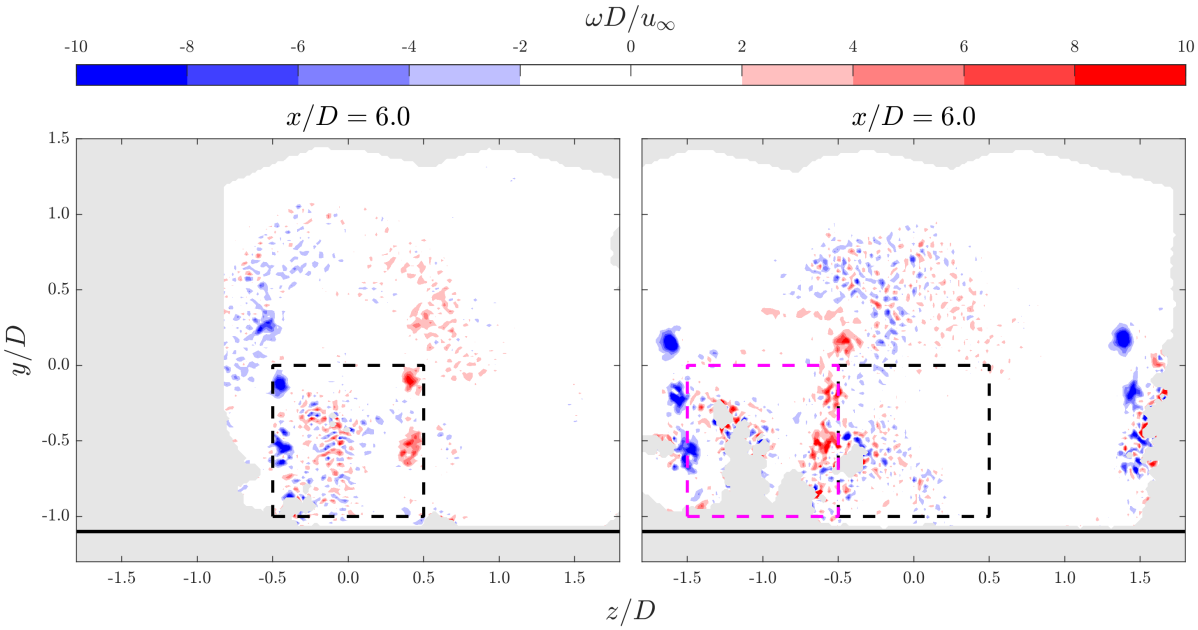

Figure 5.33: The streamwise vorticity, ω, normalized by multiplying with the rotor width D and dividing by the freestream velocity, u_∞, is shown for the misaligned and regular cases with 5D inter-turbine spacing. The cases are known as **U-05** and **U-05-MA**. Black dashed lines indicate the right MRSL projection area positioned at $x/D = 0.0$ while purple dashed lines indicate the left MRSL projection area. The purple MRSL is positioned downstream at $x/D = 5.0$. Solid black lines mark the floor.

The comparison shows more pronounced blue vortex cores in the misaligned case. The strength approaches the vortex cores at $x/D = 1.0$ in Figure 5.10. This is because of the relatively clean inflow on the left side of the purple MRSL projection area. The right side of the purple MRSL projection area suffers from disturbed inflow conditions which results in reduced strength of the red vortex cores.

5.5.3. Turbulence Intensity

The same four cross-sections now present the turbulence intensity in the misaligned case. The results are shown in Figure 5.34.

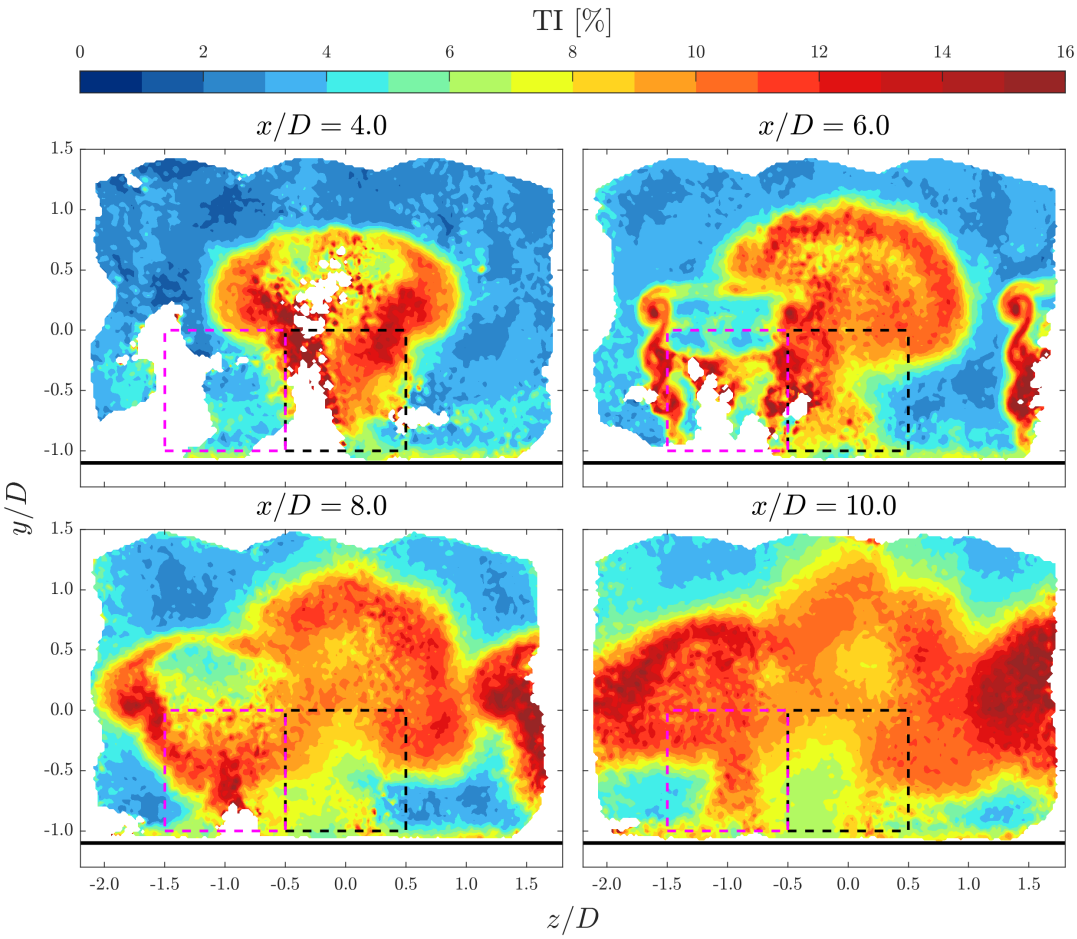

Figure 5.34: The turbulence intensity (TI), is shown for the misaligned case with 5D inter-turbine spacing. The case is known as **U-05-MA**. Black dashed lines indicate the right MRSL projection area positioned at $x/D = 0.0$ while purple dashed lines indicate the left MRSL projection area. The purple MRSL is positioned downstream at $x/D = 5.0$. Solid black lines mark the floor.

The first cross-section resembles the corresponding cross-section in Figure 5.12 in terms of shape. However, the overall turbulence intensity (TI) values are noticeably higher. The inflow conditions for the second MRSL maintain low turbulence levels. In the cross-sections at $x/D = 6.0$ and $x/D = 8.0$, the two MRSLs remain distinguishable. The right region displays homogeneous TI values, while the left region highlights the vortex structure created by the top wings. In the final cross-section, an extensive high-TI region is observed. There is a visible connection to the first column, suggesting that, at five MRSL widths downstream, the entire wind farm row forms a unified region of elevated TI values. Before discussing the MRSL projection area, side views are presented in Figure 5.35.

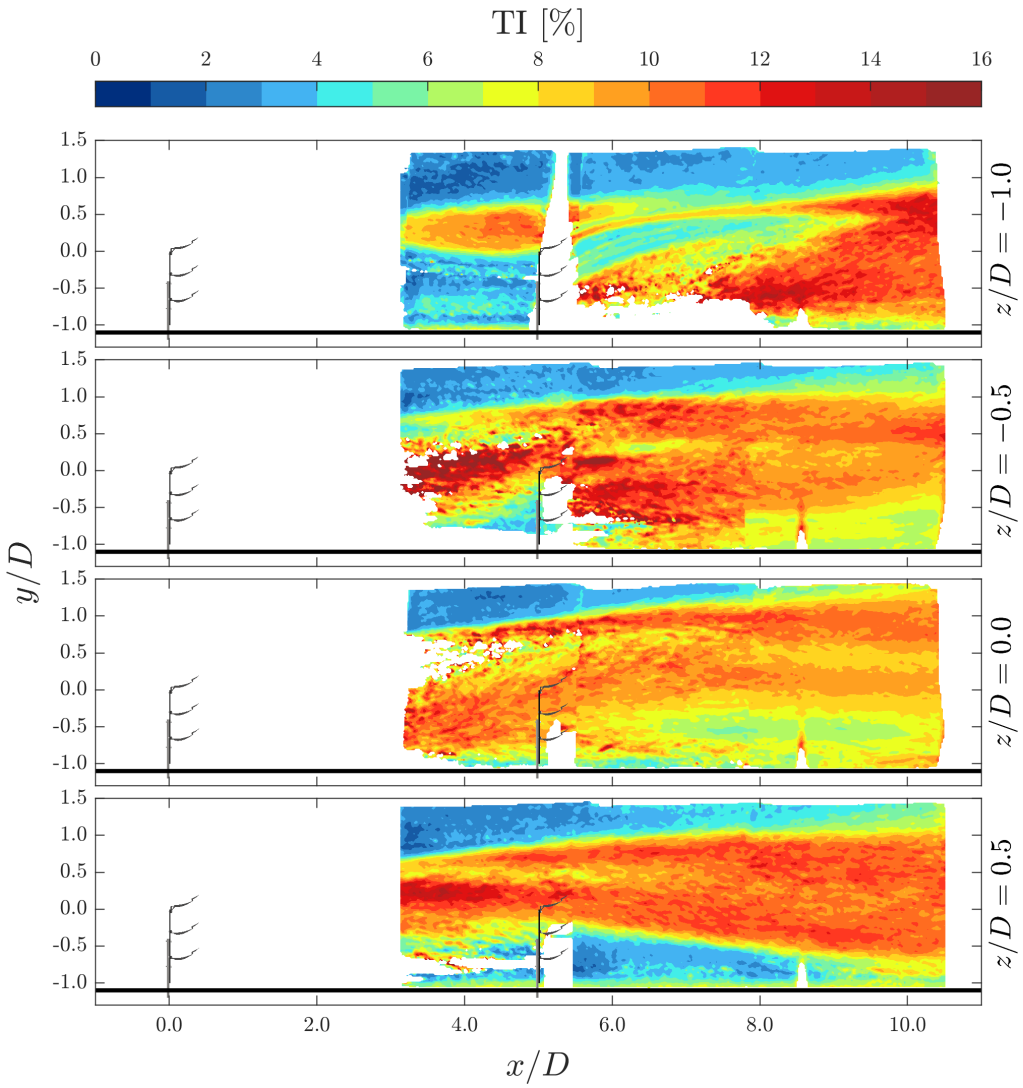

Figure 5.35: The turbulence intensity (TI) is shown for the misaligned case with 5D inter-turbine spacing. Multiple side views are presented. The case is known as **U-05-MA**. Solid black lines mark the floor.

The first cross-section reveals an upper turbulent region that remains above the second MRSL. In the wake of the second MRSL, a reduction in turbulence intensity (TI) induced by the top two wings is evident. In contrast, the bottom three cross-sections display extensive regions of high TI. For a detailed comparison, Figure 5.36 illustrates the MRSL projection area four MRSL widths downstream of the second MRSL.

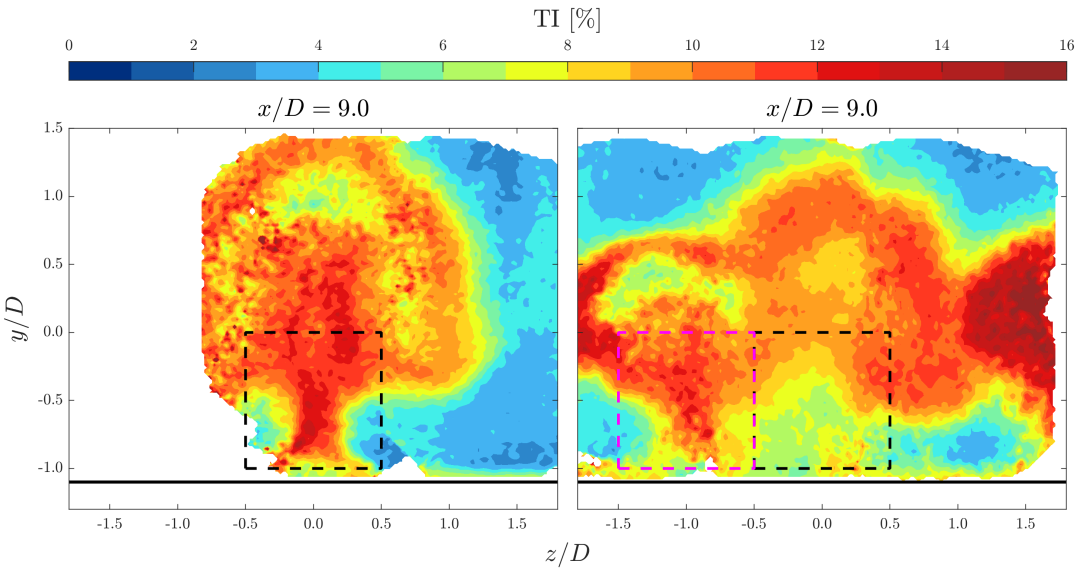

Figure 5.36: The turbulence intensity (TI) is shown for the misaligned and regular cases with 5D inter-turbine spacing. The cases are known as **U-05** and **U-05-MA**. Black dashed lines indicate the right MRSL projection area positioned at $x/D = 0.0$ while purple dashed lines indicate the left MRSL projection area. The purple MRSL is positioned downstream at $x/D = 5.0$. Solid black lines mark the floor.

The turbulence intensity extends to greater heights in the aligned case. In the misaligned case, the MRSL projection area on the left exhibits slightly lower values compared to the aligned case. If the next MRSL is positioned in a staggered configuration, the right MRSL projection area presents the inflow condition, which displays significantly reduced TI.

5.5.4. Available Power Comparison

Figure 5.37 shows the available power for the misaligned case and compares it with the aligned 5D cases Up-Washing and Without-Lifting. For the misaligned case, each MRSL projection area is shown.

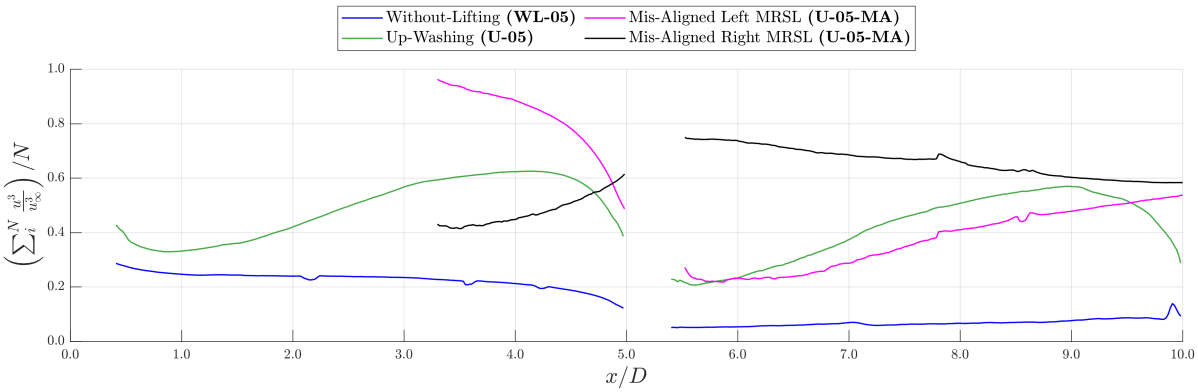

Figure 5.37: Available power for the cases Without-Lifting (**WL-05**), Up-Washing (**U-05**) and both MRSL projection areas of the misaligned case (**U-05-MA**). The MRSLs are positioned at $x/D = 0.0$ and $x/D = 5.0$. The available power is calculated for the MRSL projection area of 300 by 300 mm.

A notable observation is the reduced available power for the black line compared to the green line upstream of $x/D = 4.5$. Given that this occurs in the wake of the first MRSL and the configuration is similar, a comparable recovery would be expected. However, the reduced recovery in the misaligned case is attributed to data gaps around $x/D = 4.0$, as shown in Figure 5.29. These data gaps result in the black line indicating less available power compared to the green line, as high inflow velocities are not accounted for due to the missing data, thereby lowering the average

value. Downstream of $x/D = 9.0$, the green line goes down, this is due to the fact that another MRSL is placed at $x/D = 10.0$. It should be noted that this is not the case for the purple and black lines.

Examining the inflow conditions for the left MRSL in the misaligned case, high available power values are observed. This would ultimately result in higher rotor thrust values for the misaligned case compared to the Aligned case. Investigating the wake of the second row reveals that the right MRSL projection area in the misaligned case exhibits high available power values in the near wake. However, these values decrease downstream as the wake region expands and occupies a larger portion of the MRSL projection area. The substantial available power values for the black line in the near wake suggest that a staggered layout with even closer inter-turbine spacing could yield higher power output per unit area. However, experiments or CFD simulations involving multiple rows in a staggered layout should be conducted to validate this. Additionally, it is noted that the available power values in the misaligned case tend to approach the aligned up-washing values in the far wake of the second MRSL. This could mean that the benefits of a staggered layout are only beneficial for the first rows in the wind farm. However, this requires MRSL wind farm research with more rows.

6

Conclusion and Recommendations

The final chapter of this report provides a conclusion based on the research conducted. This is achieved by revisiting and answering the research questions. Additionally, the recommendations section discusses various research projects that could build on this work.

6.1. Conclusion

Offshore wind energy is currently facing challenges due to rising costs, with wind farm wake losses significantly contributing to these financial pressures. In exploring potential solutions, research into the theory of wind farms revealed that traditional methods, such as wind farm layout optimization and rotor yawing or tilting, are insufficient to address the issue fully. However, vertical forcing using lifting devices introduced the concept of regenerative wind farming. This innovative approach shows significant potential to enhance wind farm efficiency and reinforce the competitive advantage of offshore wind energy. This work focuses on conducting a scaled wind farm experiment in the OJF to assess the regenerative wind farming concept. This research builds upon the work of Broertjes [43], which examined the near-wake of an isolated system with lifting devices. Instead of focusing solely on the aerodynamics of an isolated system, this study investigates a cluster of nine energy-harvesting systems arranged in a 3 x 3 configuration. This setup allows for the exploration of lifting device applications within a wind farm while also enabling the analysis of the far wake due to the expansion to nine systems. To highlight the main results of the regenerative wind farm experiment, the research questions formulated in subsection 2.5.3 are presented and answered.

- **To what extent can wind farm efficiency be improved by increasing vertical energy entrainment using lifting devices?**

  The research demonstrates significant improvements in wind farm efficiency, highlighting great potential for reducing inter-turbine spacing while harvesting more energy. This regenerative wind farm concept ensures a substantially higher power output per unit surface area compared to traditional wind farms. Although power outputs cannot be measured directly when porous disks are used, the conclusions are based on quantitative data, such as load data, streamwise velocity measurements, and available power. The factors driving this enhanced efficiency are elaborated in detail in the following sub-questions.

  1. **What are the flow field characteristics of the wind farm with and without lifting devices configured?**

     The vertical advection generated by the wings, induced by the trailing vortices, significantly magnified the vertical entrainment process.
     In the Up-Washing case, the centers of these trailing vortices extend up to twice the MRSL height, effectively capturing high-momentum flow from above the wind farm

and redirecting it into the farm. This was confirmed by vertical velocity data, which showed an upwash occurring behind and above the MRSL projection area, accompanied by a downwash region on the sides of the MRSL projection area. This flow pattern facilitates the entrainment of high-momentum flow into the MRSL projection area from the sides.
In the Down-Washing case, the core of the trailing vortices remains at half the MRSL height but is positioned farther outboard of the MRSL projection area. Although the vortex center is lower, the presence of the floor enhances the strength of the circulation, ensuring effective capture of high-momentum flow. A large downwash region forms directly behind the MRSL projection area, facilitating the entrainment of high-momentum flow from the upper layers straight into the wind farm. Simultaneously, the wake is pushed outward to the sides of the MRSL projection area, creating an upwash between MRSL columns.
In contrast, the Without-Lifting case showed no vertical velocity or circulation regions induced by vorticity as the trailing vortices are absent. Instead, the actuator surfaces in the flow, without the presence of lifting devices, led to higher turbulence intensity in the exit region of both the 5D and 10D row-spacing wind farms. This indicates that the addition of lifting devices reduces turbulence intensity, resulting in more favorable inflow conditions for downstream turbines.

2. **What are the relative wind speeds inside the MRSL projection area and the vertical wind speeds in the wind farm, both with and without the lifting devices installed?**

   Wind speeds within the MRSL projection areas were investigated at a distance of one MRSL width upstream of the next MRSL. The results revealed extensive regions with at least 80% of the freestream velocity inside the MRSL projection areas for both the Up-Washing and Down-Washing cases. In contrast, the Without-Lifting case exhibited relative streamwise velocities ranging from only 20% to 60%. This finding also applies to the 10D row spacing cases, with the distinction that the Up-Washing and Down-Washing cases exhibited notably larger regions of 80% freestream velocity.
   To evaluate the interaction with high-momentum flow in the upper layers above the wind farm, vertical velocity was analyzed. The results indicated that the Up-Washing and Down-Washing cases generate vertical velocity values up to half the freestream velocity, whereas the Without-Lifting cases produce almost no vertical velocity, demonstrating minimal interaction with flow in the upper layers which carry higher momentum flow.

3. **What are the thrust values and the available power for the downstream turbines in the center column of the wind farm with and without lifting devices configured?**

   The normalized rotor thrust for the second MRSL is more than three times higher compared to the Without-Lifting configuration. For the third row, the Up-Washing configuration achieves a rotor thrust that is four times higher, while the Down-Washing configuration maintains more than three times the rotor thrust of the baseline configuration. In the second row of the 10D spacing case, rotor thrust is 2.5 times higher for the Down-Washing configuration and three times higher for the Up-Washing configuration, compared to the Without-Lifting case.
   Regarding available power, similar increases in performance are observed for both the Up-Washing and Down-Washing cases. The available power for each MRSL, measured at four MRSL widths downstream, is approximately three times higher. For the 10D row spacing case, the available power stabilizes after six MRSL widths downstream. It is worth noting that harvested power increases by more than five times when thrust forces are tripled. This is due to the relationship between power and thrust.

4. **To what extent is there an interaction, between the lifting devices and the porous disk it is attached to?**

   The thrust force on the MRSL is affected by the generation of lift, as this process in-

volves the acceleration of flow on the suction side of the airfoil. This effect was evident in the load measurements. In clean flow, the Down-Washing configuration exhibited 87% of the thrust force of the MRSL without lifting devices, whereas the Up-Washing configuration demonstrated 106% of the thrust force of the MRSL without lifting devices. These results indicate that the lifting devices in the Up-Washing configuration increase thrust on the porous disk it is attached to, while the lifting devices in the Down-Washing configuration reduce thrust on the porous disk it is attached to.

With the research questions addressed, the regenerative wind farm concept is one step closer to demonstrating its significant value for future wind farms. Based on the results, it can be concluded that lifting devices significantly enhance wind farm efficiency. Both Multi-Rotor Systems and single-rotor wind turbines benefit from the application of lifting devices. While Multi-Rotor Systems gain advantages from integrating lifting devices into their supporting structures, this does not diminish the potential benefits of applying lifting devices to single-rotor turbines. On the contrary, lifting devices could improve the performance of existing wind farms, making the concept more broadly applicable by allowing current wind farms to benefit from it. This would also contribute to acquiring further knowledge for developing the wind farms of the future. Looking at the broader picture, the potential increase in wind energy capacity offered by this concept could significantly boost green hydrogen production, particularly when electricity demands are met. This would ensure that industries unable to fully rely on electricity can transition to fossil fuel-free energy by using a reliable supply of green hydrogen.

The concept of regenerative wind farming, along with the findings of this thesis, fundamentally alters the aerodynamics of wind farms. This opens up a completely new area of research. Future research projects are therefore explored in the following section.

6.2. Recommendations

Whereas this thesis has proven the potential of boosting wind farm performance by introducing lifting devices, real-world applications require extensive research into the topic. To implement the innovative concept of regenerative wind farming using lifting devices in real-world wind farm design, numerous additional variables must be considered. These variables should encompass aspects of meteorology and wind farm design. Investigating these variables will provide insights into the effectiveness of the concept.

From an aerodynamic perspective, one crucial variable to consider is the inclusion of an atmospheric boundary layer. This thesis utilized a floor where only a thin boundary layer developed, which does not accurately represent a real-world wind shear profile. Therefore, incorporating an ABL is an important area for future research. Additionally, wind tunnels typically ensure very low turbulence inflow conditions. CFD simulations can perform turbulence intensity tests to replicate the effects of wind gusts, ensuring that the concept is tested under conditions more representative of real-world applications.

Further in-depth research into the MRSL is also needed. Optimizing the device will help achieve even higher power outputs per unit area for wind farms. This will primarily involve refining the positioning of the wings in relation to the rotors and conducting more detailed research into the performance of the lifting devices when rotating energy harvesting devices are present. Additionally, exploring wing shape presents another important area for investigation.

In terms of wind farm design, the misalignment of MRSLs requires further investigation. Preliminary tests discussed in this thesis suggest the concept remains effective under misalignment, but more detailed research is needed. For example, load measurements were not conducted for the misalignment case, and a case without lifting devices was not performed as a benchmark. Additionally, the effect of multiple misalignment rows could be investigated. Moreover, investigating the fully developed wind farm region would necessitate adding extra rows of turbines, which requires either a reduction in MRSL size or the use of a larger wind tunnel. Finally, the aerodynamic effects of turbine yawing should be explored. Airfoil effectiveness and perceived

pitch angle change when the inflow angle changes laterally, making this an important factor to investigate [31].

Beyond these considerations of aerodynamics, MRSL, and wind farm design, structural research into the framework is also essential. While less directly related to aerodynamics and more to structural engineering, the significant forces generated by the lifting devices underscore the importance of this research area. For example, integrating the wings as a structural component of the MRS frame would enhance its value in a more versatile way.

Finally, it is important to note that these potential research topics interconnect. For example, what is the effect of the ABL on the position of the wings or what is the effect of wind gusts and the accompanied lift increase by the wings on the support structure?

References

[1] R. Williams and F. Zhao. Global Offshore Wind Report 2024. Tech. rep. Report by Global Wind Energy Council, 2024.

[2] J.N. Sørensen and G.C. Larsen. "A Minimalistic Prediction Model to Determine Energy Production and Costs of Offshore Wind Farms". In: Energies 14.2 (2021). ISSN: 1996-1073. DOI: 10.3390/en14020448. URL: https://www.mdpi.com/1996-1073/14/2/448.

[3] T. Macquart, D. Kucukbahar, and B. Prinsen. Dutch Offshore Wind Market Report 2023. Tech. rep. Netherlands Enterprise Agency, 2023.

[4] A turning point for offshore wind, global opportunities and risk trends. Tech. rep. Allianz Commercial, 2023.

[5] R. Barthelmie et al. "Quantifying the Impact of Wind Turbine Wakes on Power Output at Offshore Wind Farms". In: Journal of Atmospheric and Oceanic Technology - J ATMOS OCEAN TECHNOL 27 (Aug. 2010), pp. 1302–1317. DOI: 10.1175/2010JTECHA1398.1.

[6] P. Jamieson. Innovation in Wind Turbine Design. John Wiley & Sons, Ltd, 2011. ISBN: 978111997-5441. DOI: https://doi.org/10.1002/9781119975441.ch. URL: https://onlinelibrary.wiley.com/doi/abs/10.1002/9781119975441.ch.

[7] C.J. Simão Ferreira et al. "Enhancing Wind Farm Efficiency Through Active Control of the Atmospheric Boundary Layer's Vertical Entrainment of Momentum". In: Journal of Physics: Conference Series 2767.9 (2024), p. 092107. DOI: 10.1088/1742-6596/2767/9/092107. URL: https://dx.doi.org/10.1088/1742-6596/2767/9/092107.

[8] P. Chatelain et al. "Vortex particle-mesh methods with immersed lifting lines applied to the Large Eddy Simulation of wind turbine wakes". In: Jan. 2011.

[9] L.J. Vermeer, J.N. Sørensen, and A. Crespo. "Wind turbine wake aerodynamics". In: Progress in Aerospace Sciences 39.6 (2003), pp. 467–510. ISSN: 0376-0421. DOI: https://doi.org/10.1016/S0376-0421(03)00078-2. URL: https://www.sciencedirect.com/science/article/pii/S0376042103000782.

[10] F. Porté-Agel, M. Bastankhah, and S. Shamsoddin. "Wind-Turbine and Wind-Farm Flows: A Review". In: Boundary-Layer Meteorology 174 (Jan. 2020). DOI: 10.1007/s10546-019-00473-0.

[11] G.C. Larsen et al. "Wake meandering: a pragmatic approach". In: Wind Energy 11.4 (2008), pp. 377–395. DOI: https://doi.org/10.1002/we.267. URL: https://onlinelibrary.wiley.com/doi/abs/10.1002/we.267.

[12] J. Michalakes M.J. Churchfield S. Lee and P.J. Moriarty. "A numerical study of the effects of atmospheric and wake turbulence on wind turbine dynamics". In: Journal of Turbulence 13 (2012), N14. DOI: 10.1080/14685248.2012.668191. URL: https://doi.org/10.1080/14685248.2012.668191.

[13] L.E.M Lignarolo. "On the turbulent mixing in horizontal axis wind turbine wakes". English. Dissertation (TU Delft). Delft University of Technology, 2016. ISBN: 978-94-028-0099-9. DOI: 10.4233/uuid:057fa33f-82a3-4139-beb8-53f184cd1d57.

[14] Y. Wu and F. Porté-Agel. "Large-Eddy Simulation of Wind-Turbine Wakes: Evaluation of Turbine Parametrisations". In: Boundary-Layer Meteorology 138 (Mar. 2011). DOI: 10.1007/s10546-010-9569-x.

[15] S.J. Andersen, J. N. Sørensen, and R. Mikkelsen. "Simulation of the inherent turbulence and wake interaction inside an infinitely long row of wind turbines". In: Journal of Turbulence 14.4 (2013), pp. 1–24. DOI: 10.1080/14685248.2013.796085. URL: https://doi.org/10.1080/14685248.2013.796085.

[16] L.E.M Lignarolo et al. "Experimental analysis of the wake of a horizontal-axis wind-turbine model". In: Renewable Energy 70 (2014), pp. 31–46. DOI: https://doi.org/10.1016/j.renene.2014.01.020.

[17] S. Andersen, J. Sørensen, and R. Mikkelsen. "Simulation of the inherent turbulence and wake interaction inside an infinitely long row of wind turbines". In: Journal of Turbulence 14 (Apr. 2013), pp. 1–24. DOI: 10.1080/14685248.2013.796085.

[18] Ministerie van Economische Zaken en Klimaat. Nationaal Plan Energiesysteem. Tech. rep. 2023.

[19] I. Troen and E. Lundtang Petersen. European Wind Atlas. English. Risø National Laboratory, 1989. ISBN: 87-550-1482-8.

[20] E. Dupont, R. Koppelaar, and H. Jeanmart. "Global available wind energy with physical and energy return on investment constraints". In: Applied Energy 209 (Oct. 2017). DOI: 10.1016/j.apenergy.2017.09.085.

[21] S.H. Bader, V. Inguva, and J. Perot. "Improving the efficiency of wind farms via wake manipulation". In: Wind Energy 21 (July 2018). DOI: 10.1002/we.2226.

[22] B.H. Bulder and E.T.G. Bot. Quick scan of energy production and wake losses of the Borssele Wind Farm Zone including losses for nearby Belgian Wind Farms. Tech. rep. ECN, 2015.

[23] K.L. Wu and F. Porté-Agel. "Flow adjustment inside and around large finite-size wind farms". In: Energies 10.12 (2017), p. 2164.

[24] R. Stull. Practical Meteorology: An Algebra-based Survey of Atmospheric Science. BC Open Textbook Collection. AVP International, University of British Columbia, 2016. ISBN: 9780888651761. URL: https://books.google.nl/books?id=xP2sDAEACAAJ.

[25] S. Frandsen. "On the wind speed reduction in the center of large clusters of wind turbines". In: Journal of Wind Engineering and Industrial Aerodynamics 39.1 (1992), pp. 251–265. ISSN: 0167-6105. DOI: https://doi.org/10.1016/0167-6105(92)90551-K. URL: https://www.sciencedirect.com/science/article/pii/016761059290551K.

[26] M. Calaf, C. Meneveau, and J. Meyers. "Large eddy simulations of fully developed wind-turbine array boundary layers". In: Physics of Fluids 22 (Jan. 2010). DOI: 10.1063/1.3291077.

[27] M. Abkar and F. Porté-Agel. "The Effect of Free-Atmosphere Stratification on Boundary-Layer Flow and Power Output from Very Large Wind Farms". In: Energies 6.5 (2013), pp. 2338–2361. ISSN: 1996-1073. DOI: 10.3390/en6052338. URL: https://www.mdpi.com/1996-1073/6/5/2338.

[28] R.J.A.M. Stevens and C. Meneveau. "Flow structure and turbulence in wind farms". In: Annual review of fluid mechanics 49.1 (2017), pp. 311–339.

[29] J. Meyers and C. Meneveau. "Flow visualization using momentum and energy transport tubes and applications to turbulent flow in wind farms". In: Journal of Fluid Mechanics 715 (2013), pp. 335–358. DOI: 10.1017/jfm.2012.523.

[30] M. Abkar and F. Porté-Agel. "Mean and turbulent kinetic energy budgets inside and above very large wind farms under conventionally-neutral condition". In: Renewable Energy 70 (2014). Special issue on aerodynamics of offshore wind energy systems and wakes, pp. 142–152. ISSN: 0960-1481. DOI: https://doi.org/10.1016/j.renene.2014.03.050. URL: https://www.sciencedirect.com/science/article/pii/S0960148114002146.

[31] J.D. Anderson. Fundamentals of Aerodynamics. McGraw-Hill series in aeronautical and aerospace engineering. McGraw-Hill Education, 2017. ISBN: 9781259251344. URL: https://books.google.nl/books?id=_7VLjwEACAAJ.

[32] J. Annoni et al. "Analysis of axial-induction-based wind plant control using an engineering and a high-order wind plant model". In: Wind Energy 19.6 (2016), pp. 1135–1150. DOI: https://doi.org/10.1002/we.1891. URL: https://onlinelibrary.wiley.com/doi/abs/10.1002/we.1891.

[33] T. Knudsen, T. Bak, and M. Svenstrup. "Survey of wind farm control—power and fatigue optimization". In: Wind Energy 18.8 (2015), pp. 1333–1351. DOI: https://doi.org/10.1002/we.1760. URL: https://onlinelibrary.wiley.com/doi/abs/10.1002/we.1760.

[34] P.M.O. Gebraad and J.W. van Wingerden. "Maximum power-point tracking control for wind farms". In: Wind Energy 18.3 (2015), pp. 429–447. DOI: https://doi.org/10.1002/we.1706. URL: https://onlinelibrary.wiley.com/doi/abs/10.1002/we.1706.

[35] F. Porté-Agel, Y. Wu, and C. Chen. "A Numerical Study of the Effects of Wind Direction on Turbine Wakes and Power Losses in a Large Wind Farm". In: Energies 6.10 (2013), pp. 5297–5313. DOI: 10.3390/en6105297. URL: https://www.mdpi.com/1996-1073/6/10/5297.

[36] Y. Wu and F. Porté-Agel. "Modeling turbine wakes and power losses within a wind farm using LES: An application to the Horns Rev offshore wind farm". In: Renewable Energy 75 (Mar. 2015), pp. 945–955. DOI: 10.1016/j.renene.2014.06.019.

[37] C.L. Archer, S. Mirzaeisefat, and S. Lee. "Quantifying the sensitivity of wind farm performance to array layout options using large-eddy simulation". In: Geophysical Research Letters 40.18 (2013), pp. 4963–4970. DOI: https://doi.org/10.1002/grl.50911. URL: https://agupubs.onlinelibrary.wiley.com/doi/abs/10.1002/grl.50911.

[38] N. Hamilton, M. Melius, and R.B. Cal. "Wind turbine boundary layer arrays for Cartesian and staggered configurations-Part I, flow field and power measurements". In: Wind Energy 18.2 (2015), pp. 277–295. DOI: https://doi.org/10.1002/we.1697. URL: https://onlinelibrary.wiley.com/doi/abs/10.1002/we.1697.

[39] C.L. Archer and A. Vasel-Be-Hagh. "Wake steering via yaw control in multi-turbine wind farms: Recommendations based on large-eddy simulation". In: Sustainable Energy Technologies and Assessments 33 (2019), pp. 34–43. ISSN: 2213-1388. DOI: https://doi.org/10.1016/j.seta.2019.03.002. URL: https://www.sciencedirect.com/science/article/pii/S2213138818306544.

[40] M.F. Howland et al. "Wake structure in actuator disk models of wind turbines in yaw under uniform inflow conditions". In: Journal of Renewable and Sustainable Energy 8.4 (July 2016), p. 043301. ISSN: 1941-7012. DOI: 10.1063/1.4955091. URL: https://doi.org/10.1063/1.4955091.

[41] J.J. Cutler et al. "Optimization of Turbine Tilt in a Wind Farm". In: AIAA Scitech 2021 Forum. 2021. DOI: 10.2514/6.2021-1180. eprint: https://arc.aiaa.org/doi/pdf/10.2514/6.2021-1180. URL: https://arc.aiaa.org/doi/abs/10.2514/6.2021-1180.

[42] P. Fleming et al. "Simulation comparison of wake mitigation control strategies for a two-turbine case". In: Wind Energy 18.12 (2015), pp. 2135–2143. DOI: https://doi.org/10.1002/we.1810. URL: https://onlinelibrary.wiley.com/doi/abs/10.1002/we.1810.

[43] T.J. Broertjes et al. "Lift-Induced Wake Re-Energization for a VAWT-Based Multi-Rotor System". In: 2767.7 (2024), p. 072012. DOI: 10.1088/1742-6596/2767/7/072012. URL: https://dx.doi.org/10.1088/1742-6596/2767/7/072012.

[44] S. Aubrun et al. "Wind turbine wake properties: Comparison between a non-rotating simplified wind turbine model and a rotating model". In: Journal of Wind Engineering and Industrial Aerodynamics 120 (2013), pp. 1–8. ISSN: 0167-6105. DOI: https://doi.org/10.1016/j.jweia.2013.06.007. URL: https://www.sciencedirect.com/science/article/pii/S0167610513001220.

[45] L.E.M. Lignarolo et al. "Experimental comparison of a wind-turbine and of an actuator-disc near wake". In: Journal of Renewable and Sustainable Energy 8.2 (Mar. 2016). ISSN: 1941-7012. DOI: 10.1063/1.4941926. URL: https://doi.org/10.1063/1.4941926.

[46] J. Bossuyt, C. Meneveau, and Johan Meyers. "Wind farm power fluctuations and spatial sampling of turbulent boundary layers". In: Journal of Fluid Mechanics 823 (2017), pp. 329–344. DOI: 10.1017/jfm.2017.328.

[47] K. Steiros and M. Hultmark. "Drag on flat plates of arbitrary porosity". In: Journal of Fluid Mechanics 853 (2018), R3. DOI: 10.1017/jfm.2018.621.

[48] M. Huang. "Wake and wind farm aerodynamics of vertical axis wind turbines". PhD thesis. TU Delft, 2023. DOI: https://doi.org/10.4233/uuid:14619578-e44f-45bb-a213-a9d179a54264. URL: https://resolver.tudelft.nl/uuid:14619578-e44f-45bb-a213-a9d179a54264.

[49] A.M.O. Smith. "High-Lift Aerodynamics". In: Journal of Aircraft 12.6 (1975), pp. 501–530. DOI: 10.2514/3.59830. URL: https://doi.org/10.2514/3.59830.

[50] S. Scharnowski and C.J. Kähler. "Particle image velocimetry - Classical operating rules from today's perspective". In: Optics and Lasers in Engineering 135 (2020). ISSN: 0143-8166. DOI: https://doi.org/10.1016/j.optlaseng.2020.106185. URL: https://www.sciencedirect.com/science/article/pii/S0143816619318287.

[51] G. Tescione et al. "Near wake flow analysis of a vertical axis wind turbine by stereoscopic particle image velocimetry". In: Renewable Energy 70 (2014). Special issue on aerodynamics of offshore wind energy systems and wakes. ISSN: 0960-1481. DOI: https://doi.org/10.1016/j.renene.2014.02.042. URL: https://www.sciencedirect.com/science/article/pii/S0960148114001335.

[52] G. Elsinga, B. Scarano F.and Wieneke, and Bas van Oudheusden. "Tomographic Particle Image Velocimetry". In: Experiments in Fluids 41 (Dec. 2006), pp. 933–947. DOI: 10.1007/s00348-006-0212-z.

[53] F. Scarano. "Tomographic PIV: principles and practice". In: Measurement Science and Technology 24.1 (Oct. 2012). DOI: 10.1088/0957-0233/24/1/012001. URL: https://dx.doi.org/10.1088/0957-0233/24/1/012001.

[54] D. Schanz, S. Gesemann, and A. Schröder. "Shake-The-Box: Lagrangian particle tracking at high particle image densities". In: Exp Fluids 57.70 (2016). DOI: https://doi.org/10.1007/s00348-016-2157-1.

[55] A.M.O. Smith. "High-lift aerodynamics". In: Journal of Aircraft 12.6 (1975), pp. 501–530.

[56] M.S. Selig et al. Summary of Low-Speed Airfoil Data: Volume 2. SoarTech publications, 1997.

[57] M. Drela. MSES. https://web.mit.edu/drela/Public/web/mses/. Accessed on 2024-11-20. 2015.

[58] M.S. Selig et al. Summary of Low-Speed Airfoil Data: Volume 1. SoarTech publications, 1995.

[59] C.A. Schneider, W.S. Rasband, and K.W. Eliceiri. "NIH Image to ImageJ: 25 years of image analysis". In: Nature methods 9.7 (2012), pp. 671–675.

[60] Y. Li et al. "Numerical Investigation of Regenerative Wind Farms Featuring Enhanced Vertical Energy Entrainment". In: Wind Energy Science Discussions 2024 (2024), pp. 1–38.

[61] W. Yu. "The wake of an unsteady actuator disc". PhD thesis. Delft University of Technology, 2018. DOI: 10.4233/uuid:0e3a2402-585c-41b1-81cf-a35753076dfc.

[62] R.E. Hanson, H.P. Buckley, and P. Lavoie. "Aerodynamic optimization of the flat-plate leading edge for experimental studies of laminar and transitional boundary layers". In: Experiments in fluids 53 (2012), pp. 863–871.

[63] F. Scarano et al. "On the use of helium-filled soap bubbles for large-scale tomographic PIV in wind tunnel experiments". In: Experiments in Fluids 56 (2015), pp. 1–12.

[64] D.E. Faleiros et al. "Generation and control of helium-filled soap bubbles for PIV". In: Experiments in Fluids 60 (2019), pp. 1–17.

[65] D. Giaquinta. "The Flow Topology of the Ahmed Body in Cross-Wind". MA thesis. Delft University of Technology, 2018.

[66] W. Terra et al. "A Generic Cyclist Model for aerodynamic investigation: Design, geometry & first aerodynamic analysis of a male time-trial and sprint model". In: Journal of Wind Engineering and Industrial Aerodynamics 252 (2024), p. 105829.

[67] D. Bensason et al. "Experimental demonstration of regenerative wind farming using a high-density layout of VAWTs". In: prePrint 1111 (2024), p. 1111.

[68] B. Wieneke. "Volume self-calibration for 3D particle image velocimetry". In: Experiments in Fluids (2008). DOI: https://doi.org/10.1007/s00348-008-0521-5.

[69] A. Sciacchitano and B. Wieneke. “PIV uncertainty propagation”. In: Measurement Science and Technology 27.8 (2016), p. 084006.

[70] J.F. Manwell, J.G. McGowan, and A.L. Rogers. Wind energy explained: theory, design and application. John Wiley & Sons, 2010.

[71] T. Burton et al. “Aerodynamics of Horizontal Axis Wind Turbines”. In: Wind Energy Handbook. John Wiley & Sons, Ltd, 2011. Chap. 3, pp. 39–136. ISBN: 9781119992714. DOI: https://doi.org/10.1002/9781119992714.ch3. URL: https://onlinelibrary.wiley.com/doi/abs/10.1002/9781119992714.ch3.

A

Photos of the Regenerative Wind Farm Experiment

This appendix highlights the Regenerative Wind Farm experiment using four photos. The purpose of this is to give the reader a more complete understanding of the conducted experiment. This is done by showing different shots of the setup, the MRSL in different configurations, and a live measurement.

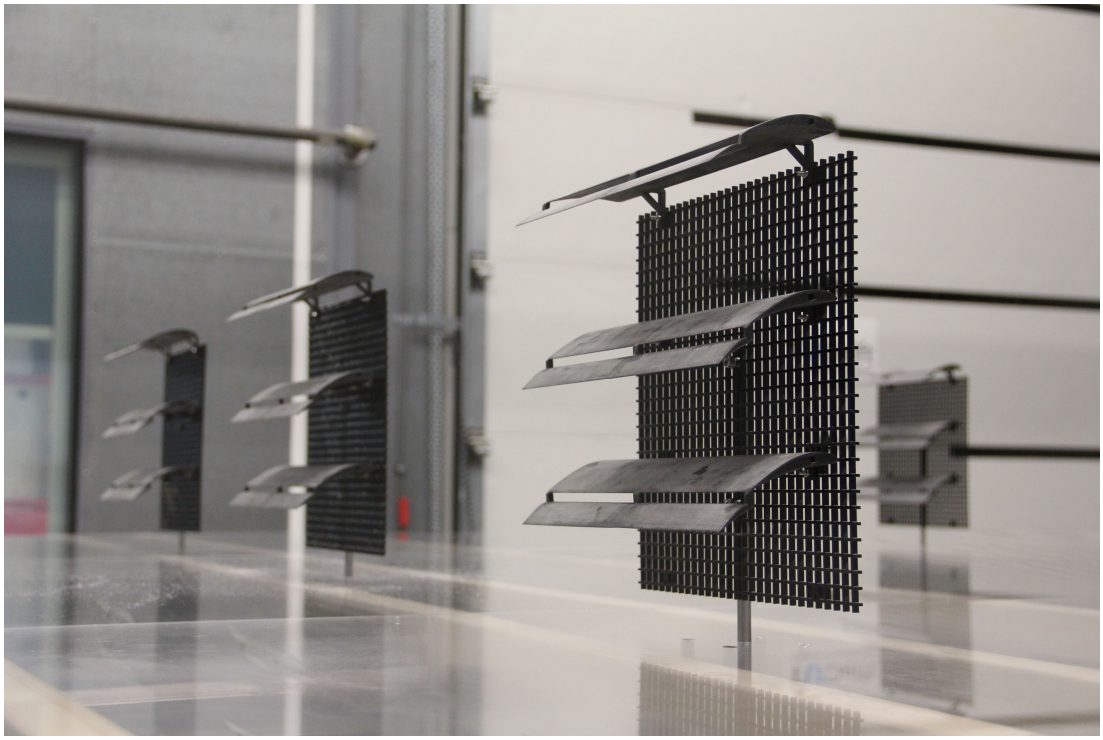

Figure A.1: Close-up of the third row of the Regenerative Wind Farm. The MRSLs are currently set to the Down-Washing configuration.

Figure A.1 shows the third row of the Regenerative Wind Farm. The MRSLs are configured for the Down-Washing case. The sunken bolts ensure no obstruction other than the support rod is experienced by the flow.

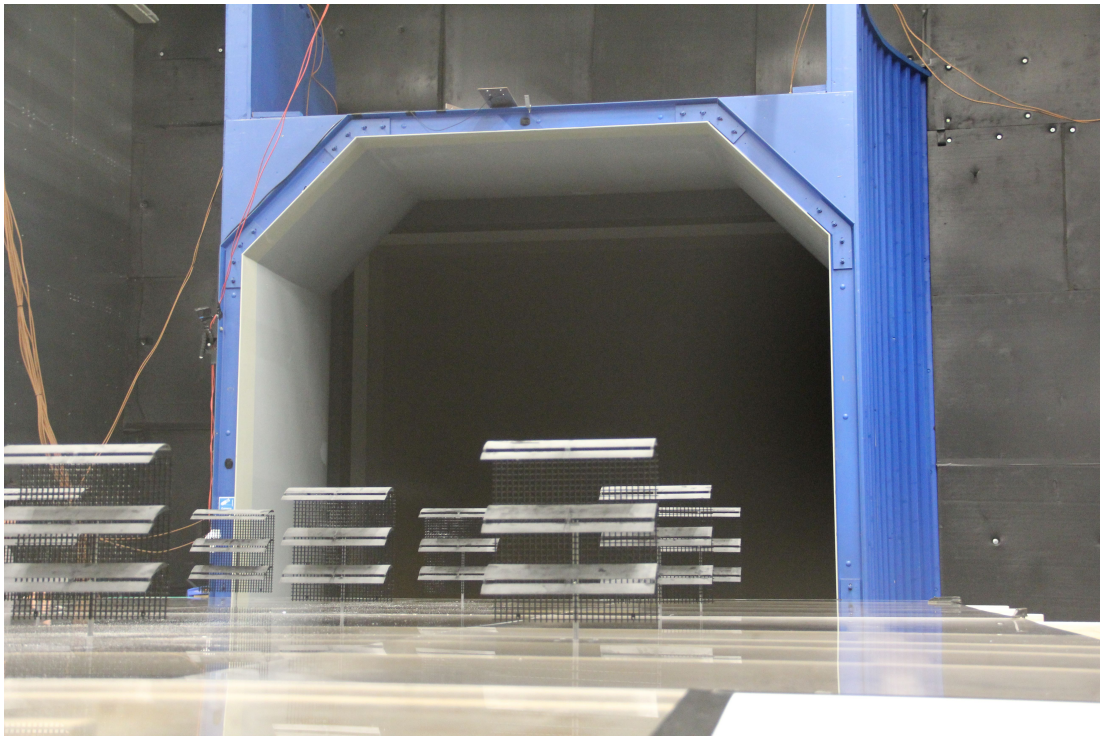

Figure A.2: The Regenerative Wind Farm shot from behind. The MRSLs are currently set to the Down-Washing configuration and nine MRSLs are installed. The tunnel exit, in blue, is visible.

Figure A.2 shows the Regenerative Wind Farm in the Down-Washing configuration once again. From this angle, the tunnel exit, highlighted in blue, is clearly visible. The floor is raised to align with the widest part of the tunnel exit, and it is significantly wider than the tunnel exit itself. The absence of supporting structures above the floor ensures that the flow remains unobstructed.

In Figure A.3, the MRSLs are arranged for the Up-Washing case. This photo captures the 10D row spacing configuration, as the second row has been removed. The tunnel exit is visible again, along with the three cameras positioned for data collection. This setup corresponds to traverse position 1.

The final photo in this appendix, shown in Figure A.4, captures a live measurement. During the measurement process, all lights in the test section are turned off, with only the LED active to illuminate the helium-filled tracer particles. This specific measurement focuses on the wake of the third row.

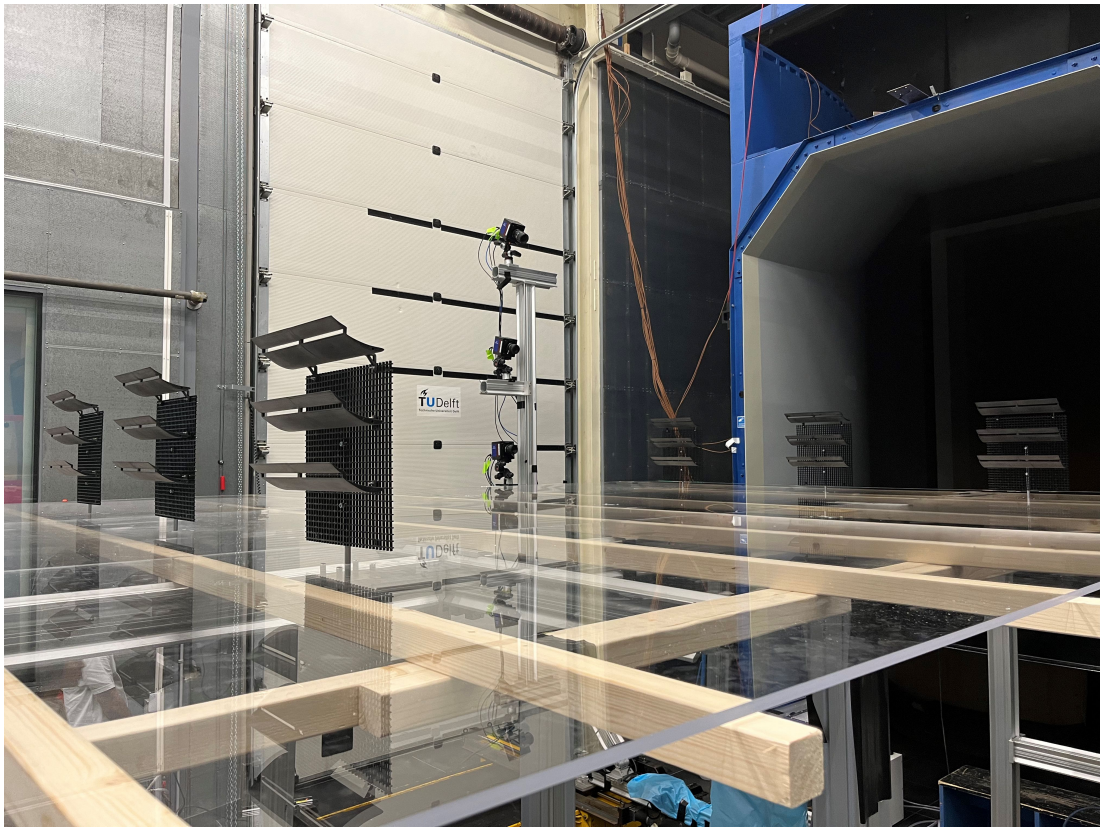

Figure A.3: Photo of the 10D Up-Washing case of the Regenerative Wind Farm. The tunnel exit and the PTV cameras are visible.

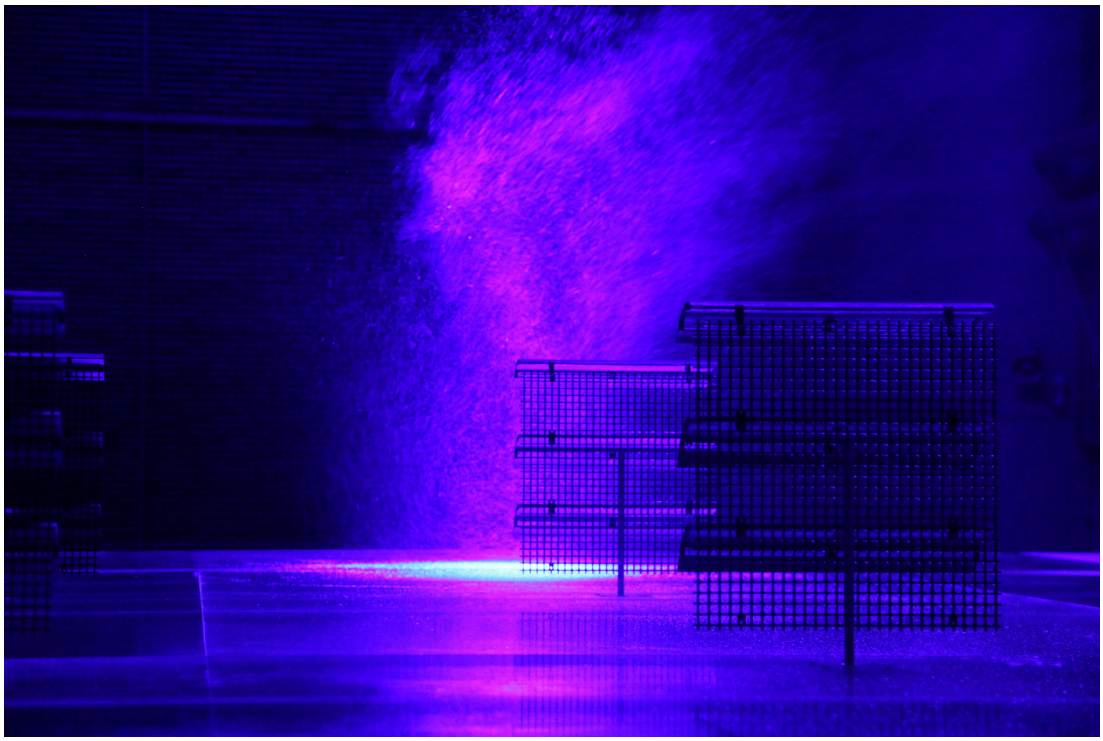

Figure A.4: Live measurement for the 5D Down-Washing case. The LED is illuminating the tracer particles from below the transparent floor. In this photo, traverse position 3 is active.

B

Reynolds Number Dependency

To ensure that the experimental results are not significantly affected by variations in Reynolds number, the loads of RGWFs with different configurations (the first six listed in Table 4.1) under several inflow wind speeds (u_∞) were measured. The results, presented in Figures B.1 and B.2, show that the normalized forces exerted by MRSLs across all considered configurations are insensitive to variations in u_∞ within the range of 6.2 to 7.3 m/s. Therefore, it is concluded that the results obtained in this study are independent of changes in Reynolds number.

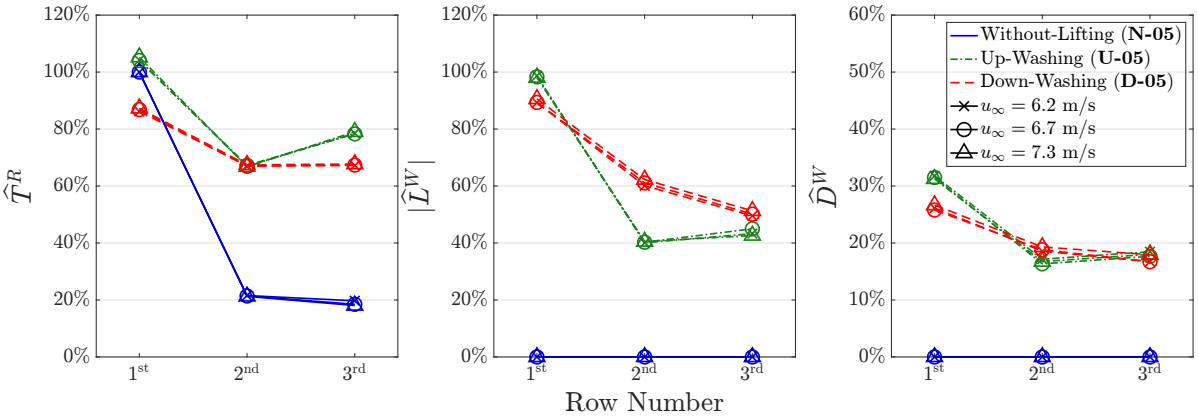

Figure B.1: Normalized (time-averaged) rotor's thrust ($\widehat{T}^R$), wings' lift ($\widehat{L}^W$), and wings' drag ($\widehat{D}^W$) for cases with $\Delta_R = 5D$ measured under different inflow wind speeds u_∞. Note that the normalization factor $T^R\big|_{1^{\text{st}}}^{\text{WL-05}}$ varies based on $u\infty$. Results of different u_∞ are represented by different markers, while line colors (and line styles) indicate different RGWF configurations.

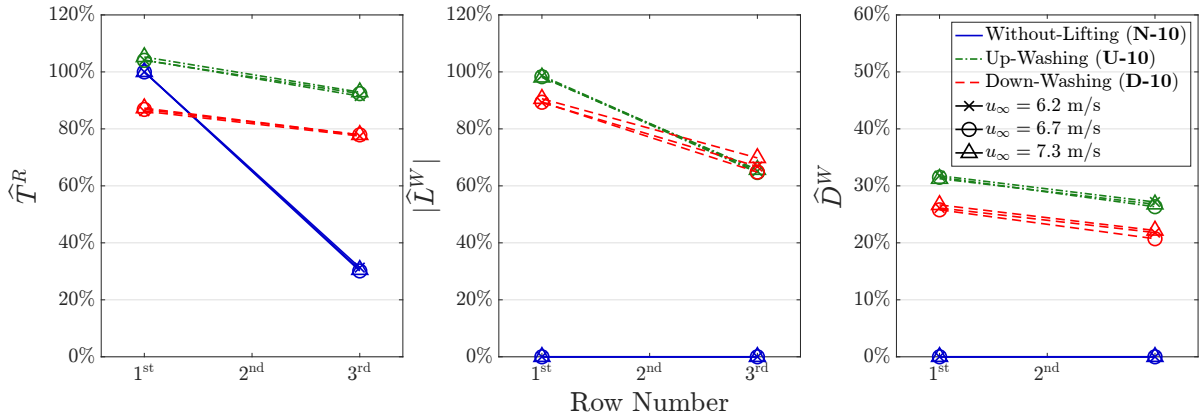

Figure B.2: Normalized (time-averaged) rotor's thrust ($\widehat{T}^R$), wings' lift ($\widehat{L}^W$), and wings' drag ($\widehat{D}^W$) for cases with $\Delta_R = 10D$ measured under different inflow wind speeds u_∞. Note that the normalization factor $T^R\Big|_{1^{\text{st}}}^{\text{WL-10}}$ varies based on $u\infty$. Results of different u_∞ are represented by different markers, while line colors (and line styles) indicate different RGWF configurations.